HITTITE JOURNAL OF SCIENCE AND ENGINEERING

HITTITE JOURNAL OF SCIENCE AND ENGINEERING

Dear Readers,

I start the preface of this issue with good news. After working very hard for years and completing all of the necessary tasks and procedures, as a team of Hittite journal of Science and Engineering (HJSE), we have just applied for the databases of Web of Science, Engineering Village (Scopus) and ProQuest Engineering. As the Editor-in-Chief, I hope that our applications will be accepted. During the publication period of this new issue of Hittite journal of Science and Engineering (2024 – Volume: 11 issue:4), I would like to express my gratitude to the president of Hitit University for his support, the associate editors, section editors, reviewers, Hitit University Publishing Office and Production Team of HJSE for their devoted efforts and sacrifices.

As Editor in Chief, I would like to thank to the authors submitting their scientific work to HJSE. In this issue, the articles from the five branches of engineering including Chemical, Food, Geomatics, Electronics and Mechanical engineering were published. The article related to the chemical engineering focuses polyvinylalcohol/polyethyleneimine (PVA/PEI) hydrogels that were fabricated using Glutaraldehyde as crosslinker via solvent casting method and it was found that all of the hydrogels showed great swelling degree at pH 7.4 simulating human biological fluids and 370 C. The article from food engineering is mainly based on the derivation of the aggregation of the lactase enzyme from *Kluyveromyces lactis* using polyethyleneimine without involving any support or solvent for precipitation. In the article from geomatics engineering, the unmanned aerial vehicles (UAVs) flights over a selected test area at various altitudes (30m, 45m, 60m) were operated to evaluate the 3D positioning accuracy of photogrammetric models generated without using any Ground Control Points (GCPs), and their locations were compared against the precise the Global Navigation Satellite System (GNSS) observations for twenty-two control points. As for the article in electronics engineering, two different capacitance multiplier structures were presented for comprehensive noise analyses and optimization and it was found that the initial input referenced noise was 10.13 mV, reduced to 6.19 mV (40% reduction) by optimization, although this resulted in a 20% change in cut-off frequency. In the final article from the area of mechanical engineering, the in-depth investigations of the Novel Inclined Delta Winglet (NIDW) in terms of heat transfer performance and flow characteristics are carried out at Re=5000-17500, using the (SST) k-ω turbulence model. I hope that these papers will be of benefit to researchers in the disciplines mentioned above.

I am pleased to invite researchers and scientists from all engineering disciplines to submit their best articles to be published in the Hittite Journal of Science and Engineering.

Dr. Ali Kılıçarslan

Editor-in-Chief

CONTENTS

High-Precision UAV Photogrammetry with RTK GNSS: Eliminating Ground Control Points

Mehmet Nurullah Alkan ⓘ

Hitit University, Osmancık Ömer Derindere Vocational High School, 19500, Çorum, Türkiye.

Corresponding Author

Mehmet Nurullah Alkan
E-mail: nurullahalkan@hitit.edu.tr Phone: +90 530 511 56 69 Fax: +90 364 611 50 30
RORID: https://ror.org/01x8m3269

Cite As

High-Precision UAV Photogrammetry with RTK GNSS: Eliminating Ground Control Points

Mehmet Nurullah Alkan

Hitit University, Osmancık Ömer Derindere Vocational High School, 19500, Çorum, Türkiye.

Abstract

The advancements in Unmanned Aerial Vehicles (UAVs) have significantly enhanced the capability of the photogrammetric approaches, particularly with the integration of Real-Time Kinematic (RTK) sensors. That approach enables the operators to use the Global Navigation Satellite System (GNSS) more efficiently with the production of high-precision 3D Digital Terrain Models (DTMs). Traditionally, Ground Control Points (GCPs) are used to link those models to a ground coordinate system, but their establishment is time-consuming and labor-intensive, requiring static or rapid-static GNSS observations over two hours for each point. However, RTK-embedded UAVs offer a significant improvement by facilitating direct geo-referencing of DTMs, which includes the estimation of internal and external orientation parameters more efficiently and potentially eliminating the need for GCPs.

In this study, UAV flights over a test area at various altitudes (30m, 45m, 60m) were conducted to evaluate the 3D positioning accuracy of photogrammetric models generated without using any GCP, and their locations were compared against the precise GNSS observations for 22 control points. Results indicated that UAVs with RTK ability could achieve centimeter-level accuracy in positioning, making this kind of evaluation a viable alternative to traditional methods. This study also discusses the implications of those results within the context of large-scale map production and their regulations in Türkiye. The elimination of GCPs should significantly reduce the time and effort associated with map production, suggesting a potential alternative in regulatory standards to incorporate these technological approaches.

Keywords: UAV, RTK GNSS, photogrammetry, direct geo-referencing, 3D modeling, GCP, Türkiye mapping regulations.

INTRODUCTION

In order to implement field observations, there are several methods using different technologies or approaches. The main issue for those positional evaluations arises from the required precision of the subject, the offered accuracy of the method and the accomplished detail level of the scene (building, field, etc.), whether it is a direct technique or an indirect method. In this context, total station, Global Navigation Satellite System (GNSS), laser-scanning and terrestrial/aerial photogrammetry are the most common procedures today. However, the final solution for all those methods includes the representation of the field, whether by a 2D/3D point cloud (laser scanning and photogrammetry) or the characteristic edges of the scene material (total station and GNSS) (1-4).

Unmanned Aerial Vehicles, known as UAVs or drones, are commonly used in many applications to acquire point clouds, which include high-precision observations of an area. With the possibility of collecting digital images and technological advancements within UAVs, it is possible to create a 3D model of a ground surface in a short time period economically using an aerial photogrammetric approach (5-7). This technique requires less expensive equipment and minimal time-consuming process in the field compared to the other mentioned methods above with several advantages, which include:

- High-precision and dense point cloud data,
- Economic evaluation of metric information from the 3D model (volume, area, etc.),
- Repeated measurements on the model at any time without new flights or processes (6-9).

During the process, acquired data including overlapped images from the field lead to the creation of point clouds, orthophoto maps and DTMs which can be used in mapping, inspection of constructions, emergency applications, archaeology, architecture, monitoring topographic alterations, preservation of cultural heritage, etc. (4, 10-15). The main output of those photogrammetric procedures includes the processing of multi-spectral, thermal, or visible-light images taken at regular intervals from the scene and linking them to the ground coordinate system. That process is defined as "georeferencing" and has two different approaches: (i) direct and (ii) indirect georeferencing. The direct method is implemented by using the camera's position information collected by an onboard GNSS receiver. The other method can be performed by using the coordinates of specific points (GCPs) on the ground but requires additional observations on the field. The accuracy of those methods generally depends on the flight route and height, image resolution, and especially preferred georeferencing solution. Either way, those approaches enable operators to link their 3D model to the ground truth, which is produced by Structure from Motion (SfM), a multi-image photogrammetry technique, and have an arbitrary reference coordinate system for the final outputs (6-7, 9, 14, 16-18).

The 3D positioning accuracy of a UAV model strongly depends on the GNSS type used on the board. If the GNSS sensor has the ability to process code-based signals, the accuracy is about ±5-10 m in both horizontal and vertical directions, but the capability to use dual-frequency satellite signals enables the procurement of cm-level 3D positioning (7, 18-20). The first case requires additional fieldwork. Here, GCPs are essential to convert the photogrammetric model into a ground coordinate system by scaling the whole cloud of points, and according to the current regulations in Türkiye, one should conduct at least 2 hours of GNSS observations (rapid-static surveys) on all of the GCPs in the scene (6, 21). There is no consensus on the number and distribution of the GCPs in a scene, but some theoretical studies indicate that a well-distributed 5-10 GCPs are sufficient to create a 3D model independent from the area of the process. If the number of GCPs increases, operating costs will also rise accordingly (4, 7, 22). The other case can be achieved by using UAVs with Real-Time Kinematic (RTK) capabilities which allow the collection

of field data with direct georeferencing. That situation eliminates the need for GCPs (4, 23-25).

Photogrammetric solutions based on either of those approaches have specific drawbacks inherent to the techniques themselves. They include gathering permissions for each flight, weather conditions, flight duration, time window during the daylight, GCP establishment and observation via GNSS, etc., and the after-flight process of constructing a DTM. Nevertheless, a general evaluation of those methods indicates that GCP establishment in the field is the most prominent obstacle to 3D model creation (18, 26-29).

In this study, the positional accuracy of three different models generated from UAV flights at altitudes of 30, 45, and 60 meters over a test field were tested against GNSS observations on the same object points. The position data of those points were generated using the photogrammetric point clouds, and the correlation with the reference coordinates was examined. That situation enables the test for whether the photogrammetric models could achieve the theoretical accuracy of GNSS observations based on the Continuously Operating Reference Stations (CORS (TUSAGA-AKTİFTR)) system (23). Additionally, the necessity of GCPs, which are considered C3-level reference points according to regulations in Türkiye and used for georeferencing, was comparatively analyzed. UAV-based photogrammetry in large-scale mapping and terrestrial positioning projects was also evaluated, while the effects of UAV flight altitudes on the current map production accuracy were examined in detail. This study also aims to evaluate the accuracy and reliability of UAV-based photogrammetric methods and to reveal their compatibility with terrestrial GNSS measurements. Additionally, by discussing the role and necessity of GCPs in photogrammetric processes, important insights into how those technologies can be used more effectively within the framework of existing regulations in Türkiye were presented.

METHODOLOGY

Test field assessment and CP selection

To compare GNSS observations with the UAV photogrammetric model in terms of precision, an area with prominent markers was selected (Figure 1). This test field is the parking lot of the Faculty of Science and Literature at Hitit University in Çorum Province, Türkiye, and was chosen due to the presence of distinctive and well-distributed markers.

The absence of obstacles at the specified flight altitudes is another reason for selecting this site. Also, the calculated ground height of selected Control Points (CP) were used with their original computed elevation, because no embossed paint was applied. One can assume that this situation in the field simulates real-world conditions often encountered in practice for distinctive objects, such as road edges, field boundaries, and building corners. Therefore, CPs are selected as features like road edge lines and arrows (Figure 2).
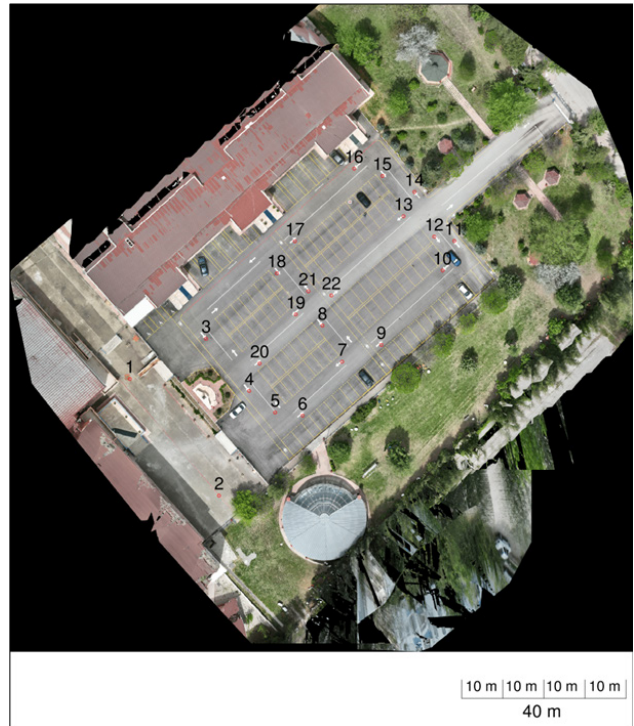
Figure 1 Test field used in this study. A well-distributed set of 22 points was chosen from the parking lot (mostly covered with straight lines and arrows).

Figure 2 West side of the parking lot from 30 m flight altitude. CPs on this part of the field were marked with red circles (CPs 3-6 and 20).

GNSS observations

A total of 22 distinctive objects in the field were selected as CPs, and their coordinates were calculated as the average of two different GNSS sessions with one-hour intervals. During the process, a GNSS receiver compatible with the CORS-TR network was used, and calculated positions of the CPs were considered as reference coordinates for further evaluation. Such observations are considered as RTK or Network-RTK, according to the used base stations. This is accomplished by using a base station (via RTK) or a whole network (Network-RTK) that sends correction vectors to the rover (in this case GNSS receiver and UAV) and applying those values to precisely generate the 3D position. Network-RTK observations, preferred to collect the reference coordinates in this study, offer real-time corrections for centimeter-level accuracy theoretically. Although current regulations in Türkiye suggest a minimum of 3 epochs for detail points, 10 epochs of

observations were executed for each session, adhering to the primary criterion for polygon coordinate calculations (21, 31).

UAV flights

Autonomous flights over the field were performed with a UAV with RTK capability at altitudes of 30, 45, and 60 meters. The UAV used in this study was the DJI Mavic 3 Enterprise, which offers robust performance with a weight of 915 grams and a maximum flight speed of 15 m/s. It is equipped with a GNSS system which can operate with multiple satellite constellations, and a wide camera sensor with a resolution of 20 megapixels, producing images up to 5280 x 3956 pixels. The UAV's gimbal stabilization is three-axis, ensuring stable and clear images and the RTK module positioning accuracy is within 1 cm + 1 ppm horizontally and 1.5 cm + 1 ppm vertically (Table 1).

Table 1 Key specifications of the UAV used in this study (URL-5).

Brand/Model	DJI/Mavic 3 Enterprise
Weight	915 g
Max flight speed	15 m/s
Used GNSS	GPS+Galileo+BeiDou+GLONASS
Wide camera sensor	4/3 CMOS, 20 MP
Max image size	5280x3956
Gimbal stabilization	3-axis
RTK module positioning accuracy (RTK Fix)	Horizontal: 1 cm + 1 ppm Vertical: 1.5 cm + 1 ppm

During the UAV flights, a GNSS receiver inside the parking lot is used as a reference station. In this step, a random location for the point was selected, and 3D coordinates were computed with a 60-epoch observation. The coordinates were then used as reference coordinates for all the photogrammetric models. Then, the GNSS receiver was linked to the UAV control unit and started to send correction values via Bluetooth during the flights.
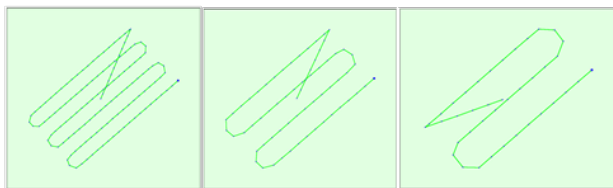
Figure 3 Top view of the flight routes and initial image positions for 30-45-60m flights, respectively. The green line represents the flight route of the UAV, with a big blue dot (starting point) and black dots (camera positions). Direct lines from the last points of the routes to the center of the models represent the UAV height correction route. That feature enables the collection of images with a 45-degree camera angle and develops the estimation of the whole model's elevation data (URL-5).

A total of 138, 65, and 39 digital images were collected during the autonomous flights at 30 m, 45 m, and 60 m altitudes, respectively. Forward and side image overlap ratios were selected as 80% and 70% respectively, to ensure an accurate 3D photogrammetric model of the field with a 90-degree camera angle. The camera, which is embedded in the UAV (M3E_12.3 RGB), provides sufficient resolution for all flights in the study; and the ground sampling distance (GSD), area covered, and the number of images for each flight altitude detailed in Table 2. This setup ensured comprehensive coverage and high-resolution data collection for subsequent photogrammetric processing (Figure 3, 4, 5).

Table 2 Specifications of flight altitudes. Processed areas differ from each other; thus, the flight altitudes enable to collect images with a larger perspective as the height increases. This situation has a drawback on the Ground Sampling Distance.

Flight Altitude	Ground Sampling Distance (GSD)	Area Covered	Number of Images
30 m	0.85 cm	1.6673 ha.	138
45 m	1.27 cm	2.3190 ha.	65
60 m	1.68 cm	3.2324 ha.	39

Photogrammetric model generation

To generate a 3D DTM of a field, third-party applications such as Agisoft Photoscan, Pix4D, and Terra can be used. Those software programs can process all the aerial digital images with aerial triangulation and bundle block adjustment procedures to generate ortho-mosaic maps and point clouds. In this study, Pix4D was selected for all the digital processing steps. That software enables users to create point clouds, orthophotos, and accurate DTMs from aerial images (7, 9, 22, 33). The generated point clouds then were used to derive the 3D coordinates of the CPs.

The processed data enables high-resolution ortho-mosaic images and detailed DTMs for each flight altitude, and those are critical for assessing the accuracy and reliability of the photogrammetric models. The ortho-mosaic images provide a precise and geometrically corrected view of the field, ensuring that spatial relationships are accurately represented. The DTMs, on the other hand, represent the elevation data of the field's surface, capturing the subtle variations in height that are crucial for various analytical purposes (Figure 4).

In Figure 4, details and covered area have an inverse proportion; as the altitude increases, the area increases, but resolution decreases as expected. That can be observed clearly on the roof of the building in the north-west.

In order to assess the reliability of the models, geolocation variance for all flights has significant importance (Table 3). Those values indicate the difference between the
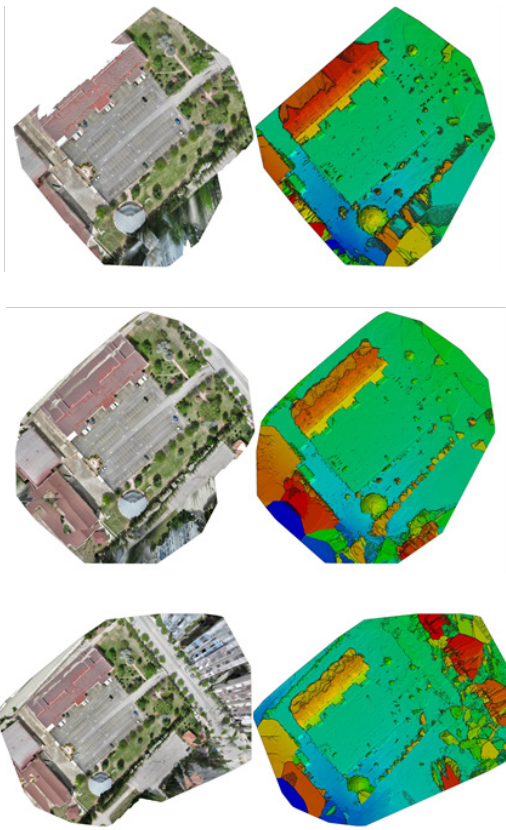
Figure 4 Ortho-mosaic and DTM were generated for 30-45-60m UAV flights, respectively.

According to Table 3, even with the higher altitudes up to 60 m, the 3D positional accuracy of the models is adequate for further evaluation. Also, all the geolocation errors are below 1 cm, but vertical accuracy might need careful consideration. Overall, the 45m flight offers the best correlation between horizontal and vertical precision.

Table 3 Geolocation errors for all photogrammetric models.

	Geolocation Error X	Geolocation Error Y	Geolocation Error H
RMS Error (m) [30 m]	0.005488	0.006392	0.006464
RMS Error (m) [45 m]	0.004127	0.004216	0.005418
RMS Error (m) [60 m]	0.003225	0.003213	0.007683

Data comparison and discussion

To analyze the differences between the ground truth at the 22 CPs and the photogrammetric models, all data was evaluated to determine if they have a normal distribution or not. For this purpose, the Shapiro-Wilk test was executed to assess the normality of the differences in all 3 axes, and the Paired t-test and Wilcoxon tests were applied, when necessary, to figure out if there was a systematic diversity (34-36). In addition, the mean error, root mean square error (RMSE), and standard deviations (σ) were calculated for each coordinate diversity pair to verify the variability and reliability of the photogrammetric models. Those analyses are crucial for evaluating the accuracy and reliability. Specifically, the mean error indicates the degree of deviation in the models, while the RMSE and σ values are important metrics for assessing the overall accuracy and data dispersion.

RESULTS

The average coordinates of two different GNSS sessions for 22 different CPs in the field were accepted as the reference coordinates. Subsequently, the coordinates of those points were calculated from each point cloud generated using Pix4D software for the 30, 45 and 60 m flights (22). As expected, there are distinctive differences in the Y, X, and H coordinates between the data sets (Table 4, Figure 5).

According to Table 4, the differences are below the specified values required by regulations in Türkiye (21). Maximum deviation and mean error for all axes promote the situation. Specifically, elevations for all altitudes indicate a careful approach for this axis.

Figure 5. Coordinate differences for all axes. Average and maximum deviations (as absolute value) are given under the graphs.

Table 4. CP Coordinate differences between GNSS observations and photogrammetric models.

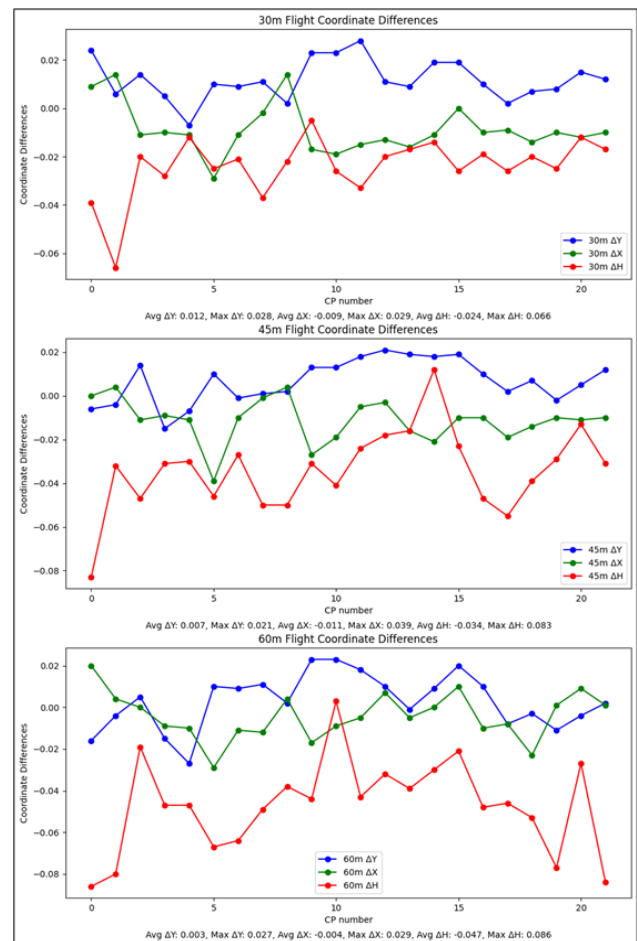|	30m flight			45m flight			60m flight		
#	ΔY(m)	ΔX(m)	ΔH(m)	ΔY(m)	ΔX(m)	ΔH(m)	ΔY(m)	ΔX(m)	ΔH(m)
1	0.024	0.009	-0.039	-0.006	0.000	-0.083	-0.016	0.020	-0.086
2	0.006	0.014	-0.066	-0.004	0.004	-0.032	-0.004	0.004	-0.080
3	0.014	-0.011	-0.020	0.014	-0.011	-0.047	0.005	0.000	-0.019
4	0.005	-0.010	-0.028	-0.015	-0.009	-0.031	-0.015	-0.009	-0.047
5	-0.007	-0.011	-0.012	-0.007	-0.011	-0.030	-0.027	-0.010	-0.047
6	0.010	-0.029	-0.025	0.010	-0.039	-0.046	0.010	-0.029	-0.067
7	0.009	-0.011	-0.021	-0.001	-0.010	-0.027	0.009	-0.011	-0.064
8	0.011	-0.002	-0.037	0.001	-0.001	-0.050	0.011	-0.012	-0.049
9	0.002	0.014	-0.022	0.002	0.004	-0.050	0.002	0.004	-0.038
10	0.023	-0.017	-0.005	0.013	-0.027	-0.031	0.023	-0.017	-0.044
11	0.023	-0.019	-0.026	0.013	-0.019	-0.041	0.023	-0.009	0.003
12	0.028	-0.015	-0.033	0.018	-0.005	-0.024	0.018	-0.005	-0.043
13	0.011	-0.013	-0.020	0.021	-0.003	-0.018	0.01-2	0.007	-0.032
14	0.009	-0.016	-0.017	0.019	-0.016	-0.016	-0.001	-0.005	-0.039
15	0.019	-0.011	-0.014	0.018	-0.021	0.012	0.009	0.000	-0.030
16	0.019	0.000	-0.026	0.019	-0.010	-0.023	0.020	0.010	-0.021
17	0.010	-0.010	-0.019	0.010	-0.010	-0.047	0.010	-0.010	-0.048
18	0.002	-0.009	-0.026	0.002	-0.019	-0.055	-0.008	-0.008	-0.046
19	0.007	-0.014	-0.020	0.007	-0.014	-0.039	-0.003	-0.023	-0.053
20	0.008	-0.010	-0.025	-0.002	-0.010	-0.029	-0.011	0.001	-0.077
21	0.015	-0.012	-0.012	0.005	-0.011	-0.013	-0.004	0.009	-0.027
22	0.012	-0.010	-0.017	0.012	-0.010	-0.031	0.002	0.001	-0.084

Table 5. Tests for coordinate differences. According to Shapiro-Wilk test results, Paired t-test was applied to 30 m (Y) and 45 m (Y, X, H) flights. Values without normal distribution are evaluated through Wilcoxon test.

Metric	30m	45m	60m
Shapiro-Wilk Test (Y)	W=0.9707, p=0.7282	W=0.9543, p=0.3826	W=0.9693, p=0.6955
Shapiro-Wilk Test (X)	W=0.8644, p=0.0062	W=0.9283, p=0.1129	W=0.9825, p=0.9507
Shapiro-Wilk Test (H)	W=0.8475, p=0.0031	W=0.9510, p=0.3303	W=0.9643, p=0.5808
Paired t-test (Y)	t=6.632, p=1.449e-06	t=3.1813, p=0.0045	-
Paired t-test (X)	-	t=-5.3123, p=0.0000	-
Paired t-test (H)	-	t=-8.5361, p=0.0000	-
Wilcoxon Test (Y)	-	-	W=92.5, p=0.2902
Wilcoxon Test (X)	W=33.0, p=0.0041	-	W=59.5, p=0.0893
Wilcoxon Test (H)	W=0.0, p=4.768e-07	-	W=1.0, p=9.536e-07

At this step, it is necessary to statistically evaluate whether those differences are significant or systematic. For this purpose, the Shapiro-Wilk test was initially used to determine whether the coordinate differences for all three axes have a normal distribution or not (35). The components with a normal distribution (p>0.05) were assessed using the Paired t-test, while those without a normal distribution (p≤0.05) were evaluated by a non-parametric (Wilcoxon) test (34, 36). For this purpose, the test results for each flight at 30, 45, and 60 meters were examined (Table 5).

The results of the Shapiro-Wilk test indicated that only the Y coordinate differences at 30m and all axes for 45m have a normal distribution. The paired t-test results showed significant differences in the Y axis at 30m and in the Y, X, and H axes at 45m. Also, 60m altitude does not have a normal distribution; thus, the Wilcoxon test is applied for this flight route. The analysis of the differences in coordinates obtained from GNSS and photogrammetric methods for flights from 30 m and 45 m altitudes indicates varied statistical significance. That leads to systematic differences amongst them. Despite those differences, RMSE and σ values indicate that both the photogrammetric model and GNSS measurements are generally consistent and reliable, and systematic errors may arise from the uncertainty in the RTK technique (Figure 6). However, the photogrammetric model from the 60 m flight altitude exhibits different characteristics from the other models. In this case, coordinate differences along Y and X axes are not significant, indicating random errors around this

flight route and no systematic error. Also, height coordinate observations require careful examination due to their higher variability across all the photogrammetric models.
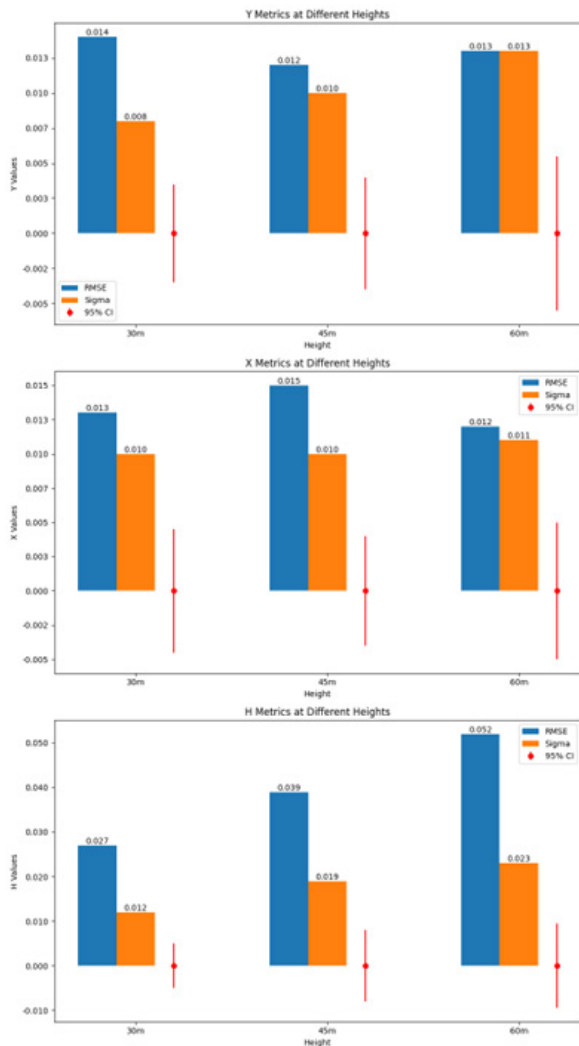

Figure 6. RMSE, σ and confidence intervals (95%) for all altitudes.

According to Figure 6, similar RMSE and σ values were calculated for the Y and X coordinate differences at 30 m and 45 m, an increase in RMSE and sigma values was observed for the H axis. This indicates that there is more deviation in the H coordinate measurements as the height increases, which is supported by the statistical test results (Table 5). Also, the 95% confidence intervals provide important information for assessing the reliability and accuracy of the measurements. Particularly at the 60 m height, the wide confidence interval and high RMSE value for the H coordinate suggest that measurements at this height require careful assessment.

DISCUSSION

In this study, the 3D coordinates of 22 CPs were calculated as the average of two different GNSS sessions and results were accepted as reference coordinates for further evaluations. Then, autonomous photogrammetric flights were conducted at 30, 45, and 60 meters in the same test field using a Mavic

3E UAV. The data obtained from those flights were processed using Pix4D software to create point clouds for each flight. The 3D coordinates of CPs were determined using the models. Those two data sets were analyzed for statistical significance. Photogrammetric models derived from different UAV altitudes enable comparison of the precision and accuracy of the data sets. Here, the RTK capabilities of the Mavic 3E UAV and the Pix4D software made it possible to create highly accurate 3D models. Calculating the differences between the GNSS data and photogrammetric models and statistically analyzing those differences provide ability to evaluate the reliability and accuracy of different methodologies.

This study aims to examine the coordinate differences between GNSS and photogrammetric data, demonstrating the accuracy and reliability of photogrammetric methods. Additionally, the results provide crucial information for evaluating UAV-based photogrammetry in large-scale mapping projects. In this context, the comparisons also contribute to identifying necessary improvements to enhance the accuracy of photogrammetric models.

Statistical Analysis

The Shapiro-Wilk test was applied to evaluate the normal distribution of all data sets. The results of this test led to the selection of appropriate statistical tests and enhanced the accuracy of the analytical process. Then, the paired t-test was used for differences with normal distribution, while the non-parametric Wilcoxon test was applied for the data outside of that kind. Those statistical tests are critical for assessing the accuracy and reliability of photogrammetric flights conducted at different altitudes. Additionally, the RMSE, confidence intervals, and σ values were used to determine the numerical variances of coordinate differences and the reliability of photogrammetric flights. RMSE values help to assess the magnitude of the errors in each axis, while confidence intervals indicate the statistical reliability and precision of the results. σ values measure the spread and degree of deviation in the data, playing a crucial role in comparing UAV flights.

Those comprehensive statistical analyses allowed for an in-depth examination of the reliability and accuracy of the data obtained from the flights. Understanding the numerical variances of coordinate differences is essential for evaluating the performance of the flights conducted at different altitudes. Also, RMSE, confidence intervals, and σ values facilitate a thorough interpretation of the results. Those analyses have established a significant basis for comparing the precision of photogrammetric methods and GNSS measurements.

Findings

The results indicate systematic and significant differences between the GNSS measurements, and the photogrammetric models conducted at 30 m and 45 m altitudes. For the 60 m flight, the errors in the Y and X axes were random, while the H differences remained significant and systematic, as observed in the other photogrammetric models. Those results are crucial in terms of the usability of photogrammetric models in projects requiring high accuracy. Regulatory standards, in particular, stipulate that differences between horizontal and

vertical coordinates should not exceed ±7 cm in large-scale map production, thus, almost all the differences are below these limits, especially for 30 m and 45 m UAV models. Those results indicate that GCP establishment in the field may not be essential while using RTK-UAVs. This step is significant to ensure both compliance with existing regulations and to obtain higher accuracy data.

Regulatory Implications

According to Türkiye's "Regulation on the Production of Large-Scale Maps and Map Information," the differences between reference and observed coordinates must not exceed ±7 cm in both horizontal and vertical values (22). The results demonstrate that photogrammetric models can achieve better accuracy than the specified limit. This suggests that UAV-based photogrammetry, using embedded RTK modules, can be utilized as an alternative to traditional GNSS-based methods for certain applications. The UAV data collection without the use of any GCPs in the field may eliminate the necessity for rapid/static GNSS observations at any ground point in the field. This may require updating the relevant articles of the regulation to reflect current conditions.

The accuracy of photogrammetric models satisfying the regulatory limits enhances the potential of UAV use in large-scale mapping projects. This can accelerate the data-gathering process and reduce costs in areas where field conditions are challenging or with limited access. For instance, UAVs can collect data more quickly and reliably than traditional methods in areas such as forests, mountainous regions, or urban areas.

Furthermore, the RTK-UAV approach can offer significant advantages in fields such as disaster management, agriculture, urban planning, and environmental monitoring. This technology's rapid data collection and analysis capabilities can provide assistance for quick responses in emergencies and expedite decision-making processes. Additionally, in agriculture, this technique may contribute to the development of precision farming applications such as plant health monitoring and yield prediction.

Updating current regulations and eliminating the GCP should cover not only the accuracy criteria for photogrammetric methods of this kind but also the standards for equipment and software used in data collection processes. That will enable more consistent and reliable data acquisition for all stakeholders.

CONCLUSION

This study highlights the potential of using RTK-embedded UAVs to achieve high-accuracy 3D positioning similar to traditional GNSS techniques without the need for any GCPs in the field. The results demonstrate that UAV-based photogrammetry can provide reliable and precise measurements, making it a viable alternative for various geospatial applications.

Furthermore, it is suggested that the current regulations in Türkiye should be updated to accommodate advancements in UAV technology. The existing regulations are primarily designed with traditional surveying methods in mind and may not fully reflect the capabilities and advantages of modern UAV systems. Updating the regulations could significantly reduce the time and effort required for large-scale map production, thereby enhancing efficiency and cost-effectiveness. This is particularly important in contexts where rapid data collection and processing are critical, such as disaster response, urban planning, and environmental monitoring.

Future research should focus on further enhancing the capabilities of UAV photogrammetry, specifically improving the accuracy of photogrammetric models in H axis. This may involve refining the algorithms used for data processing and exploring new methods for integrating UAV data with other geospatial data sets.

Additionally, optimizing UAV flight parameters and RTK capabilities is of critical importance. The impact of different flight altitudes, speeds, and patterns on data accuracy and reliability can help developing best practices for UAV operations in various environments under different conditions. In conclusion, this study reveals that RTK-based UAV photogrammetry is a reliable and effective tool for large-scale map production and other applications, meeting regulatory requirements and without GCP establishment. Updating the regulations will facilitate the wider use of this technology and make map production processes more efficient and less time-consuming.

References

1. Pu S, Vosselman G. Knowledge-based reconstruction of building models from terrestrial laser scanning data. ISPRS J Photogramm Remote Sens. 2009;64(6):575–84. doi: 10.1016/j.isprsjprs.2009.04.001.
2. Leite F, Akcamete A, Akinci B, Atasoy G, Kiziltas S. Analysis of modeling effort and impact of different levels of detail in building information models. Autom Constr. 2011;20:601–9. doi: 10.1016/j.autcon.2010.11.027.
3. Quagliarini E, Clini P, Ripanti M. Fast, low-cost and safe methodology for the assessment of the state of conservation of historical buildings from 3D laser scanning: The case study of Santa Maria in Portonovo (Italy). J Cult Herit. 2017;24:175–83. doi: 10.1016/j.culher.2016.10.006.
4. Taddia Y, González-García L, Zambello E, Pellegrinelli A. Quality assessment of photogrammetric models for façade and building reconstruction using DJI Phantom 4 RTK. Remote Sens. 2020;12(19):3144. doi: 10.3390/rs12193144.
5. Day D, Weaver W, Wilsing L. Accuracy of UAS photogrammetry: A comparative evaluation. Photogramm Eng Remote Sensing. 2016;82(12):909-14. doi: 10.14358/PERS.82.12.909.
6. Sanz-Ablanedo E, Chandler JH, Rodríguez-Pérez JR, Ordóñez C. Accuracy of unmanned aerial vehicle (UAV) and SfM photogrammetry survey as a function of the number and location of ground control points used. Remote Sens. 2018;10(10):1606. doi: 10.3390/rs10101606.
7. Elkhrachy I. Accuracy assessment of low-cost unmanned aerial vehicle (UAV) photogrammetry. Alexandria Eng J. 2021;60:5579–90. doi: 10.1016/j.aej.2021.04.011.
8. Ansari A. Use of point cloud with a low-cost UAV system for 3D mapping. In: Proceedings of the 2012 International Conference on Emerging Trends in Electrical Engineering and Energy

Management (ICETEEEM); 2012 Dec 13-15; Chennai, India. IEEE; 2012. p. 131-134. doi: 10.1109/ICETEEEM.2012.6494471.

9. Daponte P, De Vito L, Mazzilli G, Picariello F, Rapuano S. A height measurement uncertainty model for archaeological surveys by aerial photogrammetry. Measurement. 2017;98:192-8. doi: 10.1016/j.measurement.2016.11.033.

10. Sun S, Wang B. Low-altitude UAV 3D modeling technology in the application of ancient buildings protection situation assessment. Energy Procedia. 2018;153:320–4. doi: 10.1016/j.egypro.2018.10.082.

11. Vitale V. The case of the middle valley of the Sinni (Southern Basilicata). Methods of archaeological and architectural documentation: 3D photomodelling techniques and use of RPAS. Digit Appl Archaeol Cult Herit. 2018;11:e00084. doi: 10.1016/j.daach.2018.e00084.

12. Zheng X, Wang F, Li Z. A multi-UAV cooperative route planning methodology for 3D fine-resolution building model reconstruction. ISPRS J Photogramm Remote Sens. 2018;146:483–94. doi: 10.1016/j.isprsjprs.2018.11.004.

13. Mavroulis S, Andreadakis E, Spyrou NI, Antoniou V, Skourtsos E, Papadimitriou P, et al. UAV and GIS-based rapid earthquake-induced building damage assessment and methodology for EMS-98 isoseismal map drawing: The June 12, 2017 Mw 6.3 Lesvos earthquake. Int J Disaster Risk Reduct. 2019;37:101169. doi: 10.1016/j.ijdrr.2019.101169.

14. Jones CA, Church E. Photogrammetry is for everyone: Structure-from-motion software user experiences in archaeology. J Archaeol Sci Rep. 2020;30:102261. doi: 10.1016/j.jasrep.2020.102261.

15. Hill AC, Laugier EJ, Casana J. Archaeological remote sensing using multi-temporal, drone-acquired thermal and near infrared (NIR) imagery: A case study at the Enfield Shaker Village, New Hampshire. Remote Sens. 2020;12(4):690. doi: 10.3390/rs12040690.

16. Ekaso D, Nex F, Kerle N. Accuracy assessment of real-time kinematics (RTK) measurements on unmanned aerial vehicles (UAV) for direct geo-referencing. Geo-Spatial Inf Sci. 2020;23(2):165–81. doi: 10.1080/10095020.2019.1710437.

17. Eltner A, Sofia G. Structure from motion photogrammetric technique. Developments in Earth Surface Processes. Amsterdam: Elsevier; 2020. Vol. 23, p. 1–24. doi: 10.1016/B978-0-444-64177-9.00001-1.

18. Stott E, Williams RD, Hoey TB. Ground control point distribution for accurate kilometre-scale topographic mapping using an RTK-GNSS unmanned aerial vehicle and SfM photogrammetry. Drones. 2020;4(3):55. doi: 10.3390/drones4030055.

19. Benassi F, Dall'Asta E, Diotri F, Forlani G, di Cella UM, Roncella R, et al. Testing accuracy and repeatability of UAV blocks oriented with GNSS-supported aerial triangulation. Remote Sens. 2017;9(2):172. doi: 10.3390/rs9020172.

20. Varbla S, Pusst R, Ellman A. Accuracy assessment of RTK-GNSS equipped UAV conducted as-built surveys for construction site modelling. Surv Rev. 2020;53(381):477–92. doi: 10.1080/00396265.2020.1830544.

21. TMMOB Harita ve Kadastro Mühendisleri Odası. Büyük Ölçekli Harita ve Harita Bilgileri Üretim Yönetmeliği [Internet]. Ankara: TMMOB Harita ve Kadastro Mühendisleri Odası; 2018. [cited 2024 Nov 25] Available from: https://www.harita.gov. tr/uploads/files/regulations/buyuk-olcekli-harita-ve-harita-bilgileri-uretim-yonetmeligi-65.pdf

22. Pix4D. Pix4D Documentation [Internet]. [cited 2024 Nov 25] Available from: https://support.pix4d.com/hc/en-us/articles/202557489

23. TUSAGA-AKTİF. Türkiye Ulusal Sabit GNSS Ağı-Aktif. [cited 2024 Nov 25] Available from: https://www.tusaga-aktif.gov.tr/

24. Harwin S, Lucieer A. Assessing the accuracy of georeferenced point clouds produced via multi-view stereopsis from unmanned aerial vehicle (UAV) imagery. Remote Sens. 2012;4(6):1573–99. doi: 10.3390/rs4061573.

25. Štroner M, Urban R, Reindl T, Seidl J, Broucek J. Evaluation of the georeferencing accuracy of a photogrammetric model using a quadrocopter with onboard GNSS RTK. Sensors. 2020;20(8):2318. doi: 10.3390/s20082318.

26. Taddia Y, Stecchi F, Pellegrinelli A. Using DJI Phantom 4 RTK drone for topographic mapping of coastal areas. ISPRS Int Arch Photogramm Remote Sens Spat Inf Sci. 2019;XLII-2/W13:625–30. doi: 10.5194/isprs-archives-XLII-2-W13-625-2019.

27. James MR, Robson S, d'Oleire-Oltmanns S, Niethammer U. Optimising UAV topographic surveys processed with structure-from-motion: Ground control quality, quantity and bundle adjustment. Geomorphology. 2017;280:51–66. doi: 10.1016/j.geomorph.2016.11.021.

28. Woodget AS, Carbonneau PE, Visser F, Maddock IP. Quantifying submerged fluvial topography using hyperspatial resolution UAS imagery and structure from motion photogrammetry. Earth Surf Process Landf. 2015;40:47–64. doi: 10.1002/esp.3613.

29. Woodget AS, Austrums R, Maddock IP, Habit E. Drones and digital photogrammetry: From classifications to continuums for monitoring river habitat and hydromorphology. WIREs Water. 2017;4:e1222. doi: 10.1002/wat2.1222.

30. Martinez-Carricondo P, Agüera-Vega F, Carvajal-Ramirez F, Mesas-Carrascosa F-J, Garcia-Ferrer A, Perez-Porras F-J. Assessment of UAV-photogrammetric mapping accuracy based on variation of ground control points. Int J Appl Earth Obs Geoinf. 2018;72:1–10. doi: 10.1016/j.jag.2018.05.015.

31. Kahveci M. Kinematik GNSS ve RTK CORS Ağları. Ankara: Nobel; 2017.

32. DJI Enterprise. DJI Mavic 3 Enterprise Specs. [cited 2024 Nov 25] Available from: https://enterprise.dji.com/mavic-3-enterprise/specs

33. Enterprise. DJI Terra. [cited 2024 Nov 25] Available from: https://enterprise.dji.com/dji-terra

34. Gehan EA. A generalized Wilcoxon test for comparing arbitrarily singly-censored samples. Biometrika. 1965;52(1-2):203–24. doi: 10.1093/biomet/52.1-2.203.

35. Shapiro SS, Wilk MB. An analysis of variance test for normality (complete samples). Biometrika. 1965;52(3-4):591–611. doi: 10.2307/2333709.

36. Hedberg EC, Ayers S. The power of a paired t-test with a covariate. Soc Sci Res. 2015;50:277–91. doi: 10.1016/j.ssresearch.2014.12.004.

Polyethylenimine-Assisted Aggregation of β-Galactosidase from Kluyveromyces lactis

Nedim Albayrak* ⓘ | Rabia Akyol Kütük ⓘ
Hitit University, Department of Food Engineering, 19030, Corum, Türkiye.

Corresponding Author
Nedim Albayrak
E-mail: nedimalbayrak@hitit.edu.tr Phone: +90(364) 227 45 33 Fax: +90(364) 227 45 33
RORID: https://ror.org/01x8m3269

Cite As
Albayrak N, Kütük R, A. Polyethylenimine-Assisted Aggregation of β-Galactosidase from Kluyveromyces lactis. Hittite J Sci Eng. 2024;11(3):149-156.

Peer Review: Evaluated by independent reviewers working in at least two different institutions appointed by the field editor.
Ethical Statement: Not available.
Plagiarism Checks: Yes - iThenticate
Conflict of Interest: The authors affirm that, to the best of their knowledge, there is no conflict of interest or common interest with any institution, organization, or individual that could influence the review process of the paper.

CRediT AUTHOR STATEMENT
Rabia Akyol Kütük: Carried out the experimental studies, establishment of methodology and preparation first draft of the report.
Nedim Albayrak: Performed the investigation, conceptualization and visualization of the data and finally supervision, writing and editing final draft.

Polyethylenimine-Assisted Aggregation of β-Galactosidase from Kluyveromyces lactis

Nedim Albayrak* | Rabia Akyol Kütük

Hitit University, Department of Food Engineering, 19030, Corum, Türkiye.

Abstract

Using PEI as an aggregating agent with β-galactosidase from Kluyveromyces lactis was investigated with no solid support. PEI, a cationic polymer initiated instant aggregation with the enzyme in solution. The factors affecting the aggregation such as PEI to enzyme ratio, glutar aldehyde for cross-linking and pH were investigated. Aggregation and sedimentation as well as the residual activity of aggregates were effectively dependent on the PEI to enzyme ratios. Easily precipitating aggregates at the ratio of 1/8, PEI enzyme aggregates were able to contain all enzyme in the complexation and displayed 60% of initial lactase activity. The PEI aggregation of enzyme led to enhancements in chemical and physical characteristics compered to free enzyme. The soluble enzyme showed a narrow optimum at about pH 7 while pH optimum of the aggregates extended one pH unit toward the alkaline range. Upon overnight incubation at 40 ºC, aggregated enzyme displayed 30% greater stability on average at all pHs tested. Although the free enzyme showed the highest activity at 40°C, it rapidly lost 50% of its activity at 50°C. In contrast, the aggregated enzyme retained full activity at 50°C and 70% activity at 65°C. With markedly enhanced thermal stability, the half-life of the aggregated enzyme increased from 76 hours to 254 hours at 40°C. Overall, the simple and rapid aggregation of PEI with the enzyme led to instant and intense clustering, resulting in higher thermal and pH stabilities. This method may potentially offer efficient and cost-effective catalysis in lactase conversion processes.

Keywords: Kluyveromyces lactis, Lactase, Carrier-Free, PEI-Enzyme Aggregation, Stabilization, PEI, GA

INTRODUCTION

Compared to free enzymes, immobilized enzymes are more suitable for industrial applications as they offer ease of separation from the reaction medium and reuse and are more resistant to environmental conditions such as temperature and pH (1–4). Solid supports are generally used in enzyme immobilization for holding the enzyme in a fixed region (5). However, these supports do not provide any catalytic function, despite occupying over 95% of the catalyst volume or mass (6,7). As an alternative approach to immobilize enzymes on solid supports is to turn enzyme mass into macromolecular aggregate such as Cross-Lined Enzyme Aggregate (CLEA). The approach has been evaluated in some applications with beneficial aspects (8,9). However, the method requires to use extensive amount of organic solvent for enzyme precipitation (10) suffers from diffusional resistance (11) due to cross-linking of the precipitated enzyme into a dense structure.

Enzyme aggregation can also be achieved with the assistance of another polymer such as polyethyleneimine (PEI) which tentatively forms electrostatic complexes with negatively charged enzymes while cushioning the space among enzymes and aiding conformational stability (12,13). This approach has the benefits for avoidance of organic solvent thus lowering the cost and suffer relatively limited diffusional resistance due to open structure (14,15). This type of aggregated enzyme exhibits soluble enzyme characteristics during the enzymatic reaction but can be reversibly recovered through physical separation after the reaction and reused (1,16). PEI is an inexpensive and safe polymer with various industrial and biomedical applications (17,18), thus can be easily approved GRAS (Generally Recognized As Safe) in the bioprocessing of food ingredient for contact (18,19).

The general goal of the study was to focus on polymer-assisted aggregation of β-galactosidase (lactase) from Kluyveromyces lactis to effectively increase catalyst density and the operational stability while performing in solution as staying afloat for dairy applications. The enzyme is frequently used in the dairy industry and classified under GRAS substances, making it commercially prevalent (20). The lactase is also notable for its long lifespan at around 35°C, its optimal pH of 6.5-7.5 (21), which is close to the neutral pH of milk and sweet whey, and its relatively low Km value of 20 mM for lactose (22,23), making it one of the most suitable enzymes for lactose hydrolysis at neutral pH (20,22). Additionally, it stands out for its ability to achieve around 30% GOS yield with 70% lactose utilization in GOS production (24,25).

The main goal of the current study is to enhance the performance of the lactase as a catalyst for industrial processes such as lactose hydrolysis and oligosaccharide synthesis. Many issues in enzymatic production arise from inadequate catalyst performance (26). When examining the performance of immobilized enzymes for oligosaccharide production, problems like low activity, short lifespan under production conditions, insufficient stability, and expensive costs are observed (27,28). We have previously immobilized lactase from K. lactis using PEI on the surface of plasma modified cellulose acetate membranes and found that high enzyme loading on the surface did not necessarily resulted in higher rates of catalysis largely due to restriction of enzyme movement (29). To address these issues, the project aims to use a multi-layer system to concentrate the enzyme in solution, thereby improving catalytic performance to meet industrial expectations and reducing the cost for enzyme usage (22,26).

In this study, the aggregation of the lactase enzyme derived from K. lactis using polyethyleneimine (PEI) was investigated without involving any support or solvent for precipitation. Aggregated enzymes offer several advantages, including high catalyst density, minimal or no diffusional resistance, simple and rapid aggregation, and low cost for catalysis (30,31).

The study focused on the aggregation of the Kluyveromyces lactis-derived lactase enzyme with PEI, exploring the optimal PEI/enzyme ratio and characterizing some properties of the aggregated clusters of the enzyme in solution.

MATERIALS AND METHODS

Enzyme and Reagents

β-galactosidase from Kluyveromyces lactis (Lactozym® Pure 2600 L) obtained from Novozymes (Novo Nordisk, Denmark) was used for in immobilization experiments. For enzyme immobilization, polyethyleneimine (PEI) (30% (w/v) aqueous solution, average molecular weight: 50,000-100,000) was from Merck (Darmstadt, Germany), while glutaraldehyde (GA, 50% (w/v)) was obtained from AppliChem (Darmstadt, Germany). All solutions of PEI and GA were prepared using distilled water. Where necessary, pH adjustments were made using HCl or NaOH solutions (Merck). Lactose (D-Lactose monohydrate) and phosphate buffers were from Sigma (USA).

PEI-Enzyme Aggregation

To investigate the effect of different PEI concentrations on the PEI-enzyme-aggregation, PEI solutions of varying concentrations were prepared by diluting a 1% PEI stock solution with distilled water. 1 mL volumes of these PEI solutions were mixed with 0.5 mL of enzyme solution in microcentrifuge tubes. The mixtures were briefly vortexed, and the formation of a milky turbidity was observed. To assess whether the resulting PEI-enzyme aggregates were strong or dense enough to precipitate, the mixtures were centrifuged at 10,000 rpm for 2 minutes. The formation of a precipitate before and after centrifugation of the PEI-enzyme suspensions was observed (Figure 1). Enzyme activity was analyzed using samples taken from the free enzyme solution, the turbid PEI-lactase aggregation solution formed after mixing the PEI and enzyme solutions, and the supernatant remaining after centrifugation.

Glutaraldehyde Cross-Linking

To crosslink the PEI-lactase-aggregates formed in solution, 0.1 mL of GA solutions containing 0.01% to 0.20% GA were added and incubated at ambient temperature for 5 to 10 minutes. The GA solutions were prepared in distilled water and applied following the formation of the PEI-enzyme aggregates.

Enzyme Assay

Enzyme activity was determined using a spectrophotometric assay comprising o-nitrophenyl-beta-D-galactopyranoside (o-NPG, Sigma) as the substrate. The reaction was initiated by adding 0.1 mL of enzyme solution to a mixture containing 1.5 mL of 0.1 M sodium phosphate reaction buffer (pH 7) and 0.2 mL of 2 mM o-NPG. The reaction mixture was incubated at 37°C for 5 minutes and the reaction was stopped by adding 0.5 mL of 1 M sodium carbonate (Merck) solution. The absorbance was then measured at 420 nm using a spectrophotometer (Shimadzu UV-1800, Japan). As a blank, 0.1 mL of 0.1 M sodium phosphate buffer (pH 7) was used instead of the enzyme extract. One unit of beta-galactosidase activity was defined as the amount of enzyme that releases 1 µmol of o-nitrophenol per minute.

Temperature and pH Optimum

The effects of temperature and pH on the activities of free enzyme and PEI-enzyme aggregate in solution were investigated. Relevant pH values ranging from 4.5 to 8.0 were achieved using 50 mM phosphate buffers to determine the effect of pH on enzyme activities at 37°C. The effects of various temperatures ranging from 30 to 65°C on enzyme activities were determined according to the enzyme assay. The activities obtained under the varying pH or temperatures were indicated as relative activities for comparisons among the pH levels or temperatures to observe the variation between the soluble and aggregated lactase.

Temperature and pH Stability

The changes in the activities of free enzyme and PEI enzyme aggregates were measured at room temperature for 18 hours in buffer solutions with a pH range of 5.0-8.0. The residual activities were determined at the end of incubation period. Thermal deactivation is the best indication for the loss of activity under process conditions in free or aggregated enzymes. Thus, the half-lives of PEI enzyme aggregates and free enzyme were determined from the incubation at three different temperatures (30, 40, and 50°C) in buffer solutions (pH 7) During the storage period for 60 minutes, samples were taken at specific intervals to determine the remaining activities of the enzymes, and the changes in activity were comparatively examined. From the residual activity levels for each temperature, the temperature stability of a soluble enzyme and PEI-enzyme aggregate was determined by plotting the natural logarithm of the rate constants against the reciprocal of temperatures [lnk vs 1/T (K)]. The slope of the fitted straight line, deactivation constants k_d (h^{-1}) and also t 1/2 (h), were determined (Table 1.).

Table 1 Comparison of temperature stabilities of soluble lactase and PEI-lactase aggregate at PEI to enzyme ratio of 1/8 during 60 minutes of incubations at pH 7.0 .

(°C)	Soluble Enzyme $t_{1/2}$(h)	PEI-Enzyme Aggregate $t_{1/2}$(h)
30	224	1358
40	76	254
50	1	72

Storage stability at ambient temperature for three weeks was also determined for the soluble enzyme and PEI-lactase aggregate at PEI to enzyme ratio of 1/8 in buffer (pH 7). Residual enzyme activities were determined and expressed as relative activity compared with the initial activity.

RESULTS AND DISCUSSION

PEI-Lactase Aggregation

The aggregating characteristics of lactase enzyme from K. lactis within PEI polymer matrix through electrostatic interactions was first studied. The goal of the approach was to create concentrated enzyme clusters as aggregates while performing as good as soluble enzymes. A successful formation of the colloidal electrostatic complexes between PEI and the enzyme considered is a key to achieving effective and stable enzyme clustering. Therefore, several success criteria were tentatively set to maximize the yield efficiency of the PEI enzyme aggregation. First, PEI and enzyme associates lead to milky complex formation. Second, a complete PEI-enzyme complexation can be achieved at a certain PEI to enzyme ratio, where PEI and enzyme aggregation gather most of the enzyme activity/protein in turn diminishing the unbound enzyme activity/protein in solution. Third, PEI-enzyme aggregates catalytically function as good as soluble enzymes while easily and reversibly separated from the medium by means of simple filtration or centrifugation. Finally, the aggregation leads to greater stability for a longer operational lifespan.

Figure 1 shows the schematic representation of PEI-enzyme monolog complex formation and aggregation, along with photographs of the enzyme clusters. PEI, with a molecular weight range of 100,000 to 750,000, spreads into the solution as a cationic polar polymer. In contrast, the enzyme, with a molecular weight range of 100,000 to 200,000 and an isoelectric point of 4-6, is smaller and anionic compared to PEI. This results in the formation of several smaller enzyme particles that aggregate with PEI into beads, which then attract each other to form clusters. The colloidal milky appearance of the PEI-enzyme solution is attributed to this mechanism.
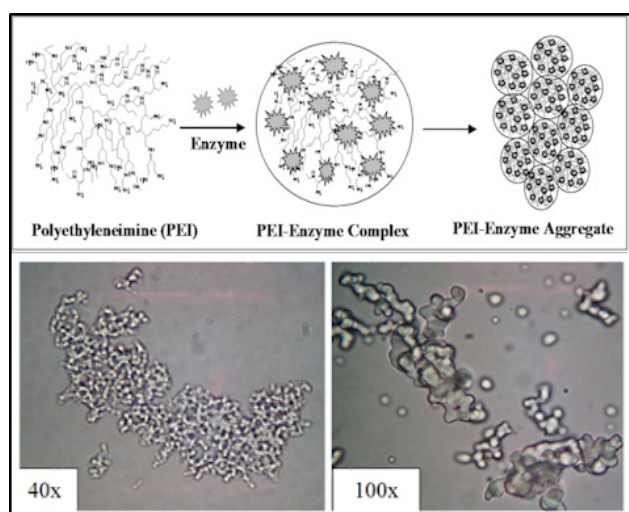

Figure 1 The proposed mechanism of aggregation of PEI and free enzyme in solution, and photographs of the resulting aggregate taken under a light microscope at 40x and 100x magnification.

In a specific ratio of PEI to enzyme, the clustering of all free enzymes within PEI matrices gently floating in the solution was anticipated and targeted. The resulting aggregation was evaluated by precipitating through centrifugation, serving as an indicator of the density or the strength of the interaction between PEI and the enzyme. Subsequently, the aim was to minimize enzyme activity remaining in the supernatant after centrifugation, as enzyme activity was only expected from the PEI-lactase aggregates. Therefore, an experiment was carried out to determine the optimal PEI concentration (i.e., PEI to enzyme ratio) that formed a complex with the enzyme, resulting in a milky structure with minimal decline in the enzyme activity associated with sedimenting aggregates. The measurements of enzyme activity without PEI were taken as control parameters for the evaluation of the activities in the PEI enzyme aggregates prior to centrifugation and the supernatant at 10,000 rpm for 2 minutes. The effects of varying conditions were evaluated based on enzyme activity. Higher enzyme activity in the aggregate or lower activity in the supernatant were considered more effective for aggregation, indicating the optimal PEI to enzyme ratio.

Figure 2 Images of PEI-enzyme aggregates with different concentrations of PEI from highest (1/1) to lowest ratio (1/16) and K. lactis lactase Lactozyme 2600L enzyme samples (1/300 dilution) before (a) and after (b) centrifugation (10,000 rpm for 2 minutes).

Figure 2 provides visual evidence of the aggregation of K. lactis lactase with different PEI concentrations before (a) and after (b) centrifugation. When PEI solutions prepared with distilled water (ranging from 1/1 to 1/16) were added to the diluted enzyme solutions in microcentrifuge tubes, a significant turbidity was observed, indicating that PEI caused the enzyme samples to aggregate. The visual appearance of

the turbidity and intensity varied in the 1/1 toward 1/8 mixtures but less intense in the 1/16, indicating a direct relationship between turbidity and PEI concentration, and notably the turbidity moved with the mixing of the aggregate solution. In the 1/1 and 1/2 samples with the highest PEI concentrations, some PEI-enzyme aggregates did not precipitate and remained suspended in the solution.
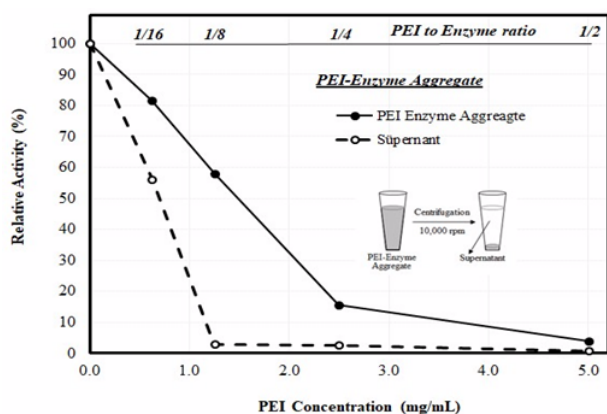

Figure 3 The enzyme activities of PEI-enzyme aggregates and the supernatant thereafter. The effect of PEI concentration from highest (1/1) to lowest ratio (1/16) on the aggregation of PEI and K. lactis lactase (Lactozyme 2600L) enzyme.

By observing the visual images of samples in Figure 2a and 2b and corresponding the levels of the enzyme activities for the PEI-lactase aggregates in Figure 3 before and after centrifugation, one can evaluate the effectiveness of PEI in promoting enzyme aggregation with minimal enzyme loss and optimize the PEI concentration to achieve maximal activity. Increasing PEI to enzyme ratio resulted in a gradual decline in enzyme activity for PEI-enzyme aggregate. At the lowest PEI to enzyme ratio (1/16), the aggregates showed 80% of initial activity; however, 60% remained in the supernatant upon spinning. At the ratio of 1/8, the PEI-enzyme aggregates showed 60% enzyme activity whereas no enzyme activity was detected in the supernatant, which coincides well with the visual clarity of the supernatant. At higher ratios (1/4), less than 20% of the enzyme activity associated with the aggregates while no activity was detected in the supernatant.

GA cross-linking is the final step for permanent fixation of the PEI-enzyme aggregates, which can be disrupted by negatively charged molecules (30). When using a solution GA ranging from 0.01% to 0.20% applied for 5-10 minutes showed no significant difference in either the PEI-lactase clustering or turbidity, nor in enzyme activity. Therefore, 0.1% GA solution treatment for 10 min was used to cross-link the aggregates for further studies (data was not shown). Rapid cross-linking effects were obtained regarding the effects of GA on the enzyme activity and aggregation characteristics with PEI for lipase enzymes (32).

The success in immobilization of an enzyme usually relies

on projected favorable chemical interactions. Enzyme aggregation with PEI is an example of such molecular interactions (33). As seen in Figure 3, increase in PEI to enzyme ratio regrettably resulted in greater decline in the activity of the PEI enzyme aggregates. Although the activity yield of 60% is the best result currently obtained, probable causes could be attributed to steric hindrance and rendered flexibility of the PEI aggregated enzyme. Interaction of enzymes with PEI was often expected to result in aggregation, but the activity of the aggregates depends on a number of factors that are difficult to predict, including pH, presence of impurities, surface chemistry, the chemical characteristics of the active site, etc (34). To explore these unknowns requires comprehensive analytical studies. Nevertheless, some of the reasons can be attributed to the complex properties of lactase from K.lactis. It was reported in several studies that the enzyme was nearly 240 kDa in size, composed of two nonidentical monomers (35) and largely dominated with beta-strands secondary structure (21) with a need of space for motility. The stability of lactase from K.lactis is increased by phosphate ions and glycerol (23,36); therefore, the enzyme samples may likely contain some amount of phosphates and glycerol. Exclusion of these stabilizers from the enzyme conformation could have reduced the activity of the aggregated enzyme.

Characterizations for PEI-Lactase Aggregate

Considering the fact that most efficient PEI-enzyme aggregation and precipitation outcomes were obtained at PEI to enzyme ratio of 1/8, the ratio and the same aggregation conditions were used for the characterization studies.
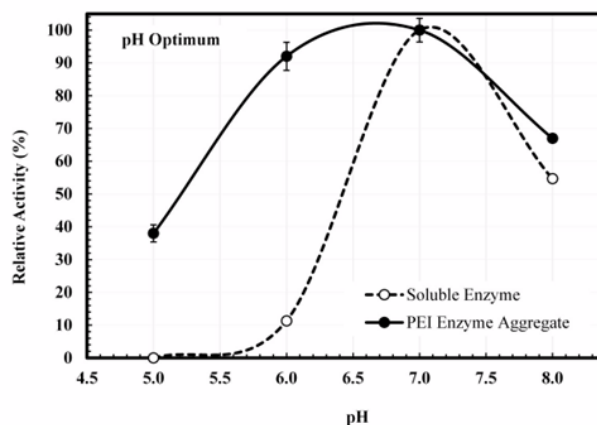

Figure 4 The effects of pH on the activities of soluble lactase and PEI-lactase aggregate at PEI to enzyme ratio of 1/8 with Lactozyme 2600L (enzyme activities were measured at 40°C).

Optimal pH

Compared with the soluble enzyme, the effects of pH and temperature on the enzyme activities for the PEI-lactase aggregates were determined and results were displayed in Figure 4. While the optimum pH value for the free enzyme was 7.0 and rather quickly lost 90% of activity at pH 6, exhibiting

a narrower optimal pH range. In contrast, the aggregated enzyme retained over 90% of its activity between pH 6.0 and 7.0 revealing broader optimal pH and noticeably shifted optimal activity towards acidic pH of 6.5-7.0. There was a minimal increase in activity at pH 8. Our results in terms of soluble enzyme very well agreed with the findings of various studies (21,37) where the structure-activity relationship as a function of the pH was investigated and they showed that the highest activity conveying the highest secondary structure content was found at pH 7.0. Enzyme exhibited structural change from pH 7.0 to 6.5, which was accompanied by a decline in the activity significantly with probable variations in critical residues (21). We can also deduce from the study that PEI-enzyme aggregation was able to withstand the structural change due to preserving nearly full activity between pH 6.0 and 7.0. Owing to the eminent electrostatic interaction between enzyme and PEI, changes in optimal pH and extension toward acidic (38) or alkaline ranges (32) were often observed depending on the enzyme. The change in optimal pH can be attributed to alterations in the charged residues of PEI molecules in the local vicinity surrounding the enzyme.
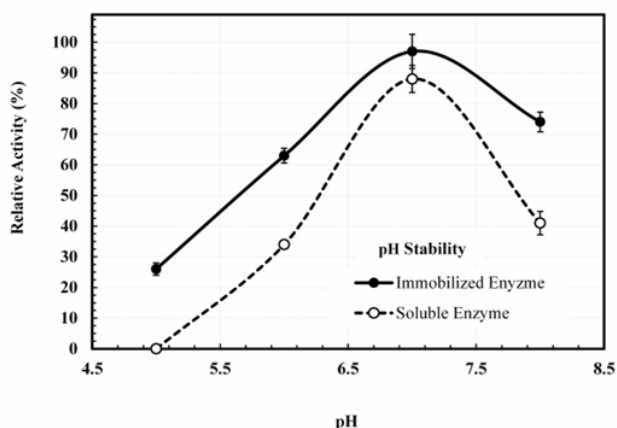

Figure 5 The effects of pH on the stabilities of soluble lactase and PEI-lactase aggregate at PEI to enzyme ratio of 1/8 (the enzyme activities were measured at 40°C after 18h of incubation).

pH stability

For evaluation of pH stability, Figure 5 compares the residual activities of the soluble lactase and PEI-lactase aggregates stored at various pHs from 5.0 to 8.0 for 18 hours of incubation at 40°C. The PEI-lactase aggregate exhibits about 30% greater stability across a range of pH values compared to the soluble lactase. Although the activities of both enzymes are maximized at pH 7.0, the PEI-lactase aggregate show a broader optimal pH range or higher stability within the same range compared to the soluble enzyme. PEI may act as an intermediary for chemical interactions among the local charges, stabilizing their positions and mitigating disruptive forces (17,39). Therefore, it may be more tolerant to pH changes during catalysis (31,39). Enhanced pH stability of the PEI-lactase aggregate means it is more versatile for

various industrial processes over a wider range of conditions thus potentially deliver more efficient and cost-effective applications(40,41).
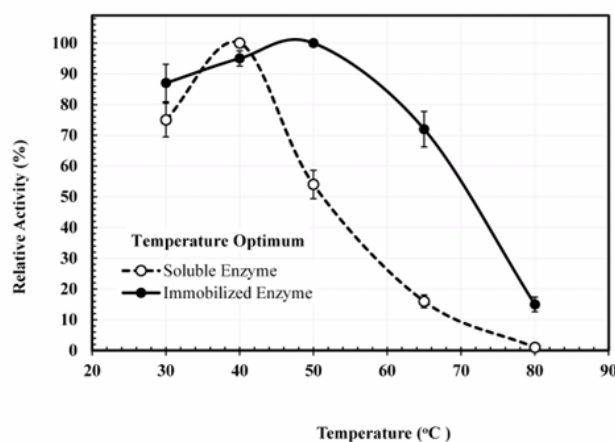

Figure 6 The effects of temperature on the activities of soluble lactase and PEI-lactase aggregate at PEI to enzyme ratio of 1/8 (pH 7).

Optimal Temperature

The effects of temperature on the enzyme activities of PEI-lactase aggregates were compared to those of the free enzyme at different temperatures in Figure 6. The free enzyme showed the highest activity at 40ºC, but it rapidly diminished its activity at increasing temperatures e.g., 50% residual activity remained at 50ºC. In contrast, the PEI-aggregated enzyme is able to preserve greater activity at higher temperatures e.g., retained full activity at 50ºC and 70% at 65ºC. The PEI-lactase aggregate clearly exhibited a broader optimal temperature range including 50ºC underlining higher stability at elevated temperatures. Similar to our results, it was reported that the enzyme optimum temperature at nearby 30 - 35oC (37) but quickly deactivated at 50oC (23).
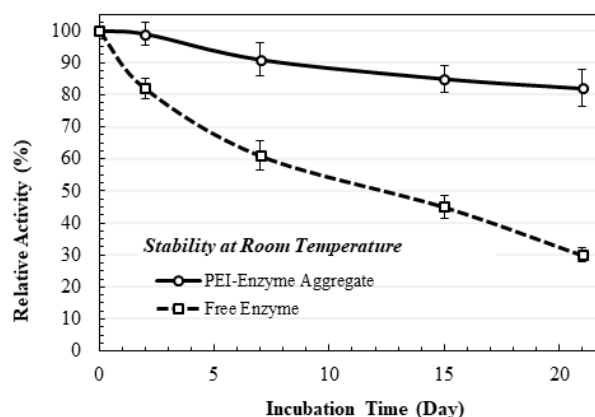

Figure 7 The effects of storage stability at room temperature for the soluble lactase and PEI-lactase aggregate at PEI to enzyme ratio of 1/8 (pH 7).

Figure 7 compared the storage stabilities of soluble lactase and PEI-lactase aggregates at room temperature for their

extended storage. The PEI-lactase aggregate showed significantly higher stability, retaining a higher percentage of its initial activity over the same period compared to the soluble lactase. The figure demonstrates that the PEI-lactase aggregate has superior storage stability at room temperature compared to the soluble lactase. This increased stability makes the PEI-aggregated enzyme more effective for long-term use in industrial applications. It was reported that the enzyme is stable at room temperature for several days (23). However, our results showed that soluble enzyme lost 50% of initial activity in 10 days.

Storage and Temperature Stabilities

Table 1 summarized the temperature stabilities of the soluble and the aggregated enzyme in buffers (pH 7.0) incubated at varying temperatures for 60 minutes. The thermal stability of the PEI-aggregated lactase increased significantly compared to the soluble enzyme. At 40°C, the half-life ($t_{1/2}$) of the soluble enzyme increased from 76 to 254 hours with PEI aggregation. Additionally, the deactivation energy for the soluble enzyme decreased from 210 kJ/mol to 105 kJ/mol for the PEI-aggregated enzyme, indicating a substantial increase in enzyme stability (from the Arrhenius plot, plot lnk vs 1/T (K)). The thermal stability and kinetic behavior of enzymes, particularly when aggregated or immobilized with agents like polyethyleneimine (PEI), are crucial for optimizing industrial applications (42). Studies have shown that PEI aggregation can significantly enhance the stability of enzymes, such as lactase (30). For example, similar research on other enzymes like amyloglucosidase and lipases has demonstrated notable improvements in thermal stability and deactivation energy with immobilization techniques. High temperatures are beneficial for enzyme-catalyzed reactions not only to get higher reaction rates but also to avoid microbial contamination (43).

CONCLUSIONS

Using only PEI as an aggregating polymer, large clusters of PEI-enzyme particles were formed with β-galactosidase from Kluyveromyces lactis. PEI likely formed multiple polar ionic bonds with the enzyme molecules, causing them to link together into large, visible aggregates. At an optimal PEI to enzyme ratio, precipitating PEI-enzyme aggregates encapsulated all the enzyme during complexation and retained the majority of its initial activity. This study demonstrated that PEI, as a safe and inexpensive cationic polymer, could be used to form large clusters of PEI-lactase aggregates that preserve most of the initial enzyme activity and significantly enhance thermal and pH stability, thereby greatly extending the operational lifespan. PEI may act as intermediary shield for chemical interactions and physical forces among the groups within and among the enzyme by keeping the groups in place. The approach offers simple, rapid, and low-cost means to concentrate and stabilize the enzyme activity. In order to derive information regarding the type of interaction and mode of association with PEI and enzyme, further experiments could be conducted to explore the exact nature of the thermal stability and activity differences, possibly incorporating the analytical techniques and optimization strategies along with varying characteristics of enzymes and polymers.

References
1. Eldin MS, Mita DG. Immobilized Enzymes: Strategies for Overcoming the Substrate Diffusion- Limitation Problem. Curr Biotechnol. 2014;3(3):207–17.
2. Schoffelen S, van Hest JCM. Chemical approaches for the construction of multi-enzyme reaction systems. Curr Opin Struct Biol. 2013 Aug;23(4):613–21.
3. Numanoğlu Y, Sungur S. β-Galactosidase from Kluyveromyces lactis cell disruption and enzyme immobilization using a cellulose–gelatin carrier system. Process Biochem. 2004 Feb [cited 2011 Nov 26];39(6):705–11.
4. Remaut K, Lucas B, Raemdonck K, Braeckmans K, Demeester J, De Smedt SC. Protection of oligonucleotides against enzymatic degradation by pegylated and nonpegylated branched polyethyleneimine. Biomacromolecules. 2007 Apr;8(4):1333–40.
5. Velasco-Lozano S, López-Gallego F, Rocha-Martin J, Guisán JM, Favela-Torres E. Improving enantioselectivity of lipase from Candida rugosa by carrier-bound and carrier-free immobilization. J Mol Catal B Enzym. 2016;130:32–9.
6. Parthasarathy R V, Martin CR. Synthesis of polymeric microcapsule arrays and their use for enzyme immobilization. Nature. 1994 May 26;369(6478):298–301.
7. Roessl U, Nahálka J, Nidetzky B. Carrier-free immobilized enzymes for biocatalysis. Biotechnol Lett. 2010 Mar [cited 2011 Aug 30];32(3):341–50.
8. Hustad GO, Richardson T, Olson NF. Immobilization of B-Galactosidase on an Insoluble Carrier with a Polyisocyanate Polymer . I . Preparation and Properties. J Dairy Sci. 1973;56(9):1111–7.
9. Grajales-Hernández DA, Velasco-Lozano S, Armendáriz-Ruiz MA, Rodríguez-González JA, Camacho-Ruíz RM, Asaff-Torres A, et al. Carrier-bound and carrier-free immobilization of type A feruloyl esterase from Aspergillus niger: Searching for an operationally stable heterogeneous biocatalyst for the synthesis of butyl hydroxycinnamates. J Biotechnol. 2020;316(March):6–16.
10. Dal Magro L, Hertz PF, Fernandez-Lafuente R, Klein MP, Rodrigues RC. Preparation and characterization of a Combi-CLEAs from pectinases and cellulases: A potential biocatalyst for grape juice clarification. RSC Adv. 2016;6(32):27242–51.
11. Wilson L, Illanes AA, Romero O, Vergara JJ, Mateo CC. Carrier-bound and carrier-free penicillin acylase biocatalysts for the thermodynamically controlled synthesis of [beta]-lactam compounds in organic medium. Enzyme Microb Technol. 2008 Nov 6 [cited 2011 Nov 26];43(6):442–7.

12. Suh J, Lee SH, Kim SM, Hah SS. Conformational Flexibility of Poly(ethylenimine) and Its Derivatives. Bioorg Chem. 1997 Aug;25(4):221–31.

13. Cui C, Tao Y, Li L, Chen B, Tan T. Improving the activity and stability of Yarrowia lipolytica lipase Lip2 by immobilization on polyethyleneimine-coated polyurethane foam. J Mol Catal B Enzym. 2013;91:59–66.

14. Santos JP, Welsh ER, Gaber BP, Singh A. Polyelectrolyte-assisted immobilization of active enzymes on glass beads. Langmuir. 2001;17(17):5361–7.

15. Bucatariu F, Ghiorghita C-A, Simon F, Bellmann C, Dragan ES. Poly(ethyleneimine) cross-linked multilayers deposited onto solid surfaces and enzyme immobilization as a function of the film properties. Appl Surf Sci. 2013 Sep 1;280(0):812–9.

16. Margolin A, Izumrudov V, Švedas VK, Zezin A, Kabanov V, Berezin I. Preparation and properties of penicillin amidase immobilized in polyelectrolyte complexes. Biochim Biophys Acta - Enzymol. 1981 Aug;660(2):359–65.

17. Sethuraman V a, Na K, Bae YH. pH-responsive sulfonamide/ PEI system for tumor specific gene delivery: an in vitro study. Biomacromolecules. 2006 Jan;7(1):64–70.

18. Deng R, Yue Y, Jin F, Chen Y, Kung H-F, Lin MCM, et al. Revisit the complexation of PEI and DNA - how to make low cytotoxic and highly efficient PEI gene transfection non-viral vectors with a controllable chain length and structure? J Control release. 2009 Nov 16 [cited 2011 Jul 12];140(1):40–6.

19. Bruil a, Oosterom H a, Steneker I, Al BJ, Beugeling T, van Aken WG, et al. Poly(ethyleneimine) modified filters for the removal of leukocytes from blood. J Biomed Mater Res. 1993 Oct;27(10):1253–68.

20. de Albuquerque TL, de Sousa M, Gomes e Silva NC, Girão Neto CAC, Gonçalves LRB, Fernandez-Lafuente R, et al. β-Galactosidase from Kluyveromyces lactis: Characterization, production, immobilization and applications - A review. Int J Biol Macromol. 2021;191(September):881–98.

21. Tello-Solís SR, Jiménez-Guzmân J, Sarabia-Leos C, Gómez-Ruíz L, Cruz-Guerrero AE, Rodríguez-Serrano GM, et al. Determination of the secondary structure of Kluyveromyces lactis β-galactosidase by circular dichroism and its structure-activity relationship as a function of the pH. J Agric Food Chem. 2005;53(26):10200–4.

22. Argenta AB, Nogueira A, de P. Scheer A. Hydrolysis of whey lactose: Kluyveromyces lactis β-galactosidase immobilisation and integrated process hydrolysis-ultrafiltration. Int Dairy J. 2021;117:105007.

23. Dickson RC, Dickson LR, Markin JS. Purification and properties of an inducible β-galactosidase isolated from the yeast Kluyveromyces lactis. J Bacteriol. 1979;137(1):51–61.

24. Martínez-Villaluenga C, Cardelle-Cobas A, Corzo N, Olano A, Villamiel M. Optimization of conditions for galactooligosaccharide synthesis during lactose hydrolysis by β-galactosidase from Kluyveromyces lactis (Lactozym 3000 L HP G). Food Chem. 2008 Mar [cited 2011 Aug 14];107(1):258–64.

25. Yin H, Bultema JB, Dijkhuizen L, van Leeuwen SS. Reaction kinetics and galactooligosaccharide product profiles of the β-galactosidases from Bacillus circulans, Kluyveromyces lactis and Aspergillus oryzae. Food Chem. 2017;225:230–8.

26. Pessela BCC, Fernández-lafuente R, Fuentes M, Vián A, Garc JL, Carrascosa A V, et al. Reversible immobilization of a thermophilic b-galactosidase via ionic adsorption on PEI-coated Sepabeads. Enzyme Microb Technol. 2003:32:369–74.

27. Cavaille D, Combes D. Characterization of β-galactosidase from Kluyveromyces lactis. Biotechnol Appl Biochem. 1995;22(1):55–64.

28. Patel AK, Singhania RR, Pandey A. 'Novel enzymatic processes applied to the food industry.' Curr Opin Food Sci. 2016;7:64-72.

29. Güleç HA. Immobilization of β-galactosidase from Kluyveromyces lactis onto polymeric membrane surfaces: effect of surface characteristics. Colloids Surf B Biointerfaces. 2013 Apr 1 [cited 2013 Aug 15];104:83–90.

30. Albayrak N, Yang ST. Immobilization of β-galactosidase on fibrous matrix by polyethyleneimine for production of galacto-oligosaccharides from lactose. Biotechnol Prog. 2002 [cited 2011 Dec 3];18(2):240–251.

31. de Lathouder KM, van Benthem DTJ, Wallin SA, Mateo C, Lafuente RF, Guisan JM, et al. Polyethyleneimine (PEI) functionalized ceramic monoliths as enzyme carriers: Preparation and performance. J Mol Catal B Enzym. 2008 Jan 2;50(1):20–7.

32. Albayrak N, Kanisli ME. Preparation and Characterization of Cross-Linked PEI-Lipase Aggregates with Improved Activity and Stability. JOTCSB. 2022;5(2):127–44.

33. Bayindirli A. Immobilization of enzymes and potential applications in food industry. Vol. 20, Gıda. 1995; 20;2:113-116.

34. Maghraby YR, El-Shabasy RM, Ibrahim AH, Azzazy HMES. Enzyme Immobilization Technologies and Industrial Applications. ACS Omega. 2023;8(6):5184–96.

35. Becerra M, Prado SD, Siso MIG, Cerdán ME. New secretory strategies for Kluyveromyces lactis β-galactosidase. Protein Eng. 2001;14(5):379–86.

36. Perczel AÁS, HollÓsi M, TusnÁdy GáÁB, Fasman GD. Convex constraint analysis: A natural deconvolution of circular dichroism curves of proteins. Protein Eng Des Sel. 1991;4(6):669–79.

37. Rodríguez ÁP, Leiro RF, Cristina MC, Cerdán ME, González Siso MI, Becerra M. Secretion and properties of a hybrid Kluyveromyces lactis-Aspergillus niger β-galactosidase. Microb Cell Fact. 2006;5:1–13.

38. Bayramoglu G, Kaya B, Yakup Arıca M. Immobilization of Candida rugosa lipase onto spacer-arm attached poly(GMA-HEMA-EGDMA) microspheres. Food Chem. 2005 Sep;92(2):261–8.

39. Pessela BCC, Betancor L, Lopez-Gallego F, Torres R, Dellamora-Ortiz GM, Alonso-Morales N, et al. Increasing the binding strength of proteins to PEI coated supports by immobilizing at high ionic strength. Enzyme Microb Technol. 2005 Aug [cited 2014 Dec 24];37(3):295–9.

40. Zhu J, Tang A, Law LP, Feng M, Ho KM, Lee DKL, et al. Amphiphilic core-shell nanoparticles with poly(ethylenimine) shells as potential gene delivery carriers. Bioconjug Chem. 2005;16(1):139–46.

41. Ghriga MA, Grassl B, Gareche M, Khodja M, Lebouachera SEI, Andreu N, et al. Review of recent advances in polyethylenimine crosslinked polymer gels used for conformance control applications. Polym Bull. 2019;76(11):6001–29.

42. Ortega N, Sáez L, Palacios D, Busto MD. Kinetic Modeling, Thermodynamic Approach and Molecular Dynamics Simulation of Thermal Inactivation of Lipases from Burkholderia cepacia and Rhizomucor miehei. Int J Mol Sci. 2022;23(12).

43. Bahar T, Çelebi S. Characterization of glucoamylase immobilized on magnetic poly(styrene) particles. Enzyme Microb Technol. 1998 Oct;23(5):301–4.

Noise Analysis For Active Element Based Capacitor Multipliers

Burak Sakaci[*] |Deniz Ozenli

National Defence University, Department of Electronics Engineering, Turkish Air Force Academy,34334, İstanbul, Türkiye.

Corresponding Author
Burak Sakaci
E-mail: buraksakaci@gmail.com **Phone:** +90 538 870 2414
RORID: https://ror.org/010t24d82

Cite As
Sakaci B, Ozenli D. Noise Analysis For Active Element Based Capacitor Multipliers. Hittite J Sci Eng. 2024;11(4):157-167.

Noise Analysis For Active Element Based Capacitor Multipliers

Burak Sakaci* | Deniz Ozenli

National Defence University, Department of Electronics Engineering, Turkish Air Force Academy,34334, İstanbul, Türkiye

Abstract

In this study, comprehensive noise analyses and optimization of two different capacitance multiplier structures have been presented. Capacitor multipliers, essential in low frequency applications due to capacitors' significant chip area requirement, play a significant role in high precision analog circuits. Noise impacts such filters by reducing the signal to noise ratio (SNR), increasing phase noise, and potentially causing distortion, which is critical in applications requiring high accuracy and stability, such as biomedical instrumentation, communication systems, and precision measurement devices. Therefore, thorough analysis and optimization of filter noise characteristics are essential for reliable operation in sensitive applications. Two capacitor multiplier structures are analyzed: the Multiple Output Voltage Differencing Transconductance Amplifier (MO-VDTA) based and the Multiple Output Current Differencing Transconductance Amplifier (MO-CDTA) based structures. The multiplication factor of the capacitor multiplier in basis of MO-VDTA varies between 120 and 750, depending on the I_B value.

This variation allows the cutoff frequency of the applied filter to change between 2 kHz and 12.4 kHz. The MO-CDTA based structure's multiplication factor varies between 400 and 1250 by changing the V_{GS} voltage of the external PMOS. This structure has been used in a 2nd order low pass filter, with the cutoff frequency varying between 23.6 kHz and 91 kHz in conjunction with multiplication factor changing. In this respect, comprehensive noise analyses of the filter applications of these two structures have been examined to ensure reliable and efficient operation in sensitive applications.

Keywords: Multiplication Factor, Capacitor Multiplier Multiple Output Voltage Differencing Transconductance Amplifier (MO-VDTA), Multiple Output Current Differencing Transconductance Amplifier (MO-CDTA), Noise Analysis

INTRODUCTION

Nowadays, modern analog circuit designs necessitate high capacitance values for a wide range of applications such as subhertz, speech, ultrasound, and biomedical fields. These applications demand substantial capacitance to function effectively specific frequency interval (1,2). Capacitor multipliers are used to achieve these high capacitance values at low production costs and in small chip areas (3,4). Capacitor multiplier structures can operate in two different modes: Current-mode and voltage-mode. In the current-mode capacitor multiplier equation, C_M represents the multiplied capacitance, C_B denotes the base capacitance, and "k" indicates the multiplication factor. This equation is expressed in the literature as $C_M = (1+k) \cdot C_B$ (5). Numerous active building blocks are employed to create efficient capacitor multiplier designs (1-18). Wearable technology, including smartwatches, wireless headphones, and biomedical devices, is a prominent market trend. Biomedical signals, with their low voltage levels, require filtering for human health compatibility (19,21). These filters often use large capacitors to achieve low frequency characteristics, as referred to (22). Ultrasound applications, such as food drying, distance measurement, and biomedical uses, are also drawing attention (23,25). Reference (26) also includes these operating frequency ranges. In this point of view, this study will discuss extended noise analyses of capacitor multiplier based filters suitable for these frequency ranges, with their role in signal processing depicted in Figure 1.
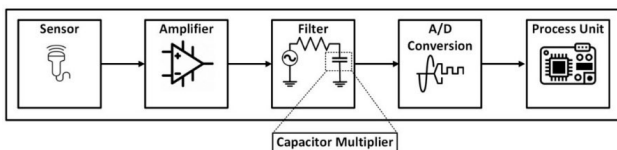

Figure 1 Capacitor multipliers in signal processing

Figure 1 highlights the crucial role of capacitors in filters. Noise analysis in filters is essential for optimizing performance and reliability by improving signal to noise ratios and reducing errors (27). Thanks to the noise analyses conducted on filters, component selection, design, and configurations are informed, enabling the design of filters that comply with standards, especially for biomedical and ultrasound applications (28).

This study presents extended noise analyses and optimizations for two filters using different active element blocks. The cutoff frequencies for 2nd order low pass filters with MO-VDTA and MO-CDTA structures are tunable from 2 kHz to 12.4 kHz and 23.6 kHz to 91 kHz, respectively, based on TSMC 0.18 μm CMOS technology. The study covers active element based capacitor multipliers, filter applications, noise optimization, and results using LT-Spice and Magic Layout Environment. Future work is also outlined.

MATERIAL AND METHODS

This section describes the capacitor multiplier structures used in this study. Capacitor multipliers have been implemented in the literature using various active elements. While some are realized with OTAs and current conveyors (29,30), others are implemented with different active elements. Some of them are valuable for high capacitance, variable capacitance, and low frequency operations, offering flexibility in filter design and optimization (12,31,32). In this study, MO-VDTA and MOCDTA based capacitor multipliers will be focused on this work, with all simulations performed with LT-Spice and Magic VLSI.

All simulation results in this study are based on layouts created using Magic VLSI. Figure 2 shows the MO-VDTA based capacitor multiplier structure, which occupies an area of 36.36 μm × 21.96 μm. Additionally, Figure 3 shows the MO-CDTA capacitor multiplier structure, which occupies an area of 176.76 μm × 136.71 μm.
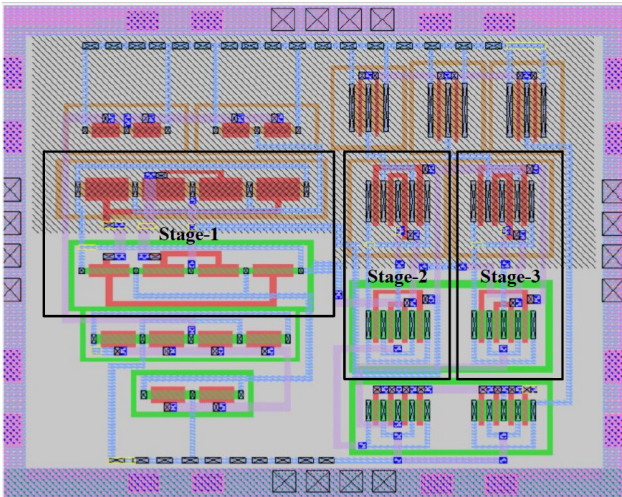
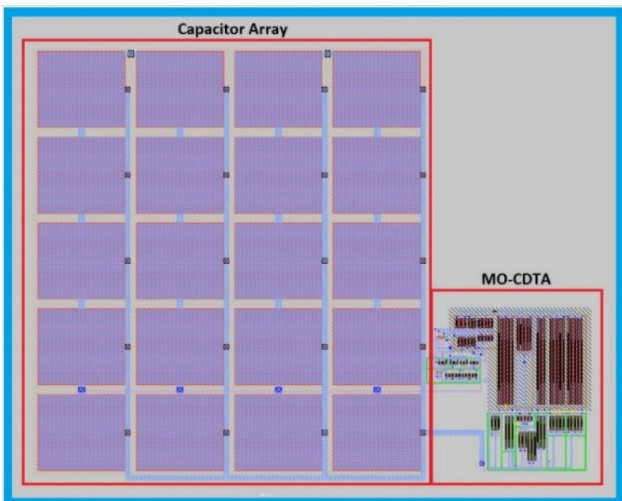**Figure 2** Layout of MO-VDTA Based Capacitance Multiplier

Figure 3 Layout of MO-CDTA Based Capacitance Multiplier

The VDTA structure, crucial for analog circuit design, traditionally includes two OTA stages (12,33,34). The MO-VDTA extends this with additional OTA stages, providing higher gain and suitability for current mode capacitive multipliers requiring large multiplication factors. The proposed MO-VDTA based multiplier has three OTA stages, seven terminals, and offers high impedance for easy interconnection, with V_P and V_N as differential inputs and V_Z as the output (35).

$$\begin{bmatrix} I_Z \\ I_{X1}+ \\ I_{X1}- \\ I_{X2}+ \\ I_{X2}- \end{bmatrix} = \begin{bmatrix} \gamma_1 G_{m1} & -\gamma_1 G_{m1} & 0 \\ 0 & 0 & \gamma_1 G_{m2} \\ 0 & 0 & -\gamma_2 G_{m2} \\ 0 & 0 & \gamma_3 G_{m3} \\ 0 & 0 & -\gamma_3 G_{m3} \end{bmatrix} \begin{bmatrix} V_P \\ V_N \\ V_Z \end{bmatrix} \quad (1)$$

Current mode capacitor multipliers utilize a feedback mechanism to scale base capacitance (7). Figure 4 illustrates a compact multiplier structure based on multioutput VDTA using X-terminal currents. Despite the rise in power consumption, silicon area, and design complexity, additional OTA stages can be added to enhance the "k" factor.
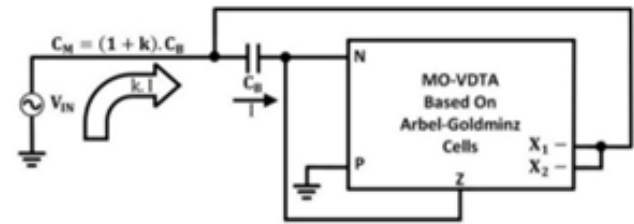

Figure 4 Capacitor multiplier based on MO-VDTA

Equations (2) and (3) describe the input impedance and multiplication factor of the proposed structure, while equation (5) provides the cut off frequency of a 1st order low pass filter. Tracking errors from the MO-VDTA's characteristic matrix, shown in equation (1), can be safely eliminated, so that γ coefficients are nearly 1 up to 10 MHz for the properly dimensioning in basis of TSMC 0.18μm technology. For low frequency applications up to 100 kHz, equations in (2) and (3) simplify the calculations for multiplication factor and cut off frequency as given in equations (4) and (5).

$$Z = \frac{sC_B + \gamma_1 G_{m1}}{sC_B\left(\gamma_1 G_{m1} + \gamma_2 G_{m2} + \gamma_3 G_{m3}\right)} \quad (2)$$

$$Z \cong \frac{G_{m1}}{sC_B\left(G_{m1} + G_{m2} + G_{m3}\right)} \quad (3)$$

$$k \cong \frac{G_{m1} + G_{m2} + G_{m3}}{G_{m1}} \quad (4)$$

$$\omega_{cut-off} \cong \frac{1}{kRC_B} \quad (5)$$

To attain a high multiplication factor, the first OTA stage's transconductance gain is kept lower than that of later stages, with the parameter "k" controlled by G_{M1}. Thus, transistors in the first OTA stage have smaller aspect ratios compared to those in the subsequent stages (6). For the first Arbel Goldminz cell, I_D in equation of (6) equals I_B /2, while in the second and third cells, it is approximately I_C/ 2. Figure 5 illustrates the OTA stages, where each transistor size is selected meticulously.
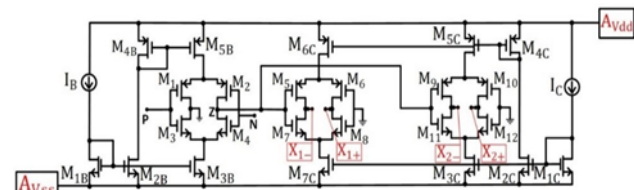

Figure 5 Transistor level of MO-VDTA

Table 1 MO-VDTA Transistors' dimensions

TRANSISTOR	Dimensions		TRANSISTOR	Dimensions	
	W	L		W	L
M_{1B}, M_{2B}, M_{3B}	0.6 µm	5 µm	M_1, M_2	1 µm	6 µm
M_{4B}, M_{5B}	1 µm	2 µm	M_3, M_4	0.3 µm	6 µm
M_{4C}	7 µm	0.18 µm	M_5, M_6, M_9, M_{10}	6 µm	0.36 µm
M_{5C}	8 µm	0.18 µm	M_{1C}, M_{2C}, M_{3C}, M_{7C}	3 µm	0.36 µm
M_{6C}	8 µm	0.18 µm	M_7, M_8, M_{11}, M_{12}	4 µm	0.36 µm

$$g_m = \sqrt{2\mu_n C_{OX} \frac{W}{L} I_D} \qquad (6)$$

The OTA cell gains are adjusted via bias currents I_B =25 nA and I_C =60 µA, resulting in the 1st OTA stage having a lower gain. The transconductance gains are G_{M1} = 250 nS and G_{M2} = G_{M3} = 110 µS.

The conventional Current Differencing Transconductance Amplifier (CDTA) is a key element in analog circuits (36,37). The MO-CDTA enhances the CDTA by adding extra output stages to the DO-OTA block, providing increased flexibility and suitability for high capacitance and current mode applications. The proposed MO-CDTA based capacitor multiplier uses three OTA stages to simplify the structure and reduce power consumption. The MO-CDTA's multiple outputs and amplified transconductance gain, as shown in equation (7), facilitate achieving a higher multiplication factor.

$$
\begin{bmatrix}
V_P \\ V_N \\ I_Z \\ I_{X1}+ \\ I_{X1}- \\ I_{X2}+ \\ I_{X2}- \\ I_{X3}+ \\ I_{X3}- \\ I_{X4}+ \\ I_{X4}-
\end{bmatrix}
=
\begin{bmatrix}
0 & 0 & 0 & 0 \\
0 & 0 & 0 & 0 \\
1 & -1 & 0 & 0 \\
0 & 0 & 0 & +G_{m1} \\
0 & 0 & 0 & -G_{m1} \\
0 & 0 & 0 & +G_{m2} \\
0 & 0 & 0 & -G_{m2} \\
0 & 0 & 0 & +G_{m3} \\
0 & 0 & 0 & -G_{m3} \\
0 & 0 & 0 & +G_{m4} \\
0 & 0 & 0 & -G_{m4}
\end{bmatrix}
\begin{bmatrix}
I_P \\ I_N \\ V_X \\ V_Z
\end{bmatrix}
\qquad (7)
$$

Equation (7) omits terminal parasitics for clarity. Figure 6 presents the transistor level implementation of the MO-CDTA, which is fully tunable via bias currents. Adding more output stages increases transconductance gain but also complexity and power consumption. The gain of each stage is defined by equation (8).

$$G_M \cong B\sqrt{\mu_n C_{OX} I_C \left(\frac{W}{L}\right)_{9,10}} \qquad (8)$$

In equation (8), B denotes the ratio of $\left(\frac{W}{L}\right)_{4C} / \left(\frac{W}{L}\right)_{5C}$ It is evident that the main factors affecting the gain are the bias current I_C and the W/L ratios of the relevant transistors. The

transistor size of MO-CDTA is selected with sensitivity. Table 2 representes transistor sizes of MO-CDTA.
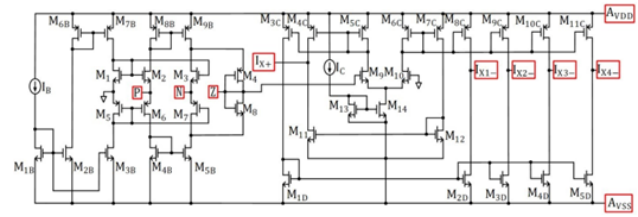

Figure 6 Transistor level of MO-CDTA

Table 2 MO-CDTA Transistors' dimensions

TRANSISTOR	Dimensions		TRANSISTOR	Dimensions	
	W	L		W	L
M_1B	1µm	0.36µm	M_{3C}, M_{4C}, M_{7C}, M_{8C} M_{9C}, M_{10C}, M_{11C}	54µm	0.36µm
M_{2B}, M_{3B}, M_4B, M_{5B}	2µm	0.36µm	M_{5C}, M_{6C}, M_{11}, M_{12}	20µm	0.36µm
M_{6B}	6µm	0.72µm	M_{13}	10µm	0.36µm
M_{7B}, M_{8B}, M_{9B}, M_5, M_6	6µm	0.36µm	M_{14}	18µm	0.36µm
M_1, M_2, M_3, M_8	1.5µm	0.36µm	M_{1D}, M_{2D}, M_{3D}, M_{4D}, M_{5D}	9µm	0.36µm
M_4, M_7, M_9, M_{10}	3µm	0.36µm			

The proposed design operates as a current mode capacitor multiplier, similar to the one described in the previous section. This is illustrated in Figure 7.
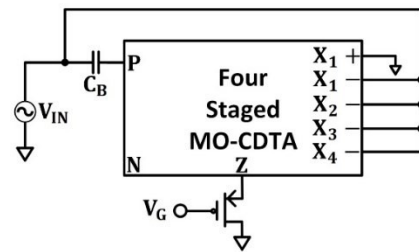
Figure 7 Capacitor multiplier based on MO-CDTA

The resistor value R_{MOS} in Figure 7 reflects the resistive properties of the PMOS transistor in the triode region, connected to the Z terminal of the multiplier

$$R_{MOS} \cong \frac{1}{k_P \frac{W}{L}(V_{SG} - |V_T|)} \qquad (9)$$

In this setup, the control voltage V_{GS} adjusts resistance, enabling electronic tuning of the capacitance multiplier as shown in Figure 7. Bias currents I_B and I_C ensure flexibility, while the output stages are crucial for achieving the desired multiplication factor. For ultrasonic applications, equation (10) can be simplified as equation (11), with the MO-CDTA's characteristic matrix and terminal parasitics as detailed.

$$Z \cong \frac{(R_{XP-})(1+sC_B R_P)}{sC_B((R_{XP-})+4R_P+4G_M(R_{MOS}//R_{ZP})(R_{XP-}))+4} \quad (10)$$

To simplify the impedance formula in the frequency range from 10 kHz to 1 MHz, terminal parasitics are neglected, resulting in the impedance formula as given in Equation 11.

$$Z \cong \frac{1}{sC_B+4sC_B G_m R_{MOS}} \quad (11)$$

Furthermore, the multiplication factor "k" for the proposed architecture is defined as shown in equation (12).

$$k \cong 1+4G_m R_{MOS} \quad (12)$$

Active element based capacitor multipliers, including MO-VDTA and MO-CDTA structures, offer significant benefits in filter design across various fields. In biomedical applications, they enable high precision filters for accurate signal processing. For speech processing, their adaptability enhances voice clarity and noise reduction. In ultrasound, they provide high frequency filters that improve signal handling and resolution. Following explains explores filter structures using MO-VDTA, applicable for low frequency usage in biomedical and speech filtering with roll off frequencies from several kHz to over 20 kHz. A 2nd order filter based on MO-VDTA is illustrated in Figure 8.
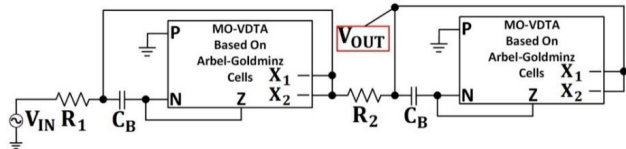

Figure 8 2nd order low pass filter based on MO-VDTA

The equations for the filter structure created with the MO-VDTA configuration are provided below, respectively:

$$\frac{V_{LP}}{V_{IN}} \cong \frac{1}{s^2 \frac{C_B^2 R_1 R_2 (G_{m1}+G_{m2}+G_{m3})^2}{G_{m1}^2}+s\frac{C_B(2R_1+R_2)(G_{m1}+G_{m2}+G_{m3})}{G_{m1}}+1} \quad (13)$$

$$\omega_0 \cong \sqrt{\frac{G_{m1}^2}{C_B^2 R_1 R_2 (G_{m1}+G_{m2}+G_{m3})^2}} \quad (14)$$

$$Q \cong \sqrt{\frac{R_1 R_2}{(2R_1+R_2)^2}} \quad (15)$$

$$S_{G_{m1}}^{\omega_0} \cong \frac{G_{m2}+G_{m3}}{G_{m1}+G_{m2}+G_{m3}}, S_{G_{m2}}^{\omega_0} \cong \frac{-G_{m2}}{G_{m1}+G_{m2}+G_{m3}}, S_{G_{m3}}^{\omega_0} \cong \frac{-G_{m3}}{G_{m1}+G_{m2}+G_{m3}}, S_{R_1,R_2}^{\omega_0} \cong -\frac{1}{2}, S_{C_B}^{\omega_0} \cong -1 \quad (16)$$

$$S_{R_1}^{Q} \cong -\frac{2R_1-R_2}{4R_1+2R_2}, S_{R_2}^{Q} \cong \frac{2R_1-R_2}{4R_1+2R_2} \quad (17)$$

When the multiplication factor ranges from 120 to 750, the cutoff frequency of the 2nd order filter varies between 2 kHz and 12.4 kHz, as shown in Figure 9. During this operation, the filter's power consumption is approximately 840 μW. For a 1st order filter, the cut off frequency ranges from 2.6 kHz to 15.8 kHz, making these frequency ranges suitable for the specific applications.
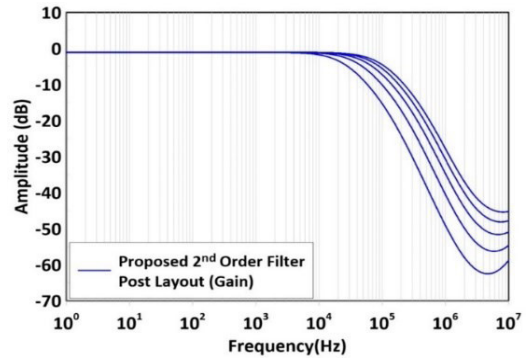

Figure 9 Gain response of 2nd order low pass filter based on MO-VDTA varying with different I_B (I_B= 25 nA to 250 nA, I_C = 60μA and R_{IN} = 50 kΩ).

To apply the proposed multiplier structure in ultrasound applications, both 1st order and 2nd order filters can be utilized. Figure 10 shows a 2nd order filter created with the MO-CDTA structure, which is electronically tunable and suitable for both low frequency and ultrasonic applications.
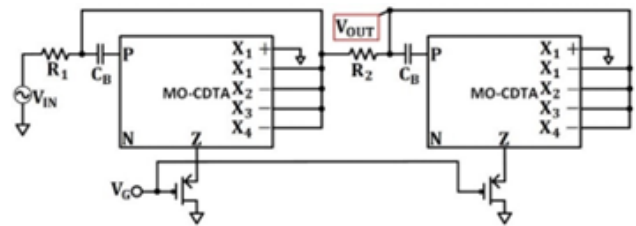
Figure 10 2nd order low pass filter based on MO-CDTA

For ultrasonic applications, filter structures are designed to operate between 20 kHz and 100 kHz with adequate suppression (22). The proposed capacitor multiplier circuit, with a multiplication factor from 400 to 1250, is integrated into a 2nd order filter as shown in Figure 10. By setting R_1= R_2=1 kΩ, the cut off frequency ranges from 23.6 kHz to 91 kHz, as illustrated in Figure 11, with V_{GS} varying from -0.5 V to -0.9 V in 0.1 V steps. The filter's power consumption is approximately 1.17 mW.
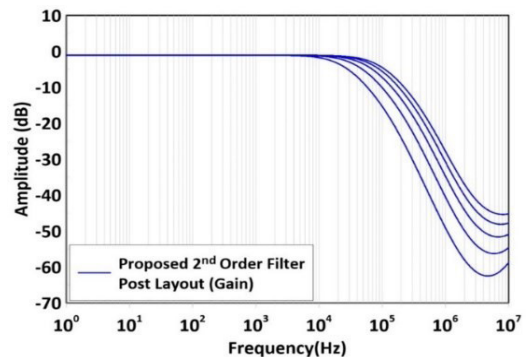
Figure 11 Gain response of 2nd order low pass filter based on MO-VDTA varying with different VGS (VGS= -0.5V to -0.9V).

Equations (18) and (19) provide the transfer functions for the low pass filters, including simplifications for parasitic effects.

The subsequent analysis describes the observed behavior of the 2nd order low pass filter. The behavior observed for the 1st and 2nd order low pass filter are as follows:

$$\frac{V_{OUT}}{V_{IN}} \cong \frac{R_{XP-}}{4R_1 + (R_{XP-}) + sC_B R_1 (R_{XP-})(1 + 4G_m(R_{MOS}//R_{ZP}))} \cong \frac{1}{1 + sC_B R_1 (1 + 4G_m R_{MOS})} \quad (18)$$

$$\frac{V_{OUT}}{V_{IN}} \cong \frac{1}{s^2 R_1 R_2 C_B^2 (1 + 4G_m R_{MOS})^2 + sC_B (R_1 + R_2)(1 + 4G_m R_{MOS}) + 1} \quad (19)$$

The cut off frequency and quality factor are calculated from equations (20), which are based on the transfer functions in equations (18) and (19). Furthermore, for the 2nd filter intended for ultrasound applications, sensitivity analyses for ω0 and Q are related to the dimensions of transistors and passive components, as outlined below:

$$\omega_0 \cong \sqrt{\frac{1}{C_B^2 R_1 R_2 (1 + 4G_m R_{MOS})^2}}, Q \cong \sqrt{\frac{R_1 R_2}{(2R_1 + R_2)^2}} \quad (20)$$

$$S_{C_B}^{\omega_0} \cong -1, \; S_{R_1, R_2}^{\omega_0} \cong -\frac{1}{2}, \; S_{G_m, R_{MOS}}^{\omega_0} \cong -\frac{4G_m R_{MOS}}{4G_m R_{MOS} + 1} \quad (21)$$

$$S_{R_1}^{Q} \cong -\frac{2R_1 - R_2}{4R_1 + 2R_2}, \; S_{R_2}^{Q} \cong \frac{2R_1 - R_2}{4R_1 + 2R_2} \quad (22)$$

RESULTS AND DISCUSSION

Noise analysis and optimization in the 2nd order low pass filters with capacitor multiplier structures are critical, particularly for biomedical and power ultrasound applications. Filters with cut off frequencies from 10 kHz to 100 kHz require careful optimization to mitigate active noise sources, such as flicker and thermal noise, which affect performance. Flicker noise is prominent at lower frequencies, while thermal noise increases at higher frequencies. Effective noise management involves optimizing transistor dimensions and passive components to improve the signal to noise ratio and meet performance standards. Essential mathematical equations for flicker and thermal noise analysis are detailed below (38-41).

$$\overline{i_n^2} = 4k\gamma T g_m \; [A^2/Hz] \rightarrow \text{Thermal Noise} \quad (23)$$

$$\overline{i_n^2} = \frac{KFI_D}{C_{OX} L^2} \frac{1}{f} \; [A^2/Hz] \rightarrow \text{Flicker (1/f) Noise} \quad (24)$$

To analyze noise in the MO-VDTA based filter, identify the key noise sources at each terminal using the characteristic matrix (1). Integrating these sources into the model is visualized, as shown in the Figure 12.

The transistor level MO-VDTA structure in Figure 5 influences the noise contributions at terminals as shown in Figure 12. Simplified equations, excluding some secondary transistor effects, lead to the equivalent noise at the 2nd order filter input, as given in Equation 25.
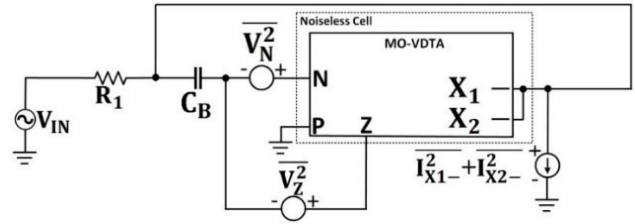

Figure 12 Noise sources of investigated filter

$$\overline{V_{IRN}^2} \cong 2\left(\overline{V_N^2} + \overline{V_P^2}\right) + R_1^2 (\overline{i_{X1-}^2} + \overline{i_{X2-}^2}) + R_2^2 (\overline{i_{X1-}^2} + \overline{i_{X2-}^2}) \quad (25)$$

For thorough noise analysis, individual contributions of noise sources in Equation 25 must be evaluated. The effects of noise at the N and Z nodes will be analyzed separately, while the grounded P node is excluded. Figure 13 shows the configuration with noise sources at the N and Z nodes.
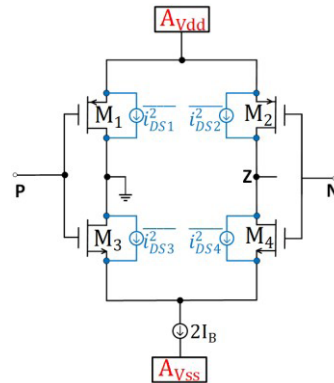
Figure 13 Noise sources of 1st stage

Referring to Figure 13, the noise equations dependent on voltage for the N and Z nodes are specified by Equation 26 and Equation 27, respectively.

$$\overline{V_N^2} \cong \frac{\overline{i_{DS1}^2} + \overline{i_{DS2}^2} + \overline{i_{DS3}^2} + \overline{i_{DS4}^2}}{g_{m1}^2} \quad (26)$$

$$\overline{V_Z^2} \cong \frac{\overline{i_{DS1}^2} + \overline{i_{DS2}^2} + \overline{i_{DS3}^2} + \overline{i_{DS4}^2}}{g_{m3}^2} \quad (27)$$

Figure 14 shows that noise from the second and third stages is mainly treated as current sources. Equations 28 and 29 are derived from this analysis.

$$\overline{i_{X1-}^2} \cong \overline{i_{DS5}^2} + \overline{i_{DS6}^2} + \overline{i_{DS7}^2} + \overline{i_{DS8}^2} \quad (28)$$

$$\overline{i_{X2-}^2} \cong \overline{i_{DS9}^2} + \overline{i_{DS10}^2} + \overline{i_{DS11}^2} + \overline{i_{DS12}^2} \quad (29)$$

Figure 14 Noise sources of 2st and 3rd stages

The "I" equations account for both flicker and thermal noise, as shown in Equations 23 and 24. Parasitic effects are excluded. Extending Equations 26 through 29 leads to Equation 30.

$$\overline{V_{IRN}^2} \cong \begin{bmatrix} 2\left(\dfrac{\overline{i_{DS1}^2}+\overline{i_{DS2}^2}+\overline{i_{DS3}^2}+\ove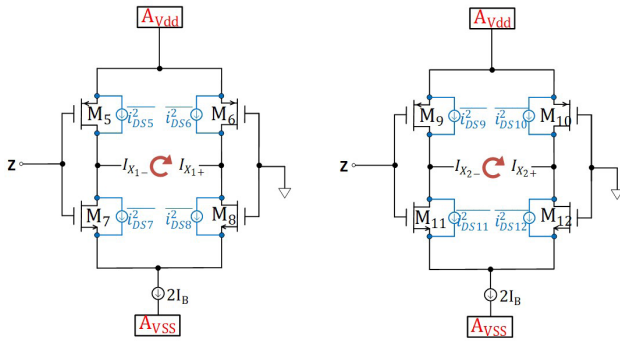rline{i_{DS4}^2}}{g_{m1}^2}+\dfrac{\overline{i_{DS1}^2}+\overline{i_{DS2}^2}+\overline{i_{DS3}^2}+\overline{i_{DS4}^2}}{g_{m3}^2}\right)+... \\ R_1^2\left(\overline{i_{DS5}^2}+\overline{i_{DS6}^2}+\overline{i_{DS7}^2}+\overline{i_{DS8}^2}+\overline{i_{DS9}^2}+\overline{i_{DS10}^2}+\overline{i_{DS11}^2}+\overline{i_{DS12}^2}\right)+... \\ R_2^2\left(\overline{i_{DS5}^2}+\overline{i_{DS6}^2}+\overline{i_{DS7}^2}+\overline{i_{DS8}^2}+\overline{i_{DS9}^2}+\overline{i_{DS10}^2}+\overline{i_{DS11}^2}+\overline{i_{DS12}^2}\right) \end{bmatrix} \quad (30)$$

Equation 30 indicates that multiple variables affect the equivalent noise at the input. Key factors determining the equivalent noise include the transconductance g_m of the second and third stages and the bias current I_C, with the bias current I_B of the first stage having a lesser impact due to its nA level. The noise contributions from I_C were tested at four levels, showing approximately 10% variation, as depicted in Figure 15. The analysis and optimization will focus on these parameters to enhance filter performance.
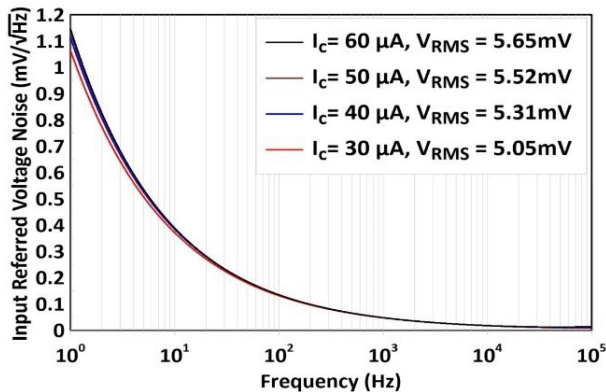

Figure 15 Input referred noise @ different I_C values

Following the analysis of I_C effects on noise, the focus shifts to gm. By halving the W/L ratio achieved by doubling the L value of transistors in the and third stages, g_m is reduced, lowering filter noise. Variations in gm and I_C are shown in the Figure 16 and Table 3
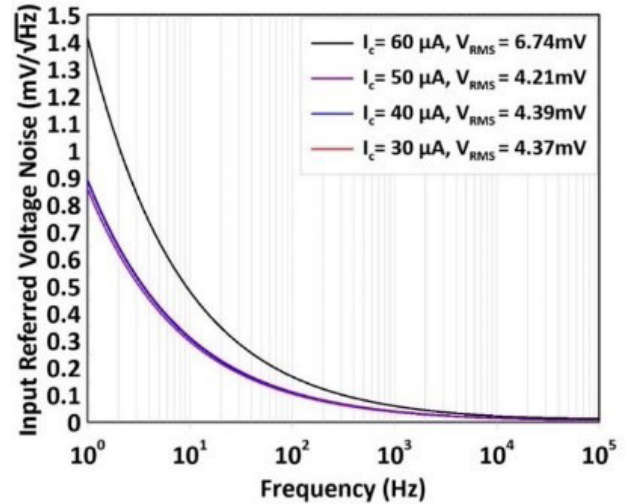

Figure 16 Input referred noise @ different I_C values with $g_m/2$

Table 3 displays the impact of g_m and I_C on noise. For NMOS transistors, g_m values are 376 µS and 105 µS; for PMOS, 220 µS and 139 µS. Variations in g_m and I_C significantly affect noise levels. However, decreased noise can worsen filter characteristics; at optimal settings, reducing noise by 40% results in a 20% change in cut off frequency. Depending on the application, trade-offs between noise reduction and filter performance must be considered, with potential exploration of alternative methods and variables for optimization.

To analyze noise for the MO-CDTA filter, dominant noise sources at each terminal, based on the characteristic matrix (7), must be identified and incorporated into the model. The block diagram showing these noise sources is illustrated in Figure 17.
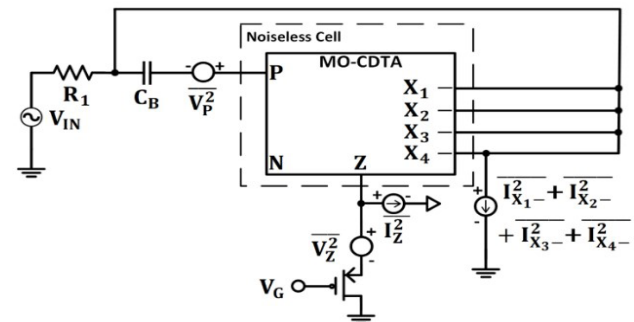
Figure 17 Noise sources of investigated filter

To determine the input referred voltage noise, derive the general equation for the equivalent input noise. Equations 31 and 32 provide the formulations for calculating this input referred voltage noise.

$$\overline{V_{IRN(1^{st})}^2} \cong \overline{V_P^2}+\overline{V_Z^2}+R_1^2\left(\overline{i_{X1-}^2}+\overline{i_{X2-}^2}+\overline{i_{X3-}^2}+\overline{i_{X4-}^2}+\overline{i_Z^2}\right) \quad (31)$$

$$\overline{V_{IRN(2^{nd})}^2} \cong 2\left[\overline{V_P^2}+\overline{V_Z^2}+R_1^2\left(\overline{i_{X1-}^2}+\overline{i_{X2-}^2}+\overline{i_{X3-}^2}+\overline{i_{X4-}^2}+\overline{i_Z^2}\right)\right] \quad (32)$$

To analyze the noise of the structure, assess the impact

Table 3 Effects of gm and I_c values on noise performance

g_m Values	$I_c(\mu A)$	Input Referred Voltage Noise	fCUT	dB Loss	g_m Values	$I_c(\mu A)$	Input Referred Voltage Noise	fCUT	dB Loss
g_m	60	10.13mV	2kHz	-2.6dB	$g_m/\sqrt{2}$	60	9.18mV	12.4kHz	-33dB
g_m	50	9.18mV	2.3kHz	-3dB	$g_m/\sqrt{2}$	50	6.39mV	7.2kHz	-16dB
g_m	40	7.67mV	5kHz	-8.2dB	$g_m/\sqrt{2}$	40	6.81mV	2.4kHz	-1dB
g_m	30	6.28mV	9.6kHz	-11dB	$g_m/\sqrt{2}$	30	6.19mV	3kHz	-1.2dB

of each transistor's noise on the input and output ports, as shown in Figure 17. The calculation, based on the transistors in Figure 18, evaluates the current impact on output terminals. For simplification, only significant transistors were included in the analysis, excluding others to manage complexity and focus on those with substantial effects.
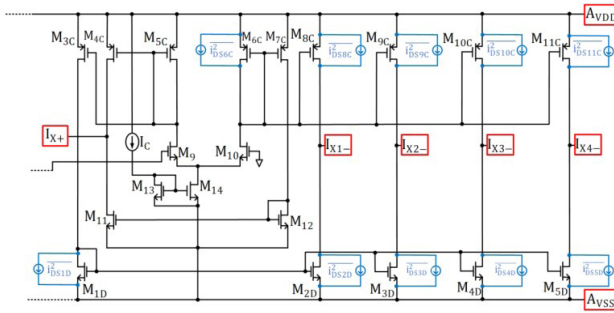

Figure 18 Noise sources of MO-CDTA

The noise impact on the output terminals is depicted by Equation 33, 34,35,37 and 37 as shown in Figure 18.

$$\overline{i^2_{OUT(OTA)}} \cong \overline{i^2_{DS5C}} + \overline{i^2_{DS6C}} + \overline{i^2_{DS9}} + \overline{i^2_{DS10}} \tag{33}$$

$$\overline{i^2_{X1-}} \cong \overline{i^2_{DS8C}} + \overline{i^2_{DS2D}} + \left(\frac{g_{m2D}}{g_{m1D}}\right)^2 \overline{i^2_{DS1D}} + \left(\frac{g_{m8C}}{g_{m6C}}\right)^2 \overline{i^2_{OUT(OTA)}} \tag{34}$$

$$\overline{i^2_{X2-}} \cong \overline{i^2_{DS9C}} + \overline{i^2_{DS3D}} + \left(\frac{g_{m3D}}{g_{m1D}}\right)^2 \overline{i^2_{DS1D}} + \left(\frac{g_{m9C}}{g_{m6C}}\right)^2 \overline{i^2_{OUT(OTA)}} \tag{35}$$

$$\overline{i^2_{X3-}} \cong \overline{i^2_{DS10C}} + \overline{i^2_{DS4D}} + \left(\frac{g_{m4D}}{g_{m1D}}\right)^2 \overline{i^2_{DS1D}} + \left(\frac{g_{m10C}}{g_{m6C}}\right)^2 \overline{i^2_{OUT(OTA)}} \tag{36}$$

$$\overline{i^2_{X4-}} \cong \overline{i^2_{DS11C}} + \overline{i^2_{DS5D}} + \left(\frac{g_{m5D}}{g_{m1D}}\right)^2 \overline{i^2_{DS1D}} + \left(\frac{g_{m11C}}{g_{m6C}}\right)^2 \overline{i^2_{OUT(OTA)}} \tag{37}$$

Figure 19.a illustrates the transistors affecting noise at the P terminal, with the equivalent noise given by Equation 38. For the Z terminal, Figure 19.b and MOSFET noise equations

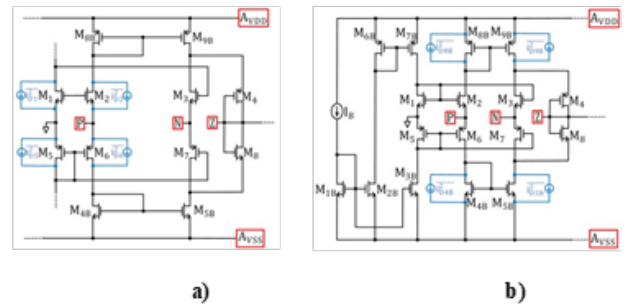(23,24) lead to the derivation of Equations 39 and 40, which describe the associated noise contributions.

Figure 19 Noise sources visualization for input referred noise effects' calculations at a) P terminal b) P and Z Terminals

$$\overline{V^2_P} \cong \frac{\overline{i^2_{D1}} + \overline{i^2_{D2}} + \overline{i^2_{D5}} + \overline{i^2_{D6}}}{g^2_{m1}} \tag{38}$$

$$\overline{i^2_Z} \cong \overline{i^2_{DS5B}} + \overline{i^2_{DS9B}} + \left(\frac{g_{m5B}}{g_{m4B}}\right)^2 \overline{i^2_{DS4B}} + \left(\frac{g_{m9B}}{g_{m8B}}\right)^2 \overline{i^2_{DS8B}} \tag{39}$$

$$\overline{V^2_Z} \cong 4kT\gamma R_{MOS} + \frac{KF}{2C_{OX}WLK'}\frac{1}{f} \tag{40}$$

Substituting the equations from Equation 32 yields the equivalent input referred voltage noise for the 2nd order low pass filter.

$$\overline{V^2_{IRN(2^{nd})}} \cong 2 \begin{bmatrix} \frac{\overline{i^2_{D1}} + \overline{i^2_{D2}} + \overline{i^2_{D5}} + \overline{i^2_{D6}}}{g^2_{m1}} + \cdots \\ \left(4kT\gamma R_{MOS} + \frac{KF}{2C_{OX}WLK'}\frac{1}{f}\right) + \cdots \\ 4R^2_1\left(\overline{i^2_{DS8C}} + \overline{i^2_{DS2D}} + \left(\frac{g_{m2D}}{g_{m1D}}\right)^2\overline{i^2_{DS1D}} + \left(\frac{g_{m8C}}{g_{m6C}}\right)^2\left(\overline{i^2_{DS5C}} + \overline{i^2_{DS6C}} + \overline{i^2_{DS9}} + \overline{i^2_{DS10}}\right)\right) + \cdots \\ R^2_1\left(\overline{i^2_{DS5B}} + \overline{i^2_{DS9B}} + \left(\frac{g_{m5B}}{g_{m4B}}\right)^2\overline{i^2_{DS4B}} + \left(\frac{g_{m9B}}{g_{m8B}}\right)^2\overline{i^2_{DS8B}}\right) \end{bmatrix} \tag{41}$$

Equation 41 shows that some filter parameters inversely affect noise, while others increase it. Table 4 presents how input referred voltage noise varies with these parameters. It's

Table 4 Noise analysis of the applied filter for various parameters

Parameters	Input Referred Voltage Noise	fCUT	dB Loss	Parameters	Input Referred Voltage Noise	fCUT	dB Loss
RMOS	19.98mV	29.3 kHz	-1 dB	$\dfrac{RMOS}{\sqrt{2}}$	14.15mV	41.1 kHz	-1 dB
$g_{m1,2}$	19.98mV	29.3 kHz	-1 dB	$\dfrac{gm1,2}{\sqrt{2}}$	20.37mV	30 kHz	-1 dB
$g_{m5C,6C}$	19.98mV	29.3 kHz	-1 dB	$\dfrac{gm5C,6C}{\sqrt{2}}$	39.75mV	16.4 kHz	-1.6 dB
$g_{m1D,2D}$	19.98mV	29.3 kHz	-1 dB	$\dfrac{gm1D,2D}{\sqrt{2}}$	26.49mV	22.8 kHz	-1.2 dB
$g_{m9,10}$	19.98mV	29.3 kHz	-1 dB	$\dfrac{gm9,10}{\sqrt{2}}$	16.17mV	35.9 kHz	-1 dB

*The gm values were altered by changing the channel lengths (L) of the transistors.

also crucial to maintain the filter's characteristic properties during these variations.

The table confirms the equivalent input referred voltage noise for the 2nd order low pass filter, showing that changes in parameter values affect noise levels. Table 4 indicates that reducing noise by 19% can shift the cut-off frequency by 22% at the optimal configuration (gm9,10). Depending on application needs, one can select the best configuration or explore alternatives by adjusting other parameters

CONCLUSION

In this study explores noise analysis and optimization for filters using two active element based capacitor multiplier structures: MO-VDTA and MO-CDTA. Both structures offer an adjustable multiplication factor "k", allowing operation across various cutoff frequencies for different applications. The MO-VDTA structure provides a multiplication factor ranging from 120 to 750, with a filter cutoff frequency from 2 kHz to 12.4 kHz. Initial input referred noise is 10.13 mV, reduced to 6.19 mV (40% decrease) through optimization, even though this causes a 20% variation in cutoff frequency. For the MO-CDTA structure, the multiplication factor also ranges from 120 to 750, with cutoff frequencies between 400 Hz and 1250 Hz. Initial input referred noise is 19.98 mV, reduced to 16.17 mV (19% decrease), resulting in a 22% change in cutoff frequency. In the noise analyses of filters, additional parasitic effects of the active elements were not included in the calculations to facilitate easier interpretation of the equations. Additionally, only the transistors with dominant noise contributions were considered. The findings highlight the need for noise optimization in low frequency applications and provide mathematical expressions for factors affecting noise. The results demonstrate that while reducing noise can decrease the cut off frequency, the   trade-offs between noise and cut off frequency vary with application. Future research will investigate additional noise parameters for the further performance optimization.

References
1. Kumar A, Singh D, Nand D. A Novel CFDITA-Based Design of Grounded Capacitance Multiplier and Its Transpose Structure. Circuits Syst Signal Process. Birkhauser; 2022;41(10):5319–39. DOI: 10.1007/S00034-022-02032-4/METRICS
2. Tang Y, Ismail M, Bibyk S. Adaptive miller capacitor multiplier for compact on-chip PLL filter. Electron Lett. 2003;39(1):43–5. DOI: 10.1049/EL:20030086
3. Sotner R, Jerabek J, Polak L, Petrzela J. Capacitance Multiplier Using Small Values of Multiplication Factors for Adjustability Extension and Parasitic Resistance Cancellation Technique. IEEE Access. Institute of Electrical and Electronics Engineers Inc.; 2020;8:144382–92. DOI: 10.1109/ACCESS.2020.3014388
4. Shukla P, Gupta A. Current-Mode PMOS capacitance multiplier. Proceedings of the International Conference on Inventive Systems and Control, ICISC 2017. Institute of Electrical and Electronics Engineers Inc.; 2017; DOI: 10.1109/ICISC.2017.8068658
5. Padilla-Cantoya I. Low-power high parallel load resistance current-mode grounded and floating capacitor multiplier. IEEE Transactions on Circuits and Systems II: Express Briefs. Institute of Electrical and Electronics Engineers Inc.; 2013;60(1):16–20. DOI: 10.1109/TCSII.2012.2234923
6. Stornelli V, Safari L, Barile G, Ferri G. A New Extremely Low Power Temperature Insensitive Electronically Tunable VCII-Based Grounded Capacitance Multiplier. IEEE Transactions on Circuits and Systems II: Express Briefs. Institute of Electrical and Electronics Engineers Inc.; 2021;68(1):72–6. DOI: 10.1109/TCSII.2020.3005524
7. Padilla-Cantoya I. Capacitor multiplier with wide dynamic

range and large multiplication factor for filter applications. IEEE Transactions on Circuits and Systems II: Express Briefs. Institute of Electrical and Electronics Engineers Inc.; 2013;60(3):152–6. DOI: 10.1109/TCSII.2013.2240814

8. Al-Absi MA, Abulema'atti MT. A Tunable Floating Impedance Multiplier. Arab J Sci Eng. Springer Verlag; 2019;44(8):7085–9. DOI: 10.1007/S13369-019-03792-Z/METRICS

9. Yesil A, Yuce E, Minaei S. Grounded capacitance multipliers based on active elements. AEU - International Journal of Electronics and Communications. Urban & Fischer; 2017;79:243–9. DOI: 10.1016/J.AEUE.2017.06.006

10. Yucehan T, Yuce E. A New Grounded Capacitance Multiplier Using a Single ICFOA and a Grounded Capacitor. IEEE Transactions on Circuits and Systems II: Express Briefs. Institute of Electrical and Electronics Engineers Inc.; 2022;69(3):729–33. DOI: 10.1109/TCSII.2021.3102118

11. Ozenli D, Alaybeyoglu E. An electronically tunable CMOS implementation of capacitance multiplier employing CCCDTA. AEU - International Journal of Electronics and Communications. Urban & Fischer; 2022;155:154359. DOI: 10.1016/J.AEUE.2022.154359

12. Sakacı B, Özenli D. A current mode capacitance multiplier employing a single active element based on Arbel-Goldminz cells for low frequency applications. Microelectron Eng. Elsevier; 2024;288:112157. DOI: 10.1016/J.MEE.2024.112157

13. Özer E. Electronically tunable CFTA based positive and negative grounded capacitance multipliers. AEU - International Journal of Electronics and Communications. Urban & Fischer; 2021;134:153685. DOI: 10.1016/J.AEUE.2021.153685

14. Ozenli D, Alaybeyoglu E, Kuntman H. A tunable lossy grounded capacitance multiplier circuit based on VDTA for the low frequency operations. Analog Integr Circuits Signal Process. Springer; 2022;113(2):163–70. DOI: 10.1007/S10470-022-02077-0/METRICS

15. Dogan M, Yuce E. A new CFOA based grounded capacitance multiplier. AEU - International Journal of Electronics and Communications. Urban & Fischer; 2020;115:153034. DOI: 10.1016/J.AEUE.2019.153034

16. Ferri G, Safari L, Barile G, Scarsella M, Stornelli V. New Resistor-Less Electronically Controllable ±C Simulator Employing VCII, DVCC, and a Grounded Capacitor. Electronics 2022, Vol 11, Page 286. Multidisciplinary Digital Publishing Institute; 2022;11(2):286. DOI: 10.3390/ELECTRONICS11020286

17. Padilla-Cantoya I, Gurrola-Navarro MA, Bonilla-Barragan CA, Molinar-Solis JE, RizoDominguez L, Medina-Vazquez AS. Impedance-mode capacitance multiplier with OTAbased flipped voltage follower for high accuracy and large multiplication factor. IEICE Electronics Express. The Institute of Electronics, Information and Communication Engineers; 2022;19(19):20220208–20220208. DOI: 10.1587/ELEX.19.20220208

18. Paul T, Roy S, Pal R. Lossy & Lossless Capacitance Multipliers: A Series of Realization Using VDTAs & Single Grounded Capacitor. Mapana Journal of Sciences. 2022;21:1-34. doi:10.12723/mjs.62.0.

19. Seneviratne S, Hu Y, Nguyen T, Lan G, Khalifa S, Thilakarathna K, et al. A Survey of Wearable Devices and Challenges. IEEE Communications Surveys and Tutorials. Institute of Electrical and Electronics Engineers Inc.; 2017;19(4):2573–620. DOI: 10.1109/COMST.2017.2731979

20. Rajan VS, Kishore KH, Sanjay R, Kumaravel S, Venkataramani B. A novel programmable attenuator based low Gm-OTA

21. Haghi M, Thurow K, Stoll R. Wearable Devices in Medical Internet of Things: Scientific Research and Commercially Available Devices. Healthc Inform Res. Korean Society of Medical Informatics; 2017;23(1):4–15. DOI: 10.4258/HIR.2017.23.1.4

22. Cardoso J. The Biomedical Engineering Handbook Third Edition Biomedical Engineering Fundamentals.

23. Huang D, Men K, Li D, Wen T, Gong Z, Sunden B, et al. Application of ultrasound technology in the drying of food products. Ultrason Sonochem. Elsevier; 2020;63:104950. DOI: 10.1016/J.ULTSONCH.2019.104950

24. Bühling B, Maack S, Strangfeld C. Fluidic Ultrasound Generation for Non-Destructive Testing. Advanced Materials. John Wiley and Sons Inc; 2024;36(18). DOI: 10.1002/ADMA.202311724

25. Moisello E, Novaresi L, Sarkar E, Malcovati P, Costa TL, Bonizzoni E. PMUT and CMUT Devices for Biomedical Applications: A Review. IEEE Access. Institute of Electrical and Electronics Engineers Inc.; 2024;12:18640–57. DOI: 10.1109/ACCESS.2024.3359906

26. Cheng X, Zhang M, Xu B, Adhikari B, Sun J. The principles of ultrasound and its application in freezing related processes of food materials: A review. Ultrason Sonochem. Elsevier; 2015;27:576–85. DOI: 10.1016/J.ULTSONCH.2015.04.015

27. Magsi H, Sodhro AH, Chachar FA, Abro SAK. Analysis of signal noise reduction by using filters. 2018 International Conference on Computing, Mathematics and Engineering Technologies: Invent, Innovate and Integrate for Socioeconomic Development, iCoMET 2018 - Proceedings. Institute of Electrical and Electronics Engineers Inc.; 2018;2018January:1–6. DOI: 10.1109/ICOMET.2018.8346412

28. Kim D, Goldstein B, Tang W, Sigworth FJ, Culurciello E. Noise analysis and performance comparison of low current measurement systems for biomedical applications. IEEE Trans Biomed Circuits Syst. 2013;7(1):52–62. DOI: 10.1109/TBCAS.2012.2192273

29. Alaybeyoğlu, E. A New Implementation of Capacitor Multiplier with Cell-Based Variable Transconductance Amplifier. IET Circuits, Devices & Systems. (2019); DOI: 13. 10.1049/iet-cds.2018.5217.

30. Khan AA, Bimal S, Dey KK, Roy SS. Current conveyor based R- and C- multiplier circuits. AEU - International Journal of Electronics and Communications. Urban & Fischer; 2002;56(5):312–6. DOI: 10.1078/1434-8411-54100121

31. Sakaci B, Ozenli D. An Electronically Tunable Capacitance Multiplier Structure Using DTMOS Technique for the Low Frequency Applications. International Conference on Electrical, Computer and Energy Technologies, ICECET 2023. Institute of Electrical and Electronics Engineers Inc.; 2023; DOI: 10.1109/ICECET58911.2023.10389302

32. Aghaei Jeshvaghani M, Dolatshahi M. A new ultra-low power wide tunable capacitance multiplier circuit in subthreshold region for biomedical applications. AEU - International Journal of Electronics and Communications. Urban & Fischer; 2024;177:155166. DOI: 10.1016/J.AEUE.2024.155166

33. Satansup J, Tangsrirat W. Compact VDTA-based current-mode electronically tunable universal filters using grounded capacitors. Microelectronics J. Elsevier; 2014;45(6):613–8. DOI: 10.1016/J.MEJO.2014.04.008

34. Alaybeyoğlu E, Kuntman H. CMOS implementations of VDTA based frequency agile filters for encrypted communications. Analog Integr Circuits Signal Process. Springer New York LLC;

for biomedical applications. Microelectronics J. Elsevier; 2020;97:104721. DOI: 10.1016/J.MEJO.2020.104721

2016;89(3):675–84. DOI: 10.1007/S10470-016-0760-Y/METRICS

35. Arbel AF, Goldminz L. Output stage for current-mode feedback amplifiers, theory and applications. Analog Integr Circuits Signal Process. Kluwer Academic Publishers; 1992;2(3):243–55. DOI: 10.1007/BF00276637/METRICS

36. Bisariya S, Afzal N. Design and implementation of CDTA: a review. Sadhana - Academy Proceedings in Engineering Sciences. Springer; 2020;45(1). DOI: 10.1007/S12046-02001511-1

37. Sakaci B, Ozenli D, Kuntman HH. An Electronically Tunable Capacitance Multiplier Employing Single Active Block For The Speech Processing Applications. 14th International Conference on Electrical and Electronics Engineering, ELECO 2023 - Proceedings. Institute of Electrical and Electronics Engineers Inc.; 2023; DOI: 10.1109/ELECO60389.2023.10416079

38. Razavi Behzad. RF microelectronics. Prentice Hall PTR; 20081998;335.

39. Horowitz P, Hill W. Art of Electronics, The. Camb.U.P.; 2011; Available from: https://books.google.com/books/about/The_Art_of_Electronics.html?hl=tr&id=LAiWPwA ACAAJ

40. Buckingham MJ. Noise in electronic devices and systems. E. Horwood ; Halsted Press; 1983;372.

41. Allen PE., Holberg DR. CMOS analog circuit design. Oxford University Press; 1987;701.

Evaluating the Combined Effects of Transverse Pitch Ratio and Flow Arrangement on the Thermo-Hydraulic Performance of a Novel Inclined Delta Winglet

Hüseyin Zahit Demirağ ⓘ

Yozgat Bozok University, Department of Mechanical Engineering, 66200, Yozgat, Türkiye.

Corresponding Author

Hüseyin Zahit Demirağ
E-mail: zahit.demirag@bozok.edu.tr Phone: +90354 242 1001
RORID: https://ror.org/04qvdf239

Cite As

Demirağ H, Z. Evaluating the Combined Effects of Transverse Pitch Ratio and Flow Arrangement on the Thermo-Hydraulic Performance of a Novel Inclined Delta Winglet. Hittite J Sci Eng. 2024;11(4):169-180.

Evaluating the Combined Effects of Transverse Pitch Ratio and Flow Arrangement on the Thermo-Hydraulic Performance of a Novel Inclined Delta Winglet

Hüseyin Zahit Demirağ

Yozgat Bozok University, Department of Mechanical Engineering, 66200, Yozgat, Türkiye.

Abstract

In this work, the in-depth examinations of the Novel Inclined Delta Winglet (NIDW) in terms of heat transfer performance and the flow characteristics are conducted at Re=5000-17500, utilizing (SST) k-ω turbulence model. In accordance with the objective of this investigation, the combined effects of the positioning of the NIDW in common-flow-down (NIDW-CFlowD) and common-flow-up (NIDW-CFlowU) orientations together with two transverse pitch ratios [P_t=0.333 and 0.166] are investigated and the resulting data are presented in a comparative manner. The angle of attack [α=30°] and the angle of inclination [β=30°] of the NIDW are kept constant. The numerical results indicate that the NIDW-CFlowD orientation at P_t=0.333 has more pronounced effect in terms of thermal performance, with an approximate increase of 4.29% increase in the Nusselt number at Re=17500, whereas the opposite trend is observed at P_t=0.166, yielding a smaller rise of around 3.13% in Nusselt number at Re=17500. The reversal in trend is entirely due to the positioning of the NIDW in the CFlowD orientation, which causes the vortex rotation centers to move further apart in the main flow direction, resulting in 4.36% and 4.02% higher Darcy friction factors in cases of P_t=0.333 and P_t=0.166, respectively compared to CFlowU configuration at Re=5000. Therefore, the highest and lowest ranges of Thermal Enhancement Factor (TEF) are calculated to be between 1.325-1.215 and 1.221-1.122 for the cases of NIDW-CFlowU with P_t=0.166 and NIDW-CFlowU with P_t=0.333 respectively. This corresponds to an increase in TEF of around 8.52% and 8.30% increase in TEF at Re=5000 and 17000, respectively.

Keywords: Novel inclined delta winglet, common-flow-up/down orientations, turbulent flow, transverse pitch ratio, thermo-hydraulic performance

INTRODUCTION

Solar Air Heater (SAH) is a one of the widely utilized [1][2][3] a type of heat exchanger that is particularly suited to low-temperature applications. They are preferred due to a number of factors, including their low capital and operating costs, simple configuration, ease of maintenance, being eco-friendly [4] and etc. A SAH is designed with the objective of maximizing the transfer of absorbed solar energy to the moving air [5], and thus ensuring the highest possible level of convective heat transfer between the absorber plate and the air. However, given the fact that the air's convective heat transfer coefficient is relatively poor [6][7], leading to the resistance to heat flow at considerable level [8][9][10]. To overcome this phenomenon, one of the most effective methods is to place a Vortex Generator (VG) heated surface of heat exchangers where the heat transfer takes place [11][12]. In this regard, two of the primary parameters, investigated in the method of enhancing convective heat transfer through the utilization of VG, encompass the positioning of the VG in different flow orientations including common-flow-up/down and the transverse pitch ratios.

In a configuration in which the distance between the leading edges of vortex generators in a plane perpendicular to the main flow is either greater or smaller than that between the trailing edges, the resulting flow structures are referred to as common-flow-up and common-flow-down, respectively. Despite the lack of explicit preference for either flow pattern in the existing literature with regard to thermal performance, the vortex interactions with the boundary layer exhibit notable differences between common-flow-up and common-flow-down orientations.

Accordingly, in order to investigate the impacts of flow patterns on thermal performance, Ke et al. [13] carried out numerical analysis to investigate the effect of delta winglet vortex generators on heat transfer and Darcy friction factor in a rectangular channel. Based on their numerical resulting data, they concluded that the common-flow-up configuration showed improved effectiveness when the delta winglet aspect ratio was relatively low, while the common-flow-down layout showed superior performance when the aspect ratio was high. Kim and Yang [14] performed detailed experimental investigation in order to study the flow characteristics and heat transfer performance of counter-rotating vortices. The boundary layer interaction becomes stronger than the vortex interaction as the longitudinal vortex pair in the common-flow-down moves downstream. However, the vortex interaction is stronger than the boundary layer interaction in the case of the longitudinal vortex pair in the common-flow-up flow pattern. Therefore, they emphasized that the common-flow-down configurations have better heat transfer characteristics than the cases with the common-flow-up orientation. Tian et al. [15] conducted a numerical study with the aim of comparing the thermal performance of DWP and RWP positioned on the bottom surface of the duct in common-flow-up/down configurations under a fixed angle of attack of β = 45°. They stated that DWP-inserted channel showed a comparable overall performance for common-flow-down and common-flow-up configurations, whereas, in the case of RWP-inserted channel, common-flow-down orientation offer superior overall performance compared to the common-flow-up flow pattern. In a numerical study, Salleh et al. [16] emphasized that VGs generate a high momentum rotating flow in the 'wake region', defined as the low pressure region under the common-flow-down configuration. On the other hand, they stated that VGs act like a nozzle under the common-flow-up orientation, increasing the flow velocity and delaying the flow separation behind the pipe, and improvements are obtained in these regions where heat transfer is low. In their research, Fu et al. [17] investigated the impact of common-flow-up/down flow configurations, as well as their arrangement either at the

same or opposite channel walls, in terms of the heat transfer and friction factor characteristics of a minichannel within the Reynolds number range of 3000-18000. The researchers observed that in the common-flow-up-1 configuration, the two vortices formed behind the LVGs, occupy the majority of the channel, resulting in a uniform distribution of velocity and that the vortex-occupied areas exhibit higher velocity. In contrast, the primary vortex in the common-flow-down-1 configuration occupies a larger area. However, the core of the channel exhibits enhanced velocity and a thinner thermal boundary layer in the vicinity of the bottom wall.

Another parameter investigated to increase the TEF is the ratio of the transverse spacing between the VGs to channel width, which is generally denoted as the transverse pitch ratio $[P_t]$ when VGs are positioned along the channel width. In particular, in the case of insufficient transverse spacing between VGs, negative interaction between the velocity components of the vortices in the plane perpendicular to the flow direction causes the turbulence intensity to decrease and Darcy friction factor to be elevated as well. It is therefore of great importance to determine the optimum values of all these dimensionless parameters in order to achieve the highest possible level of convection heat transfer by increasing the turbulence intensity throughout the test region, while achieving the lowest possible pressure drop.

Within this framework, Song et al. [18] carried out computational assessment, focusing on the significance of the transverse pitch ratio with respect to pressure drop characteristics and heat transfer performance. They emphasized that the interaction between longitudinal vortices leads to a reduction in vortex intensity with a higher pressure drop along test region. They concluded that the increases in vortex intensity and Nusselt number of up to 21.4% and 29.2%, respectively, at optimum pitch. Tanaka et al. [19] carried out both numerical and experimental assessment with an objective of determining optimum parameters within the range of Re=360-3600. Their results suggest that an optimum transverse pitch, S_t, is attained at S_t/H_d=3 (or greater), which effectively prevents the interaction of vortices by adjacent rectangular winglets. Dogan and Erzincan [20] also highlighted the fact that one of the key parameters in terms of thermal performance is the transverse pitch ratio, and the optimum transverse pitch ratio for attaining the highest TEF is determined to be R_T = 0.16. Skullong and Promvonge [21] also examined the influence of two transverse pitches of R_p = 1 and 2 on heat transfer and friction factor characteristics, spanning the range of Re=5000-24000. They determined that the greatest value of TEF is achieved through the incorporation of DWs at R_p = 1. Hu et al. [22] carried out experimental study regarding the impact of one-eighth sphere vortex generators (OES-VGs) on heat transfer and friction factor performance in the range of Re=4000-19000. They pointed out that a reduction in the S/H ratio allows for the installation of a greater number of OES-VGs on the

absorber within the same duct length, resulting in an increase in fluid disturbances, which amplifies the turbulence of the air surrounding the absorber plate, thereby enhancing the convective transfer of heat. Furthermore, Demirağ H.Z. [23] also pointed out that a reduction in the transverse pitch ratio, resulting in an increased number of NIDWs in a single row, is the main factor contributing to the elevated Nusselt number (or Nu/Nu_0 ratio). This is due to the fact that the doubling of the NIDWs, which leads to the formation of twice as many longitudinal vortices within the fluid domain test region, consequently amplifies the impact on the heated surface.

A review of existing literature reveals that studies have been predominantly examined the effects of transverse pitch ratio and the impacts of CFlowU or CFlowD flow patterns on thermal performance independently. To the best of our knowledge, no previous studies have explored the combined impacts of these two variables, despite the presence of significant distinctions in longitudinal vortex interactions and vortex center spacing in the cases of CFlowU and CFlowD flow patterns, which have a substantial potential to affect thermo-hydraulic performance. Accordingly, this study provides a unique analysis distinct from previous research [23] by examining the combined impacts of two different transverse pitch ratios and CFlowU and CFlowD flow patterns on the thermo-hydraulic performance of NIDW at Re=5000-17500. This approach not only provides a new dimension to understanding the thermal performance of NIDW but also addresses an important gap by examining the interplay between these two variables in a unified context.

MATERIAL AND METHODS

A comprehensive description of the numerical model employed in this study is presented in this section. This part also provides information regarding the validation of the model and the computational methods utilized.

Computational Model Details

The computational domain for NIDW-fitted duct is constituted by three parts, including the computational domain inlet, exit and test regions. The computational domain inlet and exit regions lengths are determined by considering the dimensions of smooth duct computational domain identified at previous work [23]. In this context, the inlet and the exit region lengths are set to L_{Inlet}= 1000 mm and L_{Exit}= 500 mm, respectively. Moreover, the channel geometry measurements from the prior numerical analysis [23] also provided a basis for determinations of the test region's height [H=30 mm], length [L_{Test}=440 mm] and width [W=300 mm], respectively. Furthermore, the dimensions of the NIDW, utilized in this numerical assessment, is presented in Figure 1. The inclination angle, angle of attack, slant angle, base-attached edge length and height of NIDW are donated as α, β, θ, k and b, respectively.
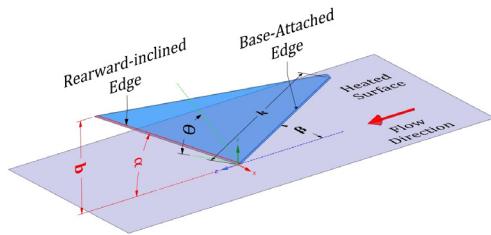
Figure 1 The dimensional definitions and isometric view of NIDW [23]

In this numerical work, detailed computational investigations are conducted on the impacts of the NIDW's transverse pitch ratio, P_t, together with its orientations, including CFlowU and CFlowD, regarding thermal performance and Darcy friction factor in the range of Re=5000-17500. It should be emphasized that, as in the previous study [23], the frontal projection areas in the plane perpendicular to the main flow are kept constant throughout all cases investigated in this work. However, unlike in the preceding research [23], the NIDW's geometry are not scaled. On the contrary, to ensure equal frontal projection areas for NIDW-CFlowU and NIDW-CFlowD cases with P_t=0.333 , the geometric dimensions are set to b=15 mm and k=30 mm for NIDW-CFlowU and NIDW-CFlowD cases at P_t=0.166, as depicted in Figure 2. Due to fact that the highest TEF values are achieved using NIDW with α=30° and β=30° in the previous work [23], the attack [β=30°] and inclination [α=30°] angles are also remained fixed in this work. Lastly, in this numerical assessment, the NIDW-CFlowU case with P_t=0.333 is considered the reference case.
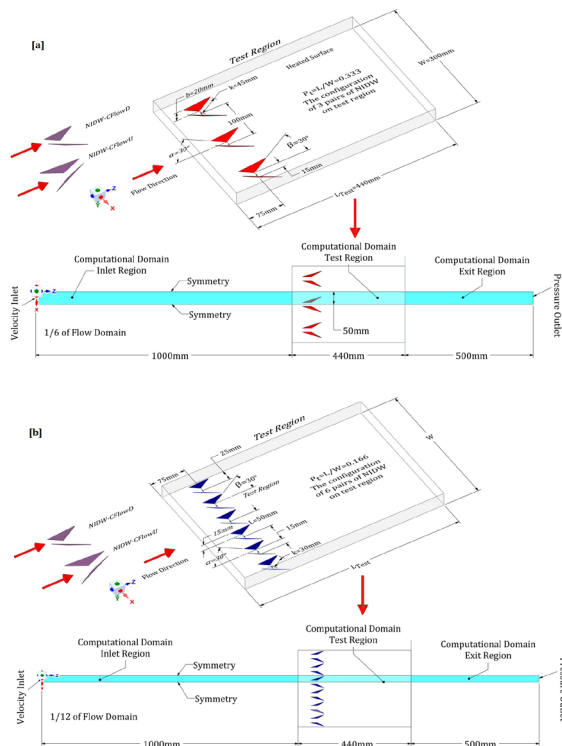

Figure 2 Geometric configurations and boundary conditions of computational domains of NIDW-CFlowD at a) P_t=0.333 and b) P_t=0.166

As illustrated in Figure 2, due to the implementation of symmetry boundary conditions within the computational fluid domain, the cases of NIDW-CFlowU or NIDW-CFlowD-fitted ducts at $P_t=L_{NIDW}/W$ [transverse spacing between two pairs of NIDW/channel width] =0.333 and 0.166, the computational domain accounts for 1/6 and 1/12 of the total flow domain, respectively. The upper wall of the rectangular duct within the test region has been designated as the heated surface on which the uniform heat flux [$q''=600W/m^2$] applied.

Mesh Structure

The performing of the mesh independence test is of great significance, not only in regard to the saving of computational resources and the reduction of time required, but also with respect to the assurance of the validity of the resulting numerical data. It should be noted, however, that, the data for the reference case of NIDW-CFlowU with P_t=0.333 [α=30° and β=30°] as well as the smooth duct data are sourced from prior work [23]. The reference case of NIDW-CFlowU with P_t=0.333 utilized grid parameters derived from a grid independence test carried out in a previous study [23]. Accordingly, a distinct mesh independence test is not conducted in the present study. Instead, the mesh structures of all cases analyzed in this numerical assessment, are generated with consideration of the mesh parameters established for the reference case. The grid structure of NIDW-CFlowD at P_t=0.333 is presented in Figure 3. As is seen in Figure 3, the mesh structure consists of a subdivision of the computational domain into different volumes, with the number of cells in the computational domain test region being greater than both the inlet and outlet of computational domains. In addition, the flow volume encapsulating the NIDW-CFlowD has a denser mesh structure than neighboring volumes in the test region. The aim of this approach is the accurate calculation of velocity and temperature gradients. For an accurate computation of the velocity gradients, the number of cells is also concentrated at the edges and corners of NIDW-CFlowD, at which the flow separates. In addition, more than 10 inflation layers are identified in all cases investigated. Furthermore, the first layer height is set to 0.05 mm and 0.025 mm for the smooth and NIDW-equipped channels, respectively. In conclusion, growth rate is set to 1.15.
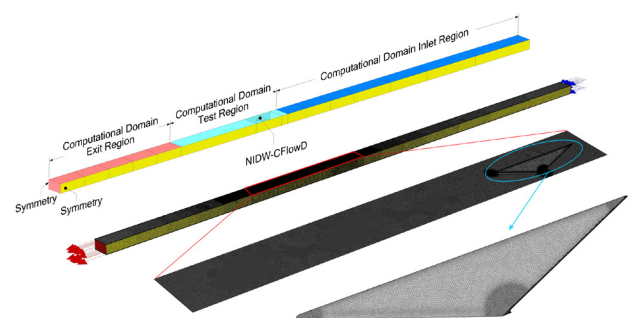

Figure 3 The computational domain grid structure consists of 8667708 polyhedral cells for the NIDW-CFlowD at P_t=0.333

Numerical Method and Data Analysis

ANSYS Fluent Computational Fluid Dynamics (CFD) software is utilized to perform numerical analysis, and the governing

equations are discretized using the finite volume approach. The convective terms are discretized with a second-order upwind approach, and the Coupled algorithm handles the pressure-velocity coupling. A three-dimensional flow simulation is conducted given the assumptions of steady state, incompressible turbulent flow, with viscous dissipation effects being excluded. More information on the numerical method and boundary conditions applied in the numerical assessment are given in previous computational study [23]. Furthermore, the numerical analysis of both the smooth and NIDW-fitted channels are performed with the utilization of non-dimensional numbers of Nusselt number (Nu), Reynolds number (Re), Darcy friction factor (f) and TEF. Further details regarding non-dimensional numbers utilized in this study is detailed in previous work [23].

Governing Equations and Turbulence Model

The numerical examination of the turbulent airflow in a rectangular duct is carried out utilizing the RANS equations. The relevant formulas of energy, momentum and continuity based on the conditions of incompressible flow and constant thermophysical parameters are given as:

Equation of Continuity

$$\frac{\partial}{\partial x_i}(\rho u_i) = 0$$

Equation of Momentum

$$\frac{\partial}{\partial x_j}(\rho u_i u_j) = -\frac{\partial P}{\partial x_i} + \frac{\partial}{\partial x_j}\left[\mu\left(\frac{\partial u_i}{\partial x_j} - \overline{\rho u_i' u_j'}\right)\right]$$

The Reynolds stress term, $-\rho\overline{u_i' u_j'}$ is detailed in Eq.-3 through the use of the Boussinesq approximation

$$-\rho\overline{u_i' u_j'} = \mu_t\left(\frac{\partial u_i}{\partial x_j} + \frac{\partial u_j}{\partial x_i}\right) - \frac{2}{3}\left(\rho k + \mu_t \frac{\partial u_i}{\partial x_i}\right)\delta_{ij}$$

Equation of Energy

$$\frac{\partial}{\partial x_i}[u_i(\rho E + P)] = \frac{\partial}{\partial x_j}\left[\left(k + \frac{C_p \mu_t}{Pr_t}\right)\frac{\partial T}{\partial x_j} + u_i(\tau_{ij})_{eff}\right]$$

$$(\tau_{ij})_{eff} = \mu_{eff}\left(\frac{\partial u_j}{\partial x_i} + \frac{\partial u_i}{\partial x_j}\right) - \frac{2}{3}\mu_{eff}\frac{\partial u_k}{\partial x_k}\delta$$

where, $(\tau_{ij})_{eff}$, c_p and k are represented by the following: energy stress tensor, specific heat capacity and thermal conductivity.

Additionally, the (SST) k-ω turbulence model is utilized because of its proven proficiency to analyze separated flows, adverse pressure gradients, and boundary layers, effectively. An adaptation of the k–ω turbulence model [24] by Menter [25], which is the (SST) k-ω turbulence model specifics are available in prior numerical assessment [23].

The Assessment of Validation Study

In general terms, the performance of a turbulence model is tested by performing simulations of chaotic flow conditions, including swirling flow, flow re-attachment, flow separation

and heat transfer analysis. Accordingly, in this first part of validation study, the Nusselt number and Darcy friction factors of the experimental work, possibly involving the above-mentioned flow conditions, are verified by employing the (SST) k-ω turbulence model. The details regarding experimental configuration and boundary conditions for the computational domain are illustrated in Figure 4, whereas Figure 5 presents the numerical Nusselt numbers (Nu) and Darcy friction factors (f) in comparison with the data derived from the experimental correlation equations. In the context of the experimental setup of DW-E at R_p=2, α=45° and b/H=0.5 [21], the computational analysis yields mean absolute deviation rates of 1.18% and 1.14% for Nu and f, respectively, in comparison to the experimental correlation data. The suitability of the (SST) k-ω turbulence model for further investigations is confirmed by the close agreement between the data sets. It is also important to note that in the previous numerical assessment, the smooth channel Darcy friction factor (f_0) and Nusselt number (Nu_0) are verified by comparison with the Petukhov and Dittus-Boelter correlation equations, respectively [23].
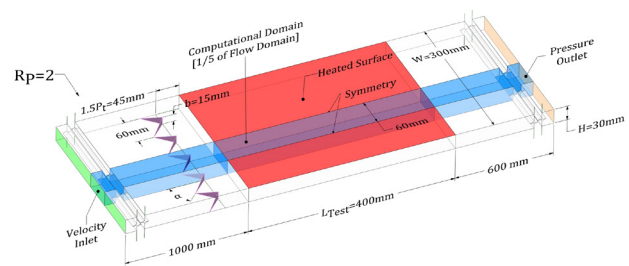

Figure 4 The visual illustration of experimental setup and the corresponding boundary conditions regarding to the computational domain (denoted in blue) for DW-E at R_p=2, α=45° and b/H=0.5
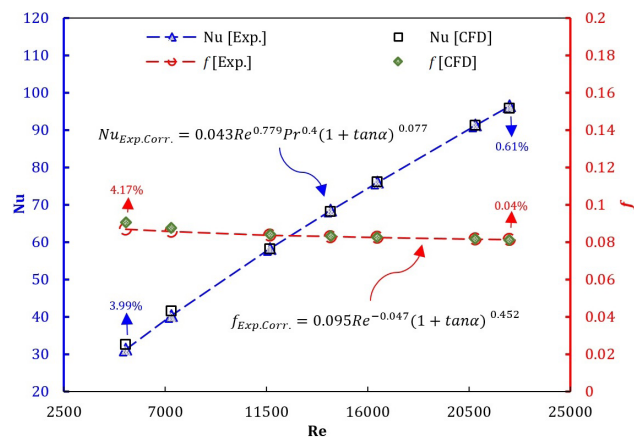
Figure 5 The verification of DW-E at R_p=2, α=45° and b/H=0.5 with an experimental correlation data

Furthermore, in the second part, the objective is to provide additional evidence to demonstrate the performance of the (SST) k-ω turbulence model. In this regard, the validation study is also carried out in local manner at Re=15000. Accordingly, local Nu_x/Nu_0 ratio of inline 60° V-discrete ribs are verified for z/D=1/4 at Re=15000. The numerical setup

of inline 60° V-discrete ribs [26][27] and the corresponding boundary condition for the computational domain (1/4 of periodic module) are illustrated in Figure 6.

Figure 6 The visual representation of inline 60° V-discrete ribs and the corresponding boundary conditions regarding to the periodic computational domain (denoted in yellow) [26][27]
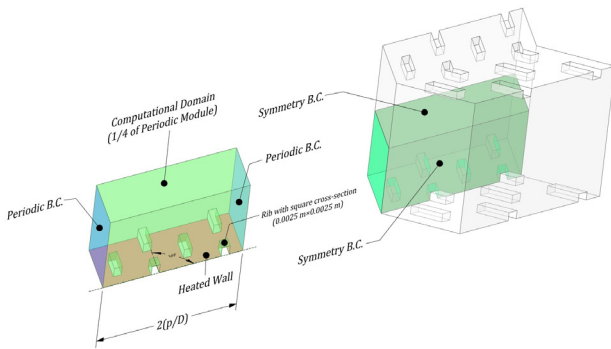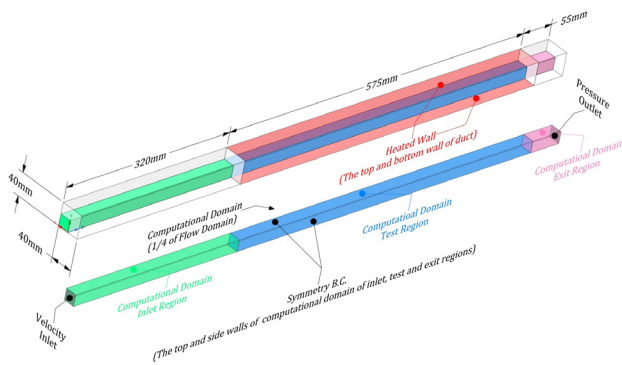

Figure 7 The schematic representation of smooth channel with a square cross-section and the corresponding boundary conditions regarding to the computational domain [27]

Additionally, smooth channel validation study is also undertaken at Re=15000 to calculate Nu_x/Nu_0 ratio at z/D=1/4. The schematic representation of the smooth duct, together with the corresponding boundary conditions for its computational domain, is shown in Figure 7.
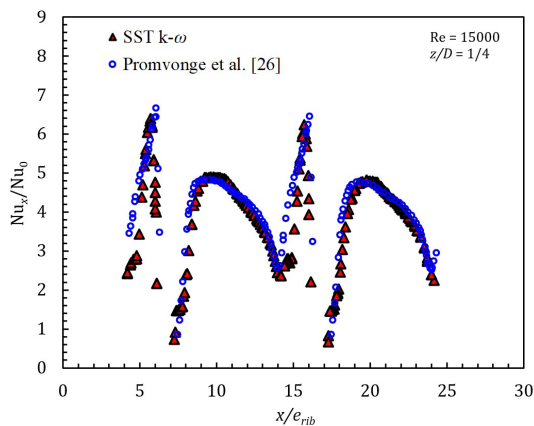

Figure 8 The verification of local Nux/Nu0 ratios for z/D=1/4 at Re=15000

The resulting numerical data indicate that the deviation rate for Nu_0 and f_0 with respect to the Dittus-Boelter and Petukhov correlation equations is 0.82% and 9.65%, respectively. Notably, the local Nu_x/Nu_0 ratios demonstrate excellent agreement with the numerical data from the study conducted by Promvonge et al. [26], as illustrated in Figure 8.

RESULTS AND DISCUSSIONS

This section presents a comprehensive investigation focusing into the influence of NIDW in different orientations, including CFlowD and CFlowU configurations at P_t=0.333 and P_t=0.166, on convective heat transfer performance and friction factor characteristics. In this section, all data for the smooth channel and NIDW-CFlowU at P_t=0.333 cases are sourced from the prior study [23].

Heat Transfer

The Nusselt number change of the positioning of NIDW in different orientations at P_t=0.333 and P_t=0.166 across the range of Reynolds numbers from 5000 to 17500 is given in the Figure 9-a, b, c, d. In a manner analogous to the behavior observed in smooth duct, the Nusselt number demonstrates a progressive increase as the Reynolds number is elevated. The underlying mechanism behind this phenomenon can be attributed to the intensified velocities of turbulent eddies, which increase interaction with the thermal boundary layer and thereby enhance convective heat transfer. The motion of eddies through the fluid results in the disruption of the boundary layer. This occurs as a consequence of the exchange of fluid in different temperatures, with the cooler core fluid mixing with the warmer fluid at the surface. The resulting increase in thermal resistance close to the wall is reduced by this process of enhanced mixing, resulting in a greater overall heat transfer rate within the system. The augmentation in convective heat transfer yields an elevated Nusselt number. It can therefore be concluded that in all cases examined, the maximum Nusselt numbers are achieved at the highest Reynolds number investigated. Furthermore, the insertion of NIDWs at diverse orientations and transverse pitch ratios into channel's flow domain has been observed to result in an elevated Nusselt number in comparison to the case of smooth channel at Re=5000-17500.

The longitudinal vortices produced by the NIDW [Figure 10], contribute to the enhancement of Nusselt number by being effective along the test region. This is because a swirling flow pattern disrupts the orderly movement of the fluid and increases the chaotic nature of the fluid, which further increases the rate of mixing of low and high temperature fluids.

Furthermore, vortices elevate the local velocity of the fluid in the vicinity of the heated surface, which inhibits the expansion of the thermal boundary layer on heated surface. Therefore, in comparison to the smooth channel case, there is a notable reduction in the area-weighted average static temperature of heated surface, providing a definitive indication of the rise in Nusselt number for NIDW-CFlowU and NIDW-CFlowD at P_t=0.333 and P_t=0.166, as demonstrated in Figure 11.
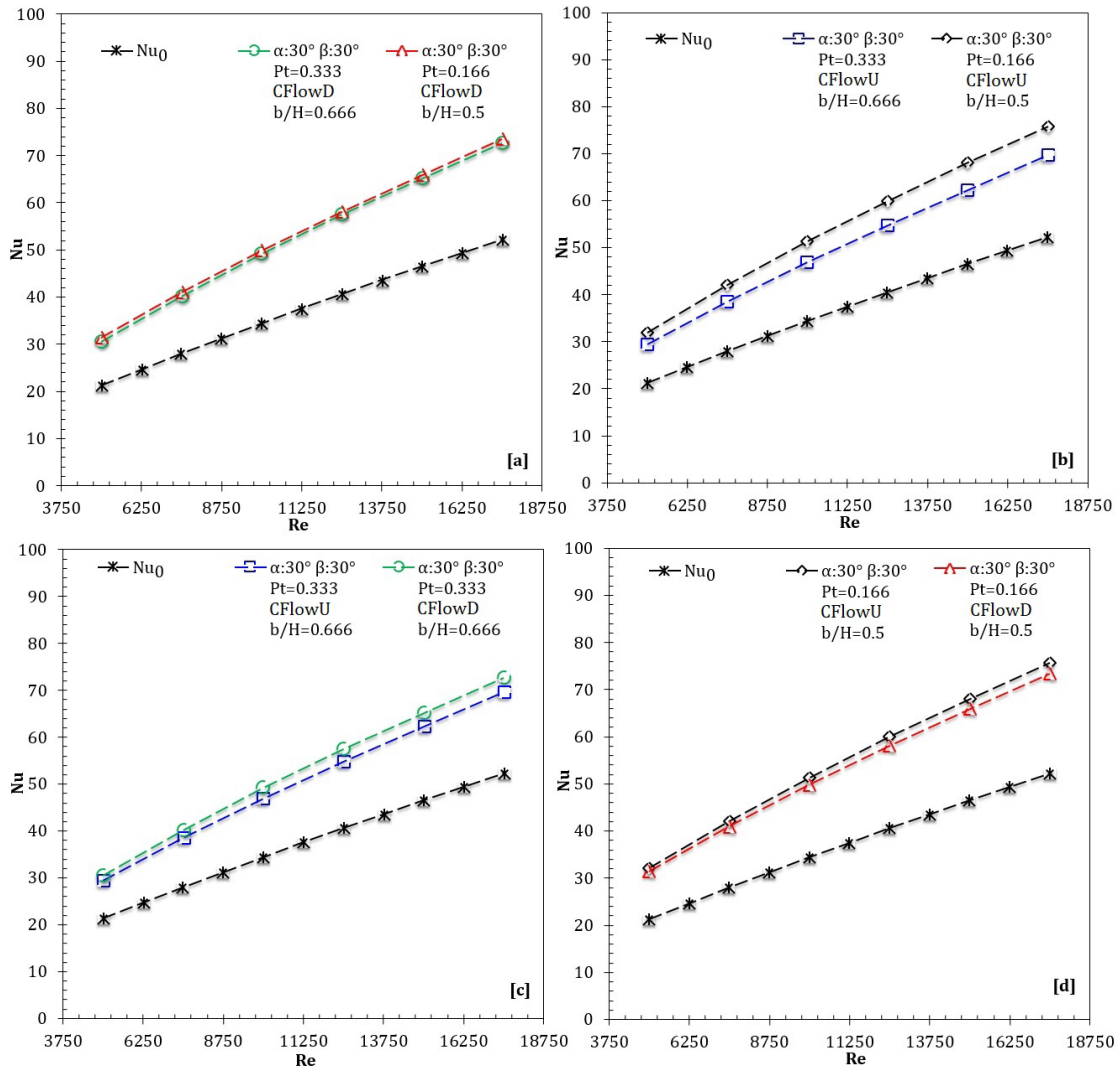
Figure 9 The variation of Nu number for a) NIDW-CFlowD at P_t=0.333 and P_t=0.166 b) NIDW-CFlowU at P_t=0.333 and P_t=0.166 c) NIDW-CFlowD and NIDW-CFlowU at P_t=0.333 d) NIDW-CFlowD and NIDW-CFlowU at P_t=0.166

Moreover, the time-averaged contour maps of the static temperature variation in conjunction with the local Nusselt number distribution demonstrate that the lowest static temperature and the corresponding highest local surface Nusselt number are observed at the trailing end of the vortex generator besides the entrance of the heated surface in all cases examined. The formation of the strongest vortices right behind the NIDW, and the subsequent gradual weakening of the vortices in the direction of the main flow as a result of viscous forces, provide a clear explanation for this situation. Nevertheless, even at the endpoint of the test region, they still continue to exert an influence on the growth of the thermal boundary. However, when comparing the effects of positioning the NIDW in different orientations and transverse pitch ratios on thermal behavior, a significant difference is observed in each cases.
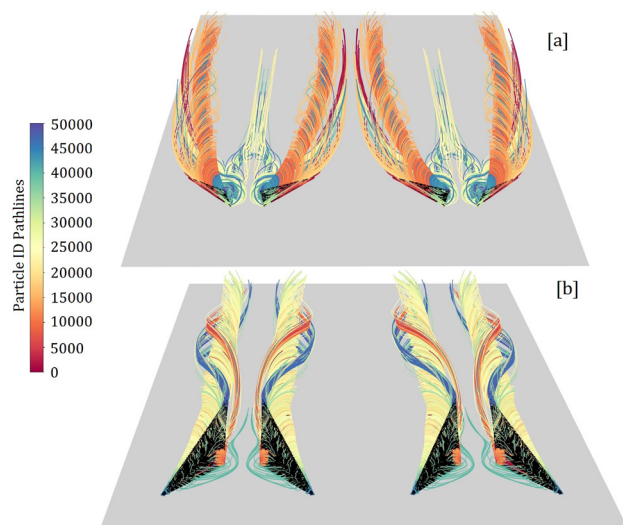

Figure 10 The 3D representation of longitudinal vortices produced by a) NIDW-CFlowD and b) NIDW-CFlowU at Re=17500
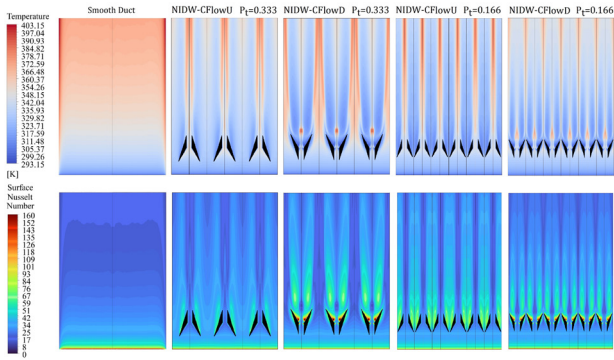
Figure 11 The time-averaged contour maps of static temperature and local Nu number variations of heated surface for both smooth duct and NIDW-fitted duct, including CFlowU and CFlowD arrangements for P_t=0.333 and 0.166 at Re=5000

With regard to the impact of transverse pitch ratio on convective heat transfer performance, the highest Nusselt numbers are observed within the range of Re=5000-17500 for P_t=0.166 and P_t=0.333, respectively when NIDW is positioned in either CFlowU or CFlowD orientations as plotted in Figure 9-a and Figure 9-b. This is attributed to the presence of a double number of longitudinal vortices along the heated surface in the case of P_t=0.166 compared to the transverse pitch ratio of P_t=0.333. The closer spacing between NIDWs in the case of P_t=0.166 results in intensified vortex-thermal boundary layer interactions, which disrupt the growth of thermal boundary layer more vigorously. This, in turn, enhances turbulent mixing high-and low-temperature fluid zones in flow domain, leading to reduced thermal resistance and resulting in an increased Nusselt number in comparison to the transverse pitch ratio of P_t=0.333. However, when NIDW is positioned in the CFlowD orientation, the increase in Nusselt number is negligibly small at P_t=0.166 in comparison to the transverse pitch ratio of P_t=0.333 (Figure 9-a) and thus, similar Nusselt numbers are obtained in the range of Re=5000-25000. Conversely, the elevation in Nusselt numbers are significantly higher at P_t=0.166 than at P_t=0.333 when NIDW is in the CFlowU pattern as given in Figure 9-b. The observed rise in Nusselt number is predominantly attributable to the longitudinal vortices generated by NIDW-CFlowD, whose rotation centers exhibit a tendency to spread farther apart in the direction of the mainstream, as illustrated in Figure 10 and Figure 12. This phenomenon lessens the influence of vortices on the heated surface along the flow direction while increasing their contact with one another. Therefore, while vortices are found to be effective right behind NIDW in both the CFlowU and CFlowD arrangements (Figure 11), their impact on heated surface in the CFlowD configuration is less pronounced than it is in the CFlowU configuration at P_t=0.166. Accordingly, for NIDW in the CFlowU configuration at P_t=0.166, lower temperature values are obtained over a significantly larger area of the heated surface than NIDW-CFlowD, as depicted in Figure 11, and thus higher Nusselt numbers are obtained spanning Reynolds number between 5000 and 17500, as plotted in Figure 9-d. Moreover, by examining the time-averaged streamline velocity distributions at six planes perpendicular to the main flow, dimensionless distance [$P=x/L$] ranging from P1 = 0.25 to P6 = 0.875, within the computational domain

test region, it was determined that in the CFlowD pattern, a tendency of vortex centers to spread apart in the direction of the main flow has a noticeable adverse impact on thermal performance, when P_t=0.166. In contrast to the CFlowU arrangement, this tendency caused the vortex centers to drift away from the heating surface, where NIDW is situated (Figure 12), and thus negatively affecting the enhancement of convective heat transfer.

However, an opposing trend has been noted in the instance of P_t=0.333 as presented in Figure 9-c. As illustrated in Figure 12, the vortices generated by the CFlowD pattern exert a considerable shear stress near the heated surface with the centers of the main vortices positioned much nearer to the heated wall along the test region in comparison to the CFlowU orientation, thereby promoting enhanced cross-sectional mixing and intensifying thermal boundary interaction, which leads to higher convective heat transfer at P_t=0.333. Additionally, although the separation of the eddies' centers in the main flow direction causes interaction between the vortices to be increased, as previously stated, the positioning of the NIDW in the CFlowD configuration at P_t=0.333 allows for the formation of additional secondary vortices between the two main vortices as depicted in Figure 10. This is because the spacing between the vortices is not small enough as in the case of P_t=0.166, to significantly influence one another negatively. This phenomenon provides an explanation for the attainment of higher Nusselt numbers, particularly just behind the NIDW-CFlowD at P_t=0.333, as depicted in Figure 11.

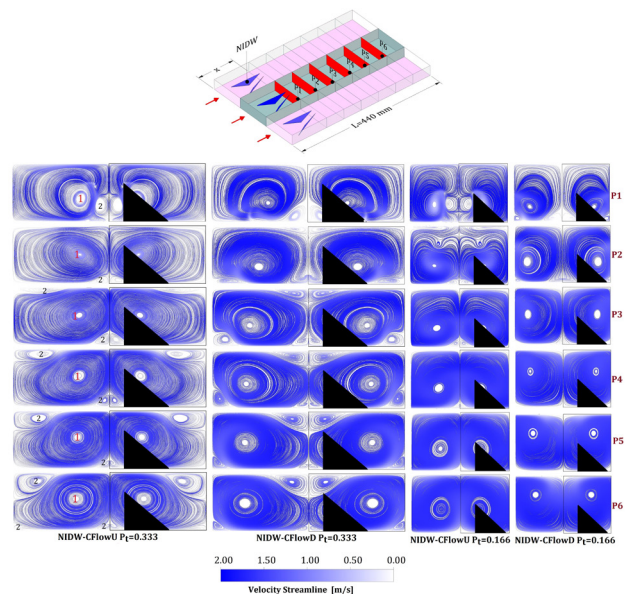**Figure 12** The time-averaged streamline velocity distribution at P1=0.25, P2=0.375, P3=0.5, P4=0.625, P5=0.75 and P6=0.875 for NIDWs in CFlowU and CFlowD orientations at P_t=0.333 and 0.166 at Re=5000

Friction Factor

The Darcy friction factor, f, changes in NIDW positioning in different orientations at two different transverse pitch ratios together with the smooth channel Darcy friction factors are
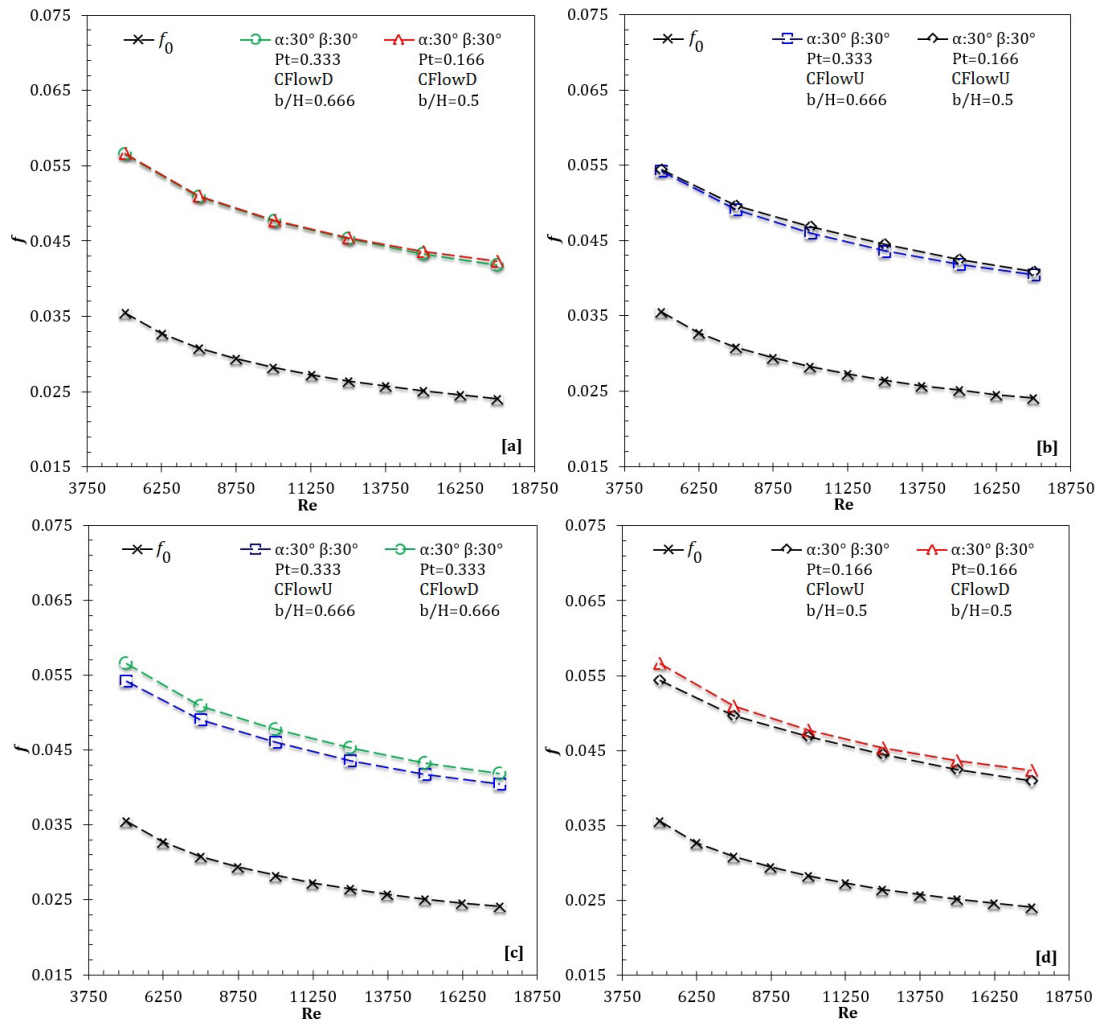
Figure 13 The variation of f for a) NIDW-CFlowD at P_t=0.333 and P_t=0.166 b) NIDW-CFlowU at P_t=0.333 and P_t=0.166 c) NIDW-CFlowD and NIDW-CFlowU at P_t=0.333 d) NIDW-CFlowD and NIDW-CFlowU at P_t=0.166

In the present study, the effects of the transverse pitch ratio and the impacts of the configurations of CFlowU and CFlowD, are considered independently of the frontal projected area. Consequently, the frontal projected areas normal to the main stream are held constant in each case examined. Accordingly, the aforementioned factors, which exert a relatively minor influence on the rise in pressure loss across the test region, play an effective role in the rise in the friction factor as plotted Figure 13-c, and Figure 13-d. As previously stated, a comparison of the CFlowU and CFlowD orientations at each case of P_t=0.166 or P_t=0.333 reveals that despite both having an equal total frontal projection areas, there are notable differences in the resulting Darcy friction factors. The CFlowD configurations of NIDW are calculated to attain higher Darcy friction factor values covering the Reynolds number range from 5000 to 17500 for both transverse pitch ratios, as plotted in Figure 13-c, and Figure 13-d. The underlying reason of this phenomenon can be attributed to the tendency of vortex centers to diverge in the direction of the main flow when the NIDW is positioned in CFlowD configuration. In order to provide a visual illustration of the resulting data, the Q-criterion based vortex structures are presented for each cases, investigated, comparatively in Figure 14. As illustrated

in Figure 14, the notable interaction between the vortices is evidently apparent for the NIDW-CFlowD, positioning under a transverse pitch ratio of P_t=0.166, resulting in the highest Darcy friction factor in the range Re=5000-17500.

Another significant finding is that the presence of a double number of longitudinal vortices in the case of P_t=0.166 results in higher Darcy friction factor for NIDW-CFlowD and NIDW-CFlowU-fitted channels at Re=5000-17500 as plotted in Figure 13-a, and Figure 13-b, respectively. In other words, the increase in the number of longitudinal vortices in a single row intensifies eddy interactions within each channel, thereby enhancing turbulence and disrupting the boundary layer in the vicinity of the channel walls to a greater extent. This disruption results in an increased momentum exchange between the vortices and the channel wall, which in turn raises the drag and consequently yields higher flow resistance. As a result, the channels fitted with NIDW-CFlowU and NIDW-CFlowD at P_t=0.166 exhibit higher Darcy friction factors compared to those at P_t=0.333.
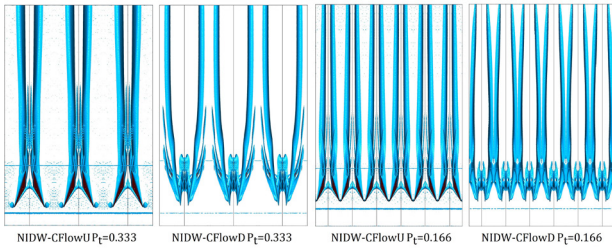
NIDW-CFlowU P_t=0.333   NIDW-CFlowD P_t=0.333   NIDW-CFlowU P_t=0.166   NIDW-CFlowD P_t=0.166

Figure 14 The comparison of vortex structures illustrated by Q-criterion

THERMAL ENHANCEMENT FACTOR

The changes in TEF for NIDWs mounted in rectangular channel in various flow patterns, including CFlowU and CFlowD configurations and transverse pitch ratios, are presented in a comparable way in Figure 15-a, b, c, d. In all cases examined, including NIDW-CFlowD at P_t=0.166 and P_t=0.333 and the NIDW-CFlowU at P_t=0.166 and P_t=0.333, a decreasing trend in the TEF values are obtained with a rise in Reynolds number, ranging from 5000 to 17500. Furthermore, the TEF values for both CFlowD and CFlowU flow patterns in the Re=5000–17500 range, are calculated to be higher at

P_t=0.166 than at P_t=0.333 as shown in Figure 15-a and Figure 15-b, respectively. This is due to the increase in the number of longitudinal vortices along test region, leading to a larger increase in convective heat transfer in comparison to the rise in friction factor. Moreover, the rise in TEF values is even more pronounced in CFlowU flow pattern in comparison to CFlowD configuration (Figure 15-b) due to previously mentioned factor of which is the divergence tendency of vortices in the mainstream direction.

However, when the effects of different flow patterns on TEF at constant transverse pitch ratios are examined comparatively, CFlowU flow pattern is more favorable in case of P_t=0.166 (Figure 15-d), whereas there is an opposite trend in case of P_t=0.333 (Figure 15-c) is present and thus, higher TEF values are obtained when NIDW is positioned in CFlowD orientation at P_t=0.333 within the range of Re=5000-17500. As a result, the TEF values obtained by positioning NIDW-CFlowU and NIDW-CFlowD in the rectangular channel at P_t=0.333 and P_t=0.166 at Re = 5000 - 17500 are calculated to be between 1.221-1.122 and 1.325-1.215 (CFlowU); 1.244-1.157 and 1.279-1.165 (CFlowD), respectively. Accordingly, the highest TEF value of 1.325 is achieved with an insertion of NIDW-CFlowU at P_t=0.166 and Re=5000.

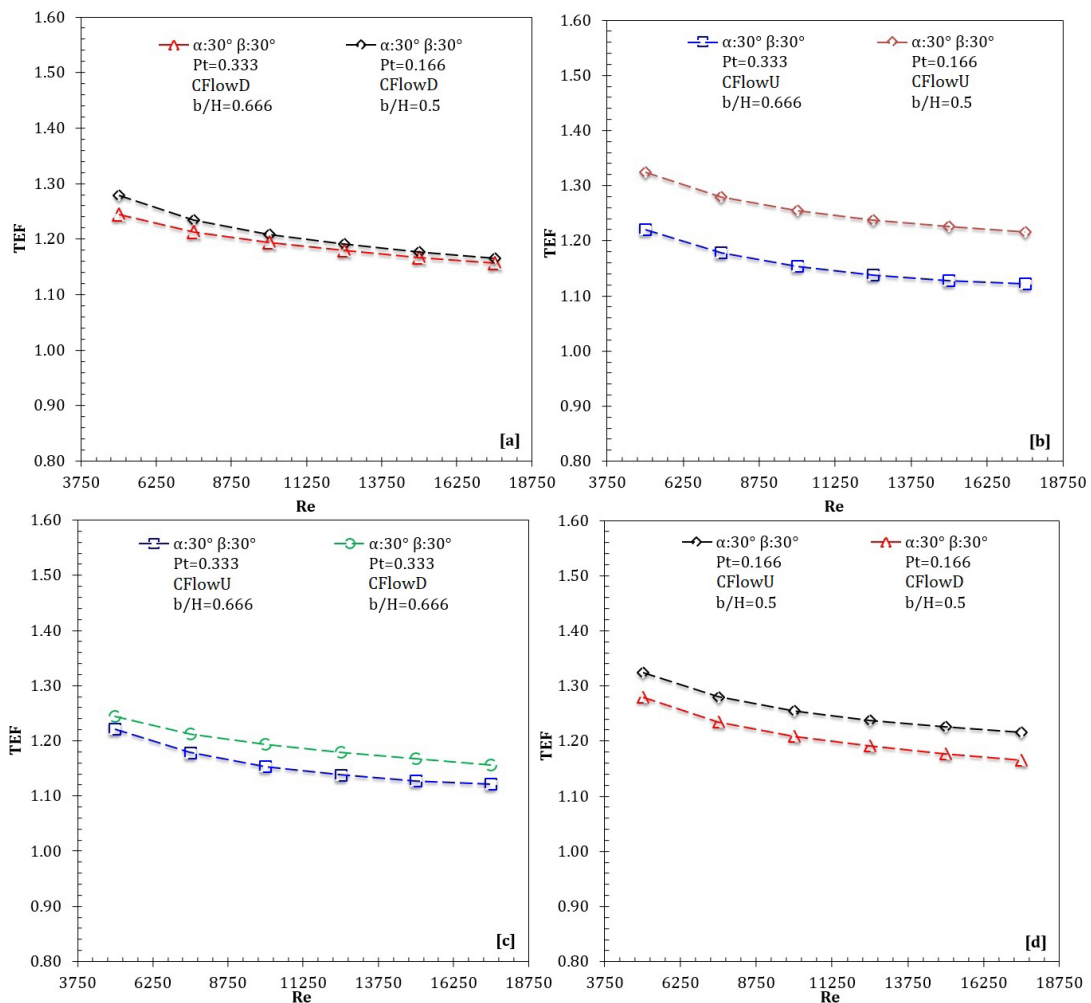
Figure 15 The variation of TEF for a) NIDW-CFlowD at P_t=0.333 and P_t=0.166 b) NIDW-CFlowU at P_t=0.333 and P_t=0.166 c) NIDW-CFlowD and NIDW-CFlowU at P_t=0.333 d) NIDW-CFlowD and NIDW-CFlowU at P_t=0.166

CONCLUSION

This computational examination focuses on the influence of orientation-based factors, encompassing CFlowU and CFlowD flow patterns and transverse pitch ratios of P_t=0.166 and P_t=0.333, regarding thermal performance and flow behaviors at Re=5000-17500. In numerical analysis, both the angle of attack [β=30°] and the angle of inclination [α=30°] are kept constant. Various combinations with the same frontal projection areas of the NIDW are investigated in terms of thermo-hydraulic performance in detail in a comparative manner.

The following represents a summary of the conclusions:

- The configurations of CFlowU and CFlowD along with the transverse pitch ratio have notable influence on the enhancement of heat transfer performance and flow characteristics as well. Although the presence of the double number of longitudinal vortices has a significant impact on the increase of both the Nusselt number and the Darcy friction factor, the orientation of the NIDW plays a key role. Thus, the highest Darcy friction factor and Nusselt number are obtained with the insertion of NIDW-CFlowD and NIDW-CFlowU at P_t=0.166.
- The distance between the vortex centers within the flow volume exhibited no discernible change in the CFlowU configuration as a result of arranging the NIDWs in various transverse pitch ratios. Nonetheless, at P_t=0.166 and P_t=0.333, it was noted that the centers of vortices in the CFlowD setup became increasingly farther apart in the main flow direction. Additionally, the tendency forced centers of vortices to shift away from the heated surface as well at P_t=0.166.
- The CFlowD configuration at P_t=0.166 has a negative effect on the heat transfer performance due to the tendency of the vortices to diverge in the direction of the main flow. However, the distance between the NIDWS at P_t=0.333 is sufficient to trigger the formation of secondary vortices along with the main vortices, resulting in the higher Nusselt numbers being achieved.
- The maximum and minimum TEF values are achieved between 1.325 - 1.215 and 1.221 - 1.122 for the cases of NIDW-CFlowU with P_t=0.166 and NIDW-CFlowU with P_t=0.333, respectively.

Acknowledgment

References

1. Goel V, Hans VS, Singh S, Kumar R, Pathak SK, Singla M, et al. A comprehensive study on the progressive development and applications of solar air heaters. Sol Energy 2021. https://doi.org/10.1016/j.solener.2021.07.040.
2. Yadav AS, Mishra A, Dwivedi K, Agrawal A, Galphat A, Sharma N. Investigation on performance enhancement due to rib roughened solar air heater. Mater Today Proc 2022. https://doi.org/10.1016/j.matpr.2022.05.071.
3. Ghritlahre HK, Sahu PK, Chand S. Thermal performance and heat transfer analysis of arc shaped roughened solar air heater – An experimental study. Sol Energy 2020. https://doi.org/10.1016/j.solener.2020.01.068.
4. Ahirwar B kumar, kumar A. Review on different techniques used to enhance the thermal performance of solar air heater. Int J Heat Mass Transf 2024. https://doi.org/10.1016/j.ijheatmasstransfer.2023.124979.
5. Chompookham T, Eiamsa–ard S, Buanak K, Promvonge P, Maruyama N, Hirota M, et al. Thermal performance augmentation in a solar air heater with twisted multiple V–baffles. Int J Therm Sci 2024;205:109295. https://doi.org/10.1016/j.ijthermalsci.2024.109295.
6. Kumar R, Chand P. Performance enhancement of solar air heater using herringbone corrugated fins. Energy 2017. https://doi.org/10.1016/j.energy.2017.03.128.
7. Saravanan A, Murugan M, Reddy MS, Ranjit PS, Elumalai P V., Kumar P, et al. Thermo-hydraulic performance of a solar air heater with staggered C-shape finned absorber plate. Int J Therm Sci 2021. https://doi.org/10.1016/j.ijthermalsci.2021.107068.
8. Biswas G, Chattopadhyay H, Sinha A. Augmentation of heat transfer by creation of streamwise longitudinal vortices using vortex generators. Heat Transf Eng 2012. https://doi.org/10.1080/01457632.2012.614150.
9. He J, Liu L, Jacobi AM. Air-side heat-transfer enhancement by a new winglet-type vortex generator array in a plain-fin round-tube heat exchanger. J Heat Transfer 2010. https://doi.org/10.1115/1.4000988.
10. Chang LM, Wang LB, Song KW, Sun DL, Fan JF. Numerical study of the relationship between heat transfer enhancement and absolute vorticity flux along main flow direction in a channel formed by a flat tube bank fin with vortex generators. Int J Heat Mass Transf 2009. https://doi.org/10.1016/j.ijheatmasstransfer.2008.09.029.
11. Min C, Qi C, Kong X, Dong J. Experimental study of rectangular channel with modified rectangular longitudinal vortex generators. Int J Heat Mass Transf 2010. https://doi.org/10.1016/j.ijheatmasstransfer.2010.03.026.
12. Xu Z, Han Z, Wang J, Liu Z. The characteristics of heat transfer and flow resistance in a rectangular channel with vortex generators. Int J Heat Mass Transf 2018. https://doi.org/10.1016/j.ijheatmasstransfer.2017.08.083.
13. Ke Z, Chen CL, Li K, Wang S, Chen CH. Vortex dynamics and heat transfer of longitudinal vortex generators in a rectangular channel. Int J Heat Mass Transf 2019. https://doi.org/10.1016/j.ijheatmasstransfer.2018.12.064.
14. Kim E, Yang JS. An experimental study of heat transfer characteristics of a pair of longitudinal vortices using color capturing technique. Int J Heat Mass Transf 2002. https://doi.org/10.1016/S0017-9310(02)00054-6.
15. Tian LT, He YL, Lei YG, Tao WQ. Numerical study of fluid flow and heat transfer in a flat-plate channel with longitudinal vortex generators by applying field synergy principle analysis. Int Commun Heat Mass Transf 2009. https://doi.org/10.1016/j.icheatmasstransfer.2008.10.018.
16. Md Salleh MF, Gholami A, Wahid MA. Numerical evaluation of thermal hydraulic performance in fin-and-tube heat exchangers with various vortex generator geometries arranged in common-flow-down or common-flow-up. J Heat Transfer 2019;141. https://doi.org/10.1115/1.4041832.
17. Fu H, Sun H, Yang L, Yan L, Luan Y, Magagnato F. Effects of the configuration of the delta winglet longitudinal vortex generators and channel height on flow and heat transfer in

minichannels. Appl Therm Eng 2023. https://doi.org/10.1016/j.applthermaleng.2023.120401.

18. Song KW, Wang L, Hu YJ, Liu Q. Flow symmetry and heat transfer characteristics of winglet vortex generators arranged in common flow up configuration. Symmetry (Basel) 2020. https://doi.org/10.3390/sym12020247.

19. Tanaka T, Itoh M, Hatada T, Matsushima H. Influence of inclination angle, attack angle, and arrangement of rectangular vortex generators on heat transfer performance. Heat Transf - Asian Res 2003. https://doi.org/10.1002/htj.10089.

20. Dogan M, Erzincan S. Experimental investigation of thermal performance of novel type vortex generator in rectangular channel. Int Commun Heat Mass Transf 2023. https://doi.org/10.1016/j.icheatmasstransfer.2023.106785.

21. Skullong S, Promvonge P. Experimental investigation on turbulent convection in solar air heater channel fitted with delta winglet vortex generator. Chinese J Chem Eng 2014. https://doi.org/10.1016/S1004-9541(14)60030-6.

22. Hu J, Zhang Y, Xie S, Xiao Y. Thermo-hydraulic performance of solar air heater with built-in one-eighth sphere vortex generators. Appl Therm Eng 2024. https://doi.org/10.1016/j.applthermaleng.2024.122837.

23. Demirağ HZ. Innovative approach for longitudinal vortex generator design: Impact on thermal performance. Therm Sci Eng Prog 2024. https://doi.org/10.1016/j.tsep.2024.102444.

24. Wilcox DC. Turbulence Modeling for CFD (Third Edition). DCW Ind 2006.

25. Menter FR. Two-equation eddy-viscosity turbulence models for engineering applications. AIAA J 1994. https://doi.org/10.2514/3.12149.

26. Promvonge P, Changcharoen W, Kwankaomeng S, Thianpong C. Numerical heat transfer study of turbulent square-duct flow through inline V-shaped discrete ribs. Int Commun Heat Mass Transf 2011. https://doi.org/10.1016/j.icheatmasstransfer.2011.07.014.

27. SriHarsha V, Prabhu S V., Vedula RP. Influence of rib height on the local heat transfer distribution and pressure drop in a square channel with 90° continuous and 60° V-broken ribs. Appl Therm Eng 2009. https://doi.org/10.1016/j.applthermaleng.2008.12.015.

Polyvinylalcohol/Polyethyleneimine Hydrogels: Evaluation of Swelling, Dehydration and Antibacterial Activity

Emel Tamahkar[1,*] |Bengi Özkahraman[2,*] |Gülşen Bayrak[3] |Işık Perçin[3]
Zeynep Ciğeroğlu[4] |Filiz Boran[5]

[1]Bursa Technical University, Faculty of Engineering and Natural Sciences, Department of Bioengineering, Bursa, Türkiye
[2]Hitit University, Faculty of Engineering, Department of Polymer Engineering, Corum, Türkiye
[3]Hacettepe University, Faculty of Science, Department of Biology, Ankara, Türkiye
[4]Usak University, Faculty of Engineering and Natural Sciences, Department of Chemical Engineering, Usak, Türkiye
[5]Hitit University, Faculty of Engineering, Department of Chemical Engineering, Corum, Türkiye

Corresponding Author
Emel Tamahkar & Bengi Özkahraman
E-mail: emel.irmak@btu.edu.tr, bengiozkahraman@hitit.edu.tr
RORID[1]: https://ror.org/03rdpn141 RORID[2]: https://ror.org/01x8m3269

Cite As
Tamahkar E. & Ozkahraman B, et al. Polyvinylalcohol/Polyethyleneimine Hydrogels: Evaluation of Swelling, Dehydration and Antibacterial Activity. Hittite J Sci Eng. 2024;11(4):181-189.

Polyvinylalcohol/Polyethyleneimine Hydrogels: Evaluation of Swelling, Dehydration and Antibacterial Activity

Emel Tamahkar[1,*]|Bengi Özkahraman[2,*]|Gülşen Bayrak[3]|Işık Perçin[3]| Zeynep Ciğeroğlu[4]|Filiz Boran[5]

[1]Bursa Technical University, Faculty of Arts, Department of Bioengineering, Bursa, Türkiye
[2]Hitit University, Faculty of Engineering, Department of Polymer Engineering, Corum, Türkiye
[3]Hacettepe University, Faculty of Science, Department of Biology, Ankara, Türkiye
[4]Usak University, Faculty of Engineering, Department of Chemical Engineering, Usak, Türkiye
[5]Hitit University, Faculty of Engineering, Department of Chemical Engineering, Corum, Türkiye

Abstract

In the present study, Polyvinylalcohol/polyethyleneimine (PVA/PEI) hydrogels designed with different Glutaraldehyde (Glu) amount, PEI amount and PVA concentration were synthesized via solvent casting technique. The fabricated PVA/PEI hydrogels with different compositions were evaluated for swelling rate, dehydration properties and antibacterial activity to determine superior combination. The swelling tests were performed for 0-300 min at pH 7.4 and 37 °C. All of the prepared PVA/PEI hydrogels swelling ratio were observed in the range of 221-321%. The highest dehydration rate was found for the PVA/PEI hydrogel with the lowest PVA concentration and the lowest dehydration rate was found for the PVA/PEI hydrogel with the highest Glu amount. All the PVA/PEI hydrogels demonstrated high antibacterial activity against *E.coli.* PP5 (prepared with 5% PVA, 0.5 mL PEI and 30 μL Glu) was determined as the selected hydrogels with optimized characteristics in respect to swelling, dehydration and antibacterial activity data. This study highlights potential usage of the resultant PVA/PEI hydrogels as antibacterial wound dressings in wound care applications.

Keywords: Polyvinylalcohol, polyethyleneimine, swelling rate, dehydration properties, antibacterial activity

INTRODUCTION

The hydrogels are crosslinked three-dimensional highly hydrophilic network polymers that the origin of the term hydrogel goes back to 1894 [1]. There has been received special attention because of their acidic or basic pendant groups such as carboxylic acid (-COOH) [2] sulfonic acid ($-SO_3H$) [3], primary amine ($CONH_2$) [4] and quaternized ammonium ($NR+_4$) [5]. Hence, these polymeric matrices able to hold a huge amount of water and biological fluids due to this groups.

In general, hydrogels swelling behavior takes places as a result of ionization. Thanks to the ionization property, it is possible to absorb the water formed in the hydrophilic functional groups connected to the polymer chains. Moreover, swelling behavior of the hydrogels depends on the swelling properties of hydrogels, polymer structure (hydrophilicity or hydrophobicity etc), polymer–solvent interactions (valence of counter ion of external swelling medium), and cross-linking density [6]. The swelling and deswelling behavior of hydrogel are important to improve the understanding of mechanism due to usage in for biomedical and industrial applications including agrochemistry [7], wastewater treatment [4], drug delivery systems [8], wound dressing [9], tissue engineering [10].

Polyethyleneimine (PEI) has received increased attention due to its cationic hydrophilic nature with the presence of amine groups (primary, secondary and tertiary amino) [11]. The hydrophilic character provides good water swelling capacity. Furthermore, high positive charges of the PEI responsive for antibacterial activity [12]. Poly (vinyl alcohol) (PVA) is biodegradable, biocompatible, non-toxic and eco-friendly which can be potentially used for promising biomaterials [13–15]. PVA exhibits water solubility properties thanks to its hydroxyl groups (-OH) [16]. Due to its hydrophilic character, the addition of a polymeric system can increase the swelling capacity. Glutaraldehyde (Glu) is a common chemical crosslinking agent for PVA polymer systems due to its high crosslinking rate [17, 18]. Glu has two aldehyde groups one of

may react with the hydroxyl group of polyvinyl alcohol [19]. There are very few studies in the literature addressing possible potential applications of copolymeric PEI and PVA hydrogels. In one of these studies, Wang et al., successfully prepared stretchable elastomer composite hydrogel based on PEI and PVA. Prepared hydrogels demonstrated excellent mechanical properties and high biocompatibility. With obtained results PVA and PEI hydrogels can be used different application areas such as healthcare monitoring, human–machine interfaces and soft robots [20]. In a following study, the biosensor application is entrapment of thermolysin enzyme into a PVA/PEI matrix containing gold nanoparticles and cross-linked using Glu vapors were shown to produce successfully [21]. Also, it has been well supported that heavy metal Cr (VI) was highly effective removal from aqueous solutions and exhibits a good reusability [22]. In the present study, we successfully fabricated PVA and PEI based hydrogels using Glu as crosslinker via solvent casting method. PVA/PEI hydrogels were fabricated with different amounts of Glu, PEI and PVA. The PVA/PEI hydrogels were investigated for swelling and dehydration properties as well as antibacterial performances against *E. coli.*

MATERIALS AND METHODS

Chemicals and Materials

PVA (Mw 146000-186000; 99% hydrolyzed), PEI (average Mn ~1,800 by GPC, 50 wt. % in H2O) and Glu obtained from Sigma Aldrich. Luria Bertani (LB) agar and LB broth were obtained from Merck. All the other chemicals used were of analytical grade etc.

Preparation of PVA/PEI Hydrogels

PVA/PEI hydrogels with different combination of PVA, PEI and Glu were prepared via solvent casting method. Firstly, PVA was dissolved in distilled water at 90°C under magnetic stirring for 2 h. Then, PEI was added drop by drop to the PVA solution with vigorous mixing. PVA and PEI was interacted for 30 min to form a homogeneous solution. Glu as a crosslinker was added to the solution dropwise in the ice bath under

magnetic stirring. The mixture was poured onto 24-well plate and solvent was evaporated slowly at room temperature. Lastly, the hydrogels were dried under vacuum at 40°C for 4 h. The amounts of the components used for the preparation were listed in Table 1.

Table 1 The compositions of PVA/PEI hydrogels

Codes	PVA (% w/v)	PEI (mL)	Glu (µL)
P30	10	1	30
P60	10	1	60
P120	10	1	120
P30-0.5	10	0.5	30
P30-0.1	10	0.1	30
P30-0.05	10	0.05	30
PP5	5	0.5	30
PP2.5	2.5	0.5	30
PP1	1	0.5	30

Characterization of PVA/PEI Hydrogels

With using FTIR-ATR measurements the chemical structure of the PVA/PEI hydrogels was determined. The FTIR-ATR spectrum was obtained in the range of 600-4000 cm-1. The morphological properties of the selected hydrogels were performed with FESEM (Hitachi Regulus 8230 FE-SEM). The samples were coated with gold prior to SEM measurements.

Swelling ratio tests

Swelling measurements were carried out with using a thermostated water bath at 37 °C, at pH 7.4 and deionized water were used. Hydrogel samples were dried and measured (M_{dried}) after (M_{dried}) hydrogel samples were placed into buffer solution and the swollen hydrogels were measured after the excess water was removed from the surfaces of the samples ($M_{swollen}$). Hydrogels swelling ratio were calculated with the given formula (1):

$$SR(\%) = \frac{M_{swollen} - M_{dried}}{M_{dried}} \times 100 \qquad (1)$$

All of the swelling ratio experiments were performed in triplicate.

Dehydration tests

For the investigation of the hydrogels water loss percentage, dehydration tests were performed. Firstly, hydrogels were swollen in distilled water and keep under the room temperature. After at specific time intervals the wet hydrogels were weighed and the percentage of the water loss was calculated as given formula below (2). All of the dehydration experiments were performed in triplicate.

$$\text{Dehydration rate } (\%) = \frac{m_i - m_t}{m} \times 100 \qquad (2)$$

At the formula m_i is represented wet hydrogels initial weight, m_t represented the measured weight of the wet hydrogel at predetermined time t and m is represented the hydrogels water content. All of the dehydration experiments were performed in triplicate.

Antibacterial Assay

Escherichia coli (E. coli) was used for the antimicrobial studies of PVA-PEI hydrogels. *E. coli* was inoculated in LB medium and incubated for 24 h, at 37°C. After incubation bacterial solution diluted to be 10^{-3} times and 100 µL of diluted bacterial suspensions were added to eppendorf tubes with 900 µL LB medium inside. Hydrogels were cut as 9 mm diameter, washed with deionized water and sterilized under ultraviolet (UV) light for 10 min for each side. Each hydrogel was added into eppendorf tubes containing bacterial suspensions. One eppendorf tube without added PVA/PEI hydrogel was considered as a control group. PVA/PEI hydrogels were incubated at 37°C for 24h inside of incubator set up for 150 rpm. After the incubation, PVA/PEI hydrogel containing bacterial solutions were diluted to be 10^{-6} and control group diluted to be 10^{-7}. 100 µL of diluted solutions were inoculated onto the LB agar plates and spread to the surface. Agar plates were incubated at 37°C for 24 h, after the number of colonies were counted and colony forming units (CFUs) was calculated. All of the experiments were performed three times and average colony numbers were taken into account. [23, 24].

RESULTS AND DISCUSSION

Characterization of PVA/PEI Hydrogels

FTIR-ATR measurements of PVA and PVA/PEI hydrogels

FTIR-ATR spectra of PVA/PEI hydrogels were shown in Fig. 1. It was clearly seen that they present very similar profiles. The band appeared at 1643 cm-1 is assigned to the formation of C=N bonds supporting the crosslinking reactions between primary amine groups of PEI and glutaraldehyde [25]. The characteristic band of pure PVA at around 3283 cm-1 corresponds to the stretching vibration of hydroxyl groups of PVA. The intensity of this band was decreased significantly after the synthesis of PVA/PEI hydrogel indicating the reduction of available hydroxyl groups which attributes to the formation of hydrogen bonding of PVA with PEI [26]. In addition, with the increased amount of Glu, the color of the hydrogels was observed to change from white to slight yellow indicating the cross-linking reaction took place.
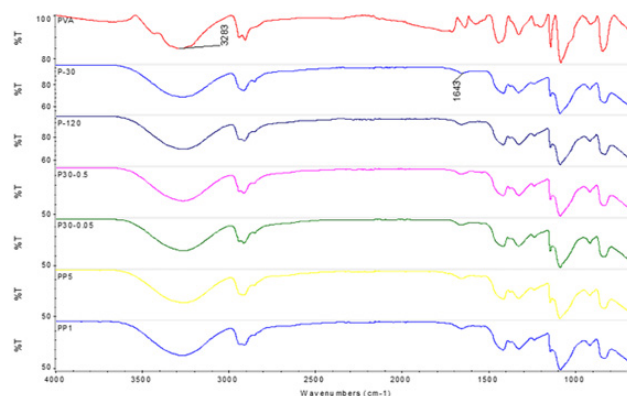

Figure 1 FTIR-ATR spectra of PVA and PVA/PEI hydrogels.

SEM measurements of the P30, P30-0.5 and PP1 hydrogels

The SEM images of P30, P30-0.5 and PP1 were demonstrated in Figure 2 to explain the morphological characteristics of the hydrogels. All the hydrogels possessed porous structures with different porosity and homogeneity. The average pore sizes of the hydrogels were determined with ImageJ software using 15 individual measurements for each sample and found as 3.5±0.9, 13.4±4.9 and 37.7±11.2 um for P-30, P30-0.5 and PP1 respectively. P-30 had interconnected pores with high porosity. The pores of PVA/PEI hydrogel increased in size with the decrease in PEI amount. With the reduction of PVA ratio, the pores became larger which supports the higher swelling capacity enabling the penetration of water molecules. Morphological features were found to be consistent with the swelling results.
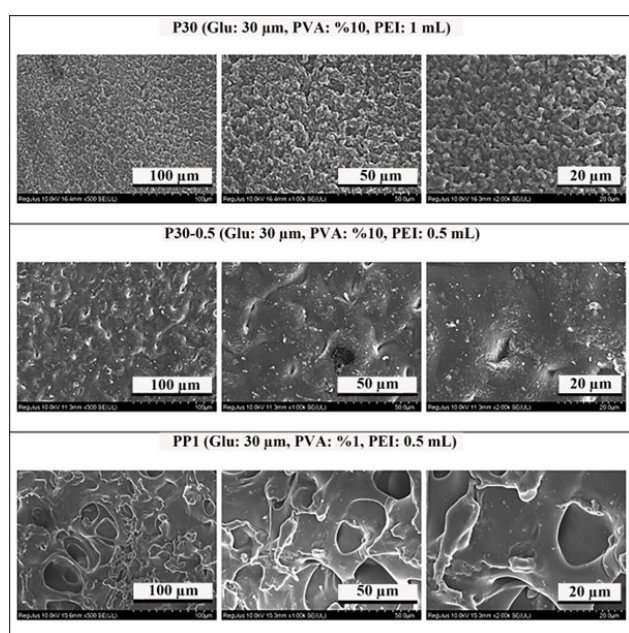

Figure 2 SEM images of the PVA/PEI hydrogels (P30, P30-0.5 and PP1).

Swelling ratio of the PVA/PEI hydrogels

The effect of Glu amount on swelling kinetics was examined and the obtained results were demonstrated in Figure 3a. The mass ratios of Glu were utilized as 0.5, 1 and 2 %w/v. PVA/PEI hydrogels follow the similar trend; firstly, they swelled rapidly at the initial periods after immersion, then the swelling ratio decreases and finally reached an equilibrium value. The swelling amount of PVA/PEI fabricated with 30 μL Glu was higher than that of PVA/PEI fabricated with 60 and 120 μL Glu. PVA/PEI hydrogels swelling ratio was decreased when the amount of Glu was increased due to formation of more crosslinks between PEI and Glu. The increase in Glu amount results in more rigid polymeric structure since the mobility of the polymer chains is hindered [27]. Thus, with the higher crosslinking available free area for the diffusion of water molecules is diminished and the swelling capability is lowered. 30 μL is selected and used for the further experiments.

Figure 3b shows the effect of PEI content on swelling ratio of

PVA/PEI hydrogels when PEI amount was changed as 1, 0.5, 0.1 and 0.05 mL. The highest SR was observed for PVA/PEI hydrogel synthesized using 0.5 mL PEI. The increased swelling capacity caused by incorporation of PEI chains providing high amount of amine groups available for hydrogen bonding with water molecules. PEI with branched structure having high amount of amine groups enables interaction with more water molecules [28]. However, SR was reduced when PEI amount was 1 mL indicating more than adequate amount of PEI blocks the diffusion of water molecules throughout the polymeric matrix. The obtained SR results were compatible with the results reported by Mohan and Geckeler [29].

The effect of PVA content on water holding capacity of PVA/PEI hydrogels was evaluated in Figure 3c. The highest swelling capacity was found with PVA/PEI hydrogels prepared with 1% PVA content and the lowest swelling amount was obtained from the hydrogels having PVA (10 %). The swelling capability of PVA/PEI hydrogels decreased due to the increase in PVA content. Higher PVA amount in the polymeric structure may cause stronger hydrogen bonding leading less interaction with water molecules. Chaturvedi et al. and Shim et al were reported similar results [14, 30]. In addition, increased amount of PVA content provides the integration of PEI chains more effectively leading the polymeric structure more hydrophilic.

In order to reach the swelling equilibrium (t_{eq}), evaluations were carried out at different time periods. Required time periods were follows as: 90, 120 and 150 min for P30, P60 and P120; approximately 60 min for P30-0.5, P30-0.1, P30-0.05; approximately 45 min for PP5, PP2.5 and PP1. The increased amount of Glu caused the increment in t_{eq}. The hydrogel becomes denser with the increase of cross-linker amount making the hydrogels swollen in a slower manner. For the other PVA/PEI hydrogels, t_{eq} remained almost stable due to the constant cross-linker amount.

Statistical Analysis

In this study, Design Expert 7.0 trial version software package program was used to construct design by using historical data. ANOVA Table comprises the predicted the effective parameters on responses.

Swelling kinetic models

The swelling kinetics of PVA/PEI hydrogels in distilled water were examined with first order kinetic model and second order kinetic model which are defined as the linearized forms:

$$\log\left(1 - \frac{M}{M_e}\right) = K_f t \qquad (3)$$

$$\frac{t}{M} = A + Bt \qquad (4)$$

$$A = \frac{1}{K_s M_e^2} \qquad (5)$$

$$B = \frac{1}{M_{e,theo}} \qquad (6)$$

where, M and $M_{e,theo}$ are water swelling of the hydrogel at time t (min) and at equilibrium. The slope of log $\left(1 - M/M_e\right)$ versus t gives K_f that is the first order rate constant. The slope of t/M versus t yields K_s which is the second order rate constant. The kinetic parameters were listed in Table 2. The swelling data fits more to second order kinetic model rather than first order kinetic model according to the regression coefficients. Also, the theoretical swelling ratio is close to the experimental swelling ratios. As seen in Table 2, the K_s values of PVA/PEI hydrogels decreased with the increasing crosslinker amount. There existed no significant difference when PEI amount was changed. The value of K_s was enlarged by lowering PVA content. The results were all comparable with the swelling data since K_s depends on many parameters like crosslinking degree, hydrophilicity of the polymeric structure [31].

In order to determine the swelling mechanism of PVA/PEI hydrogels, the following equation was used:

$$F = \frac{M_t}{M_e} = kt^n \qquad (7)$$

M_t: the mass of the water diffused into the hydrogel at regular time interval

M_e: the mass of the water diffused into the hydrogel at equilibrium state

k: the characteristic constant of network structure

n: the swelling exponent which indicates the transport mode of diffusion.

Table 2 shows swelling kinetic parameters of swelling exponent (n) and characteristic constant (k). The n value defines the diffusion mechanism through the polymeric matrix, such as Fickian diffusion where n≤0.5 and Non-Fickian diffusion where 0.5<n<1. For Fickian diffusion, the relaxation rate of the polymer chains is greater than the diffusion rate of solvent molecules through the matrix [6]. The effect of Glu concentration on diffusion was investigated. Due to the increased amount of cross-linker, the n value was increased from 0.35 to 0.53. The fickian diffusion was occurred when 30 uL of Glu was utilized while non-fickian diffusion was appeared with the increased amount of Glu. The reason may be the formation of more rigid structure with more cross-linker. There exist no significant effect of the amount of PEI on the diffusion type. Fickian diffusion was also observed for PVA/PEI hydrogels with varying PVA content (5%-1%). PVA/PEI hydrogels presented important potential as biomaterials since almost all of the hydrogels demonstrated a Fickian diffusion [32].

The diffusion coefficients (D) were also calculated via the short time approximation method using the first 60% of the swelling data with the following equation:

$$\frac{M_t}{M_e} = 4\left[\frac{Dt}{\pi r^2}\right]^2 \qquad (8)$$

where r is the radius of the hydrogels (cm). The diffusion coefficient was calculated using the plot of M_t/M_e versus $t^{0.5}$. It was clearly observed that the diffusion coefficient decreased with increasing Glu amount due to the fabrication of more compact structure with the crosslinking reactions [33]. There existed no significant effect of PEI amount on D values. The decrease of the diffusion coefficients with decreasing content of PVA may be caused by the hydrolytic degradation of the hydrogels namley, PP2.5 and PP1.

Table 3. ANOVA table for n value of swelling of the hydrogels. In Table 3, it can be said that model is significant owing to the lower p-value (0.0022). The most effective parameters was found as PVA since it showed higher F-value than the other selected two parameters. The insignificant factor was found to be glutaraldehyde because of the higher p-value (0.1214). Besides, statistical indicators such as R2 and Adj-R2 were calculated by design expert 7.0. The determination coefficient (r2) was calculated as 0.9347. This implies that model data is fitted well to experimental data. Furthermore, Adjustment R-squared was calculated as 0.8956.

Table 2 The kinetic parameters for swelling of PVA/PEI hydrogels.

Codes	n	k	R^2	D x 10^2 (cm²/min)
P30	0.35	0.21	0.98	0.28
P60	0.52	0.15	0.90	0.29
P120	0.53	0.14	0.93	0.17
P30-0.5	0.50	0.25	0.97	0.29
P30-0.1	0.50	0.13	0.91	0.31
P30-0.05	0.51	0.12	0.93	0.33
PP5	0.23	0.39	0.97	0.34
PP2.5	0.18	0.47	0.95	0.31
PP1	0.19	0.50	0.97	0.23

Table 3 ANOVA table for n value of swelling of the hydrogels.

p-value Source Prob>F	Sum of Squares	df	Mean Square	F value
Model 0.0022	0.16 significant	3	0.053	23.87
A-PEI 0.0232	0.023	1	0.023	10.43
B-Glu 0.1214	7.696E-003	1	7.696E-003	3.47
C-PVA 0.0008	0.12	1	0.12	52.29
Residual	0.011	5	2.216E-003	
Cor Total	0.17	8		

The lineer equation for n-value in terms of coded factors was given in Eq. (9)

$$n = 0.35 - 0.086 * A + 0.059 * B + 0.15 * C \qquad (9)$$

where A, B and C represents PEI, Glu, PVA, respectively. The optimal conditions were found 0.05 x mL of PEI, 119.99 μL of Glu and 10.00 of % PVA

Figure 4.a depicted the binary interaction of PEI and Glu on n-value at optimal conditions. When n-value increased with increasing the amount of Glu. If the amount of PEI was increased from 0.05 to 1.0, n-value was decreased. The binary interaction effect of PEI and PVA on n-value at optimal conditions were shown in Figure 4.b. n-value increased with increasing the amount of PVA in 3-D graph. Also, Increasing PEI has reverse effect on n-value. The Pareto chart was constructed were given in Eq. (10) [34].

$$P_i = \left(\frac{\beta_i^2}{\sum \beta_i^2}\right) \times 100 \left(i \neq 0\right) \tag{10}$$

In Eq (10), β_i represents the coefficient of variables, P_i is the percentage of each variable, respectively. Thus, the variables affecting on the n-value (%) were depicted in Figure 4.c. The most important variable was the amount of PVA (C, 67.41 %). The other variables are listed as follows: PEI (A, 22.16 %) and Glu (B, 10.43%). The least effective variable was found to be Glu (B) under α=0.05 significance.
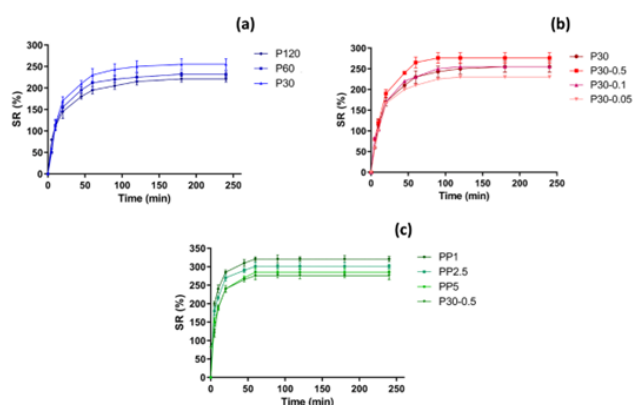

Figure 3 The effect of Glu amount (PVA: 10%, PEI: 1 mL) (a), PEI amount (PVA: 10%, Glu: 30 μL) (b) and PVA content (Glu: 30 μL, PEI: 0.1 mL) (c) on the swelling degree of PVA/PEI hydrogels.
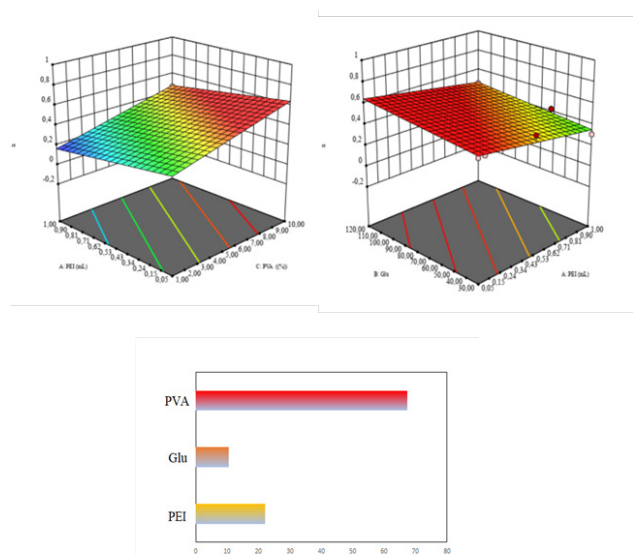

Figure 4 The binary interaction effect of (a) PEI and Glu on n-value at optimal conditions and (b) PEI and PVA on n-value at optimal conditions and (c) Pareto graph for the influences of factors affecting on the n-value.

One of the major parameters of the swelling process is the pH of the biological medium. The pH of the healthy skin is in the range of 4.0-6.0 while it becomes around pH 7.4 when exposed to blood after injury [35]. pH-responsive polymers contain ionizable functional groups and thus their swelling degree is mainly based on the protonation state of these groups due to pKa values. The charged polymeric matrix facilitates the interaction of hydrogen bonding with the hydrated deposit. The prepared PVA/PEI hydrogels showed the similar trend since they swell more at pH 7.4 in comparison with pH 4 (Figure 5). PEI as a cationic polymer (pKa ≈ 7.4) bears high amount of amine groups having higher amount of protonated amine groups at acidic pH. However great number of protonated amine groups leaded to a significant reduction of swelling capacity by disarranging the hydrated layer. Avais and Chattopadhyay prepared PEI hydrogels via chemical cross-linking using azetidinium based crosslinker and reported pH-responsivity of the prepared PEI hydrogels with maximum swelling capacity at pH 7.4 [36]. The removal of exudate from the wound site is a crucial step for effective wound healing. The prepared PVA/PEI hydrogels swell more at pH of wound area enabling the removal of exudate from the wound site efficiently.
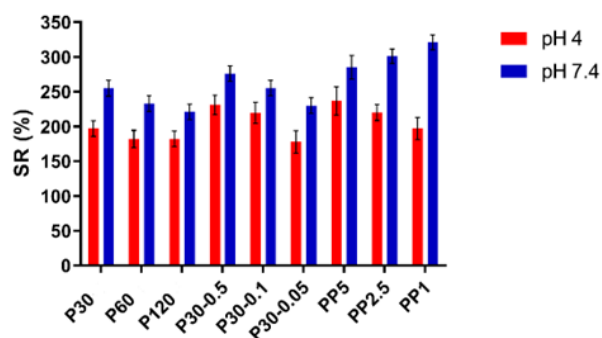

Figure 5 The swelling ratio of PVA/PEI hydrogels with pH 4 and 7.4.

Dehydration tests

The dehydration kinetic curves were shown in Figure 6. Firstly, water loss from the hydrogels occurred fast, then reduced slowly and finally reached an equilibrium value. The hydrogel prepared with the largest Glu amount had the lowest dehydration rate since more rigid polymeric structure inhibit the water loss (Fig 6(a)). The hydrogel synthesized with the lowest PVA content showed the biggest dehydration rate while having large pores would favor the dehydration of the hydrogel (Fig 6(c)). The bulk water molecules diffuse easily from the large pores however they can be retained as bound water via hydrogen bonding in the pores [37]. PVA has the dominant effect on the dehydration process.

Antibacterial activity assay

The antibacterial properties of the hydrogels were examined by colony formation counting assay and percentage antibacterial activity of PVA-PEI hydrogels against *E. coli* were given in Figure 7. PVA ratio increases in PP1, PP2.5 and PP5 hydrogels, respectively. As gelation of these hydrogels increased, PEI were expected to effectively incorporate into

hydrogel structure. The PP5 and PP2.5 hydrogels showed 98.2% and 96.3% antibacterial activities, respectively. However, antibacterial effect of PP1was 66.7%. Antibacterial efficiency of P30, P60 and P120 hydrogels which have different Glu ratio were 66.7%, 61.8% and 41.3%, respectively. As we conclude from the percentage antibacterial activity results, antibacterial activities of PP2.5 and P30-0.1, PP5 hydrogels was over 96.4%. Thus, these three hydrogels showed excellent antibacterial activity for *E. coli*. P30-0.1 with 99.9% antibacterial activity was found as the most effective among the hydrogels containing different amount of PEI. The antibacterial performance of the antibacterial hydrogels depends on chemical and morphological characteristics of the polymeric matrix. PEI as a cationic polymer improves the antibacterial activity of the hydrogels due to the disruption of the bacterial cell membrane. The hydrogels with high porosity facilitate the interaction of the microorganisms with the polymeric structure [38].
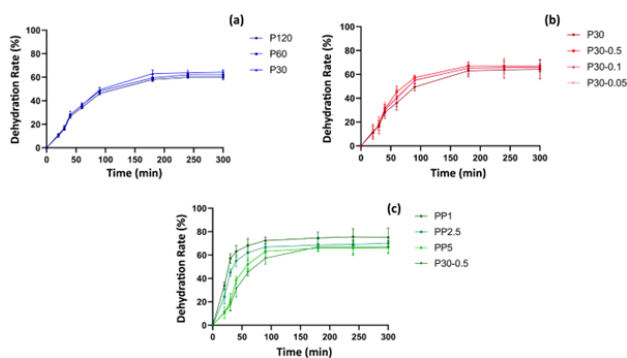

Figure 6 The effect of Glu amount (PVA: 10%, PEI: 1 mL) (a), PEI amount (PVA: 10%, Glu: 30 µL) (b) and PVA content (Glu: 30 µL, PEI: 0.1 mL) (c) on the dehydration rate of PVA/PEI hydrogels.
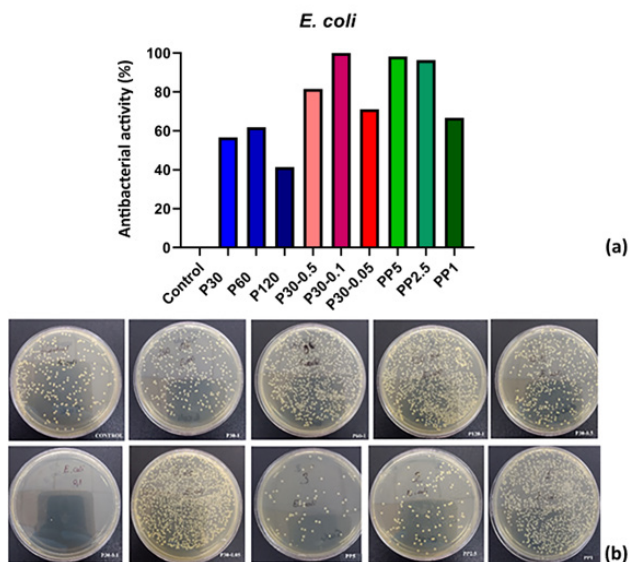

Figure 7 Colony formation counting assay results, (a) percentage antibacterial activities of PVA/PEI hydrogels against *E. coli*, (b) optic images of agar plates. Dilution factor: 10-7 for control group and 10-6 for hydrogels. Hydrogels treated *E. coli* was inoculated in agar plates and incubated for 24 h at 37 °C.

Consequently, the correlation between swelling amount, dehydration rate, and antibacterial activity was created in the 3D plot to evaluate the optimum PVA/PEI hydrogel for antibacterial wound dressing materials. It has been reported that PEI added to PVA/PEI hydrogels consists of high positive charges that are sensitive to antibacterial activity [12]. As can be seen from Figure 8, the PVA/PEI hydrogel (PP5) with the highest PEI (0.5 mL) and PVA (5%) content has significantly demonstrated the excellent antibacterial activities of the PEI in the PVA/PEI hydrogels. In addition, it is clear that the optimum PVA/PEI hydrogel as an excellent antibacterial wound dressing material is the PP5 hydrogel due to its high swelling amount, low dehydration rate and great antibacterial activity.
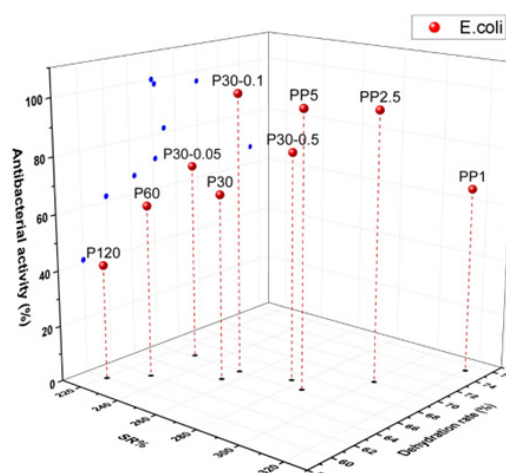

Figure 8 3D plot of PVA/PEI hydrogels against antibacterial activity, swelling amount and dehydration rate.

CONCLUSION

The aim of this study was to investigate the swelling amount, dehydration rate and antibacterial activity performance that are crucial key parameters for wound healing applications. For this propose, PVA/PEI hydrogels were prepared via solvent casting technique with different amount Glu, PEI and PVA concentration. All of the hydrogels showed great swelling degree at pH 7.4 simulating human biological fluids and 37 °C. PVA concentration showed the dominant effect on the swelling degree as well as the dehydration results. All of the prepared PVA/PEI hydrogels demonstrated high antibacterial activity against *E. coli*. The obtained results were related with the incorporation of PEI into the polymeric structure and the morphological properties of the hydrogels. 3D plot containing swelling degree, dehydration percentage and antibacterial activity displayed the optimum hydrogel depending on these parameters. PP5 was determined as the best hydrogel with the optimized data.

References

1. Cascone, S.; Lamberti, G. Hydrogel-Based Commercial Products for Biomedical Applications: A Review. Int J Pharm, 2020, 573 (November 2019), 118803. https://doi.org/10.1016/j.ijpharm.2019.118803.

2. Özkahraman, B.; Acar, I.; Emik, S. Removal of Cationic Dyes from Aqueous Solutions with Poly (N-Isopropylacrylamide-Co-Itaconic Acid) Hydrogels. Polymer Bulletin, 2011, 66 (4), 551–570. https://doi.org/10.1007/s00289-010-0371-1.

3. Sobhanimatin, M. B.; Pourmahdian, S.; Tehranchi, M. M. Fast Inverse Opal Humidity Sensor Based on Acrylamide/AMPS Hydrogel. Mater Today Commun, 2021, 26 (September 2020), 101997. https://doi.org/10.1016/j.mtcomm.2020.101997.

4. Godiya, C. B.; Kumar, S.; Xiao, Y. Amine Functionalized Egg Albumin Hydrogel with Enhanced Adsorption Potential for Diclofenac Sodium in Water. J Hazard Mater, 2020, 393 (February), 122417. https://doi.org/10.1016/j.jhazmat.2020.122417.

5. Wei, S.; Liu, X.; Zhou, J.; Zhang, J.; Dong, A.; Huang, P.; Wang, W.; Deng, L. Dual-Crosslinked Nanocomposite Hydrogels Based on Quaternized Chitosan and Clindamycin-Loaded Hyperbranched Nanoparticles for Potential Antibacterial Applications. Int J Biol Macromol, 2020, 155, 153–162. https://doi.org/10.1016/j.ijbiomac.2020.03.182.

6. Koc, F. E.; Altıncekic, T. G. Investigation of Gelatin/Chitosan as Potential Biodegradable Polymer Films on Swelling Behavior and Methylene Blue Release Kinetics. Polymer Bulletin, 2021, 78 (6), 3383–3398. https://doi.org/10.1007/s00289-020-03280-7.

7. Guo, T.; Wang, W.; Song, J.; Jin, Y.; Xiao, H. Dual-Responsive Carboxymethyl Cellulose/Dopamine/Cystamine Hydrogels Driven by Dynamic Metal-Ligand and Redox Linkages for Controllable Release of Agrochemical. Carbohydr Polym, 2021, 253 (September 2020), 117188. https://doi.org/10.1016/j.carbpol.2020.117188.

8. Tamahkar, E.; Özkahraman, B.; Süloğlu, A. K.; İdil, N.; Perçin, I. A Novel Multilayer Hydrogel Wound Dressing for Antibiotic Release. J Drug Deliv Sci Technol, 2020, 58 (July). https://doi.org/10.1016/j.jddst.2020.101536.

9. Ahsan, A.; Farooq, M. A. Therapeutic Potential of Green Synthesized Silver Nanoparticles Loaded PVA Hydrogel Patches for Wound Healing. J Drug Deliv Sci Technol, 2019, 54 (October), 101308. https://doi.org/10.1016/j.jddst.2019.101308.

10. Spearman, B. S.; Agrawal, N. K.; Rubiano, A.; Simmons, C. S.; Mobini, S.; Schmidt, C. E. Tunable Methacrylated Hyaluronic Acid-Based Hydrogels as Scaffolds for Soft Tissue Engineering Applications. J Biomed Mater Res A, 2020, 108 (2), 279–291. https://doi.org/10.1002/jbm.a.36814.

11. Hernandez-Montelongo, J.; Lucchesi, E. G.; Nascimento, V. F.; França, C. G.; Gonzalez, I.; Macedo, W. A. A.; Machado, D.; Lancellotti, M.; Moraes, A. M.; Beppu, M. M.; et al. Antibacterial and Non-Cytotoxic Ultra-Thin Polyethylenimine Film. Materials Science and Engineering C, 2017, 71, 718–724. https://doi.org/10.1016/j.msec.2016.10.064.

12. Hernandez-Montelongo, J.; Corrales Ureña, Y. R.; Machado, D.; Lancelloti, M.; Pinheiro, M. P.; Rischka, K.; Lisboa-Filho, P. N.; Cotta, M. A. Electrostatic Immobilization of Antimicrobial Peptides on Polyethylenimine and Their Antibacterial Effect against Staphylococcus Epidermidis. Colloids Surf B Biointerfaces, 2018, 164, 370–378. https://doi.org/10.1016/j.colsurfb.2018.02.002.

13. Khorasani, M. T.; Joorabloo, A.; Moghaddam, A.; Shamsi, H.; MansooriMoghadam, Z. Incorporation of ZnO Nanoparticles into Heparinised Polyvinyl Alcohol/Chitosan Hydrogels for Wound Dressing Application. Int J Biol Macromol, 2018, 114, 1203–1215. https://doi.org/10.1016/j.ijbiomac.2018.04.010.

14. Chaturvedi, A.; Bajpai, A. K.; Bajpai, J.; Singh, S. K. Evaluation of Poly (Vinyl Alcohol) Based Cryogel-Zinc Oxide Nanocomposites for Possible Applications as Wound Dressing Materials. Materials Science and Engineering C, 2016, 65, 408–418. https://doi.org/10.1016/j.msec.2016.04.054.

15. Boran, F.; Karakaya, Ç. Polyvinyl Alcohol / CuO Nanocomposite Hydrogels : Facile Synthesis and Long-Term Stability. Journal of Balıkesır University Institute of Science and Technology, 2019, 21 (2), 512–530. https://doi.org/10.25092/baunfbed.624392.

16. Kanmaz, N.; Saloglu, D.; Hizal, J. Humic Acid Embedded Chitosan/Poly (Vinyl Alcohol) PH-Sensitive Hydrogel: Synthesis, Characterization, Swelling Kinetic and Diffusion Coefficient. Chem Eng Commun, 2019, 206 (9), 1168–1180. https://doi.org/10.1080/00986445.2018.1550396.

17. Zhang, Z.; Liu, Y.; Lin, S.; Wang, Q. Preparation and Properties of Glutaraldehyde Crosslinked Poly(Vinyl Alcohol) Membrane with Gradient Structure. Journal of Polymer Research, 2020, 27 (8), 0–6. https://doi.org/10.1007/s10965-020-02223-0.

18. Hou, T.; Guo, K.; Wang, Z.; Zhang, X. F.; Feng, Y.; He, M.; Yao, J. Glutaraldehyde and Polyvinyl Alcohol Crosslinked Cellulose Membranes for Efficient Methyl Orange and Congo Red Removal. Cellulose, 2019, 26 (8), 5065–5074. https://doi.org/10.1007/s10570-019-02433-w.

19. Mehrotra, T.; Zaman, M. N.; Prasad, B. B.; Shukla, A.; Aggarwal, S.; Singh, R. Rapid Immobilization of Viable Bacillus Pseudomycoides in Polyvinyl Alcohol/Glutaraldehyde Hydrogel for Biological Treatment of Municipal Wastewater. Environmental Science and Pollution Research, 2020, 27 (9), 9167–9180. https://doi.org/10.1007/s11356-019-07296-z.

20. Wang, C.; Hu, K.; Zhao, C.; Zou, Y.; Liu, Y.; Qu, X.; Jiang, D.; Li, Z.; Zhang, M. R.; Li, Z. Customization of Conductive Elastomer Based on PVA/PEI for Stretchable Sensors. Small, 2020, 16 (7), 1–9. https://doi.org/10.1002/smll.201904758.

21. Dridi, F.; Marrakchi, M.; Gargouri, M.; Garcia-Cruz, A.; Dzyadevych, S.; Vocanson, F.; Saulnier, J.; Jaffrezic-Renault, N.; Lagarde, F. Thermolysin Entrapped in a Gold Nanoparticles/Polymer Composite for Direct and Sensitive Conductometric Biosensing of Ochratoxin A in Olive Oil. Sens Actuators B Chem, 2015, 221, 480–490. https://doi.org/10.1016/j.snb.2015.06.120.

22. Sun, X.; Yang, L.; Li, Q.; Liu, Z.; Dong, T.; Liu, H. Polyethylenimine-Functionalized Poly(Vinyl Alcohol) Magnetic Microspheres as a Novel Adsorbent for Rapid Removal of Cr(VI) from Aqueous Solution. Chemical Engineering Journal, 2015, 262, 101–108. https://doi.org/10.1016/j.cej.2014.09.045.

23. Gao, F.; Xiao, J.; Huang, G. Current Scenario of Tetrazole Hybrids for Antibacterial Activity. Eur J Med Chem, 2019, 184, 111744. https://doi.org/10.1016/j.ejmech.2019.111744.

24. Fang, H.; Wang, J.; Li, L.; Xu, L.; Wu, Y.; Wang, Y.; Fei, X.; Tian, J.; Li, Y. A Novel High-Strength Poly(Ionic Liquid)/PVA Hydrogel Dressing for Antibacterial Applications. Chemical Engineering Journal, 2019, 365 (January), 153–164. https://doi.org/10.1016/j.cej.2019.02.030.

25. Wang, S.; Xiao, K.; Mo, Y.; Yang, B.; Vincent, T.; Faur, C.; Guibal, E. Selenium(VI) and Copper(II) Adsorption Using Polyethyleneimine-Based Resins: Effect of Glutaraldehyde Crosslinking and Storage Condition. J Hazard Mater, 2020, 386 (September 2019), 121637. https://doi.org/10.1016/j.jhazmat.2019.121637.

26. Liu, Z.; Han, S.; Xu, C.; Luo, Y.; Peng, N.; Qin, C.; Zhou, M.; Wang,

W.; Chen, L.; Okada, S. In Situ Crosslinked PVA-PEI Polymer Binder for Long-Cycle Silicon Anodes in Li-Ion Batteries. RSC Adv, 2016, 6 (72), 68371–68378. https://doi.org/10.1039/c6ra12232a.

27. Long, J.; Nand, A. V.; Bunt, C.; Seyfoddin, A. Controlled Release of Dexamethasone from Poly(Vinyl Alcohol) Hydrogel. Pharm Dev Technol, 2019, 24 (7), 839–848. https://doi.org/10.1080/10837450.2019.1602632.

28. Guan, Y.; Wang, L.; Cui, L.; Shen, X.; Gao, W.; Meng, J.; Li, D.; Shen, C.; Zhang, Y.; Hu, G.; et al. Preparation and Rheological Investigation of Tough PAAm Hydrogel by Adding Branched Polyethyleneimine. J Appl Polym Sci, 2020, 137 (14), 1–7. https://doi.org/10.1002/app.48541.

29. Mohan, Y. M.; Geckeler, K. E. Polyampholytic Hydrogels: Poly(N-Isopropylacrylamide)-Based Stimuli-Responsive Networks with Poly(Ethyleneimine). React Funct Polym, 2007, 67 (2), 144–155. https://doi.org/10.1016/j.reactfunctpolym.2006.10.010.

30. Shim, J. K.; Oh, S. R.; Lee, S. B.; Cho, K. M. Preparation of Hydrogels Composed of Poly(Vinyl Alcohol) and Polyethyleneimine and Their Electrical Response. J Appl Polym Sci, 2008, 107 (4), 2136–2141. https://doi.org/10.1002/app.26676.

31. Panpinit, S.; Pongsomboon, S. amnart; Keawin, T.; Saengsuwan, S. Development of Multicomponent Interpenetrating Polymer Network (IPN) Hydrogel Films Based on 2-Hydroxyethyl Methacrylate (HEMA), Acrylamide (AM), Polyvinyl Alcohol (PVA) and Chitosan (CS) with Enhanced Mechanical Strengths, Water Swelling and Antibacteria. Reactive and Functional Polymers, 2020, 156 (September), 104739. https://doi.org/10.1016/j.reactfunctpolym.2020.104739.

32. Jayaramudu, T.; Ko, H.-U.; Kim, H. C.; Kim, J. W.; Kim, J. Swelling Behavior of Polyacrylamide–Cellulose Nanocrystal Hydrogels: Swelling Kinetics, Temperature, and PH Effects. Materials, 2019, 12 (13), 2080. https://doi.org/10.3390/ma12132080.

33. Aydınoğlu, D. Investigation of PH-Dependent Swelling Behavior and Kinetic Parameters of Novel Poly(Acrylamide-Co-Acrylic Acid) Hydrogels with Spirulina. E-Polymers, 2015, 15 (2), 81–93. https://doi.org/10.1515/epoly-2014-0170.

34. Abdessalem, A. K.; Oturan, N.; Bellakhal, N.; Dachraoui, M.; Oturan, M. A. Experimental Design Methodology Applied to Electro-Fenton Treatment for Degradation of Herbicide Chlortoluron. Applied Catalysis B: Environmental, 2008, 78 (3–4), 334–341. https://doi.org/10.1016/j.apcatb.2007.09.032.

35. Schneider, L. A.; Korber, A.; Grabbe, S.; Dissemond, J. Influence of PH on Wound-Healing: A New Perspective for Wound-Therapy? Arch Dermatol Res, 2007, 298 (9), 413–420. https://doi.org/10.1007/s00403-006-0713-x.

36. Avais, M.; Chattopadhyay, S. Waterborne PH Responsive Hydrogels: Synthesis, Characterization and Selective PH Responsive Behavior around Physiological PH. Polymer (Guildf), 2019, 180 (August), 121701. https://doi.org/10.1016/j.polymer.2019.121701.

37. Huang, Y.; Shi, F.; Wang, L.; Yang, Y.; Khan, B. M.; Cheong, K. L.; Liu, Y. Preparation and Evaluation of Bletilla Striata Polysaccharide/Carboxymethyl Chitosan/Carbomer 940 Hydrogel for Wound Healing. Int J Biol Macromol, 2019, 132, 729–737. https://doi.org/10.1016/j.ijbiomac.2019.03.157.

38. Pillai, S. K. R.; Reghu, S.; Vikhe, Y.; Zheng, H.; Koh, C. H.; Chan-Park, M. B. Novel Antimicrobial Coating on Silicone Contact Lens Using Glycidyl Methacrylate and Polyethyleneimine Based Polymers. Macromol Rapid Commun, 2020, 41 (21), 1–10. https://doi.org/10.1002/marc.202000175.